



8-2001

Design and analysis of a novel electric machine and drive

Daniel Steven Daniel

Follow this and additional works at: https://trace.tennessee.edu/utk_graddiss

Recommended Citation

Daniel, Daniel Steven, "Design and analysis of a novel electric machine and drive. " PhD diss., University of Tennessee, 2001.

https://trace.tennessee.edu/utk_graddiss/8486

This Dissertation is brought to you for free and open access by the Graduate School at TRACE: Tennessee Research and Creative Exchange. It has been accepted for inclusion in Doctoral Dissertations by an authorized administrator of TRACE: Tennessee Research and Creative Exchange. For more information, please contact trace@utk.edu.

To the Graduate Council:

I am submitting herewith a dissertation written by Daniel Steven Daniel entitled "Design and analysis of a novel electric machine and drive." I have examined the final electronic copy of this dissertation for form and content and recommend that it be accepted in partial fulfillment of the requirements for the degree of Doctor of Philosophy, with a major in Electrical Engineering.

J. Milton Bailey, Major Professor

We have read this dissertation and recommend its acceptance:

Vasilios Alexiades, Paul B. Crilly, Jack S. Lawler

Accepted for the Council:

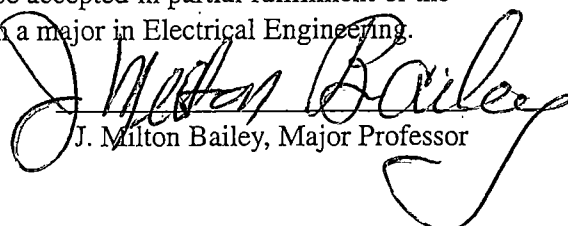
Carolyn R. Hodges

Vice Provost and Dean of the Graduate School

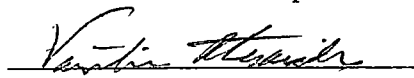
(Original signatures are on file with official student records.)

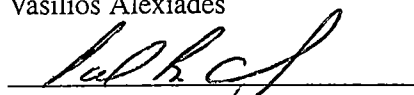
To the Graduate Council:

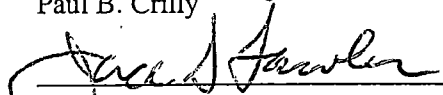
I am submitting herewith a dissertation written by Daniel S. Daniel entitled: "Design and Analysis of a Novel Electric Machine and Drive" I have examined the final copy of this dissertation for form and content and recommend that it be accepted in partial fulfillment of the requirements for the degree of Doctor of Philosophy, with a major in Electrical Engineering.


J. Milton Bailey, Major Professor

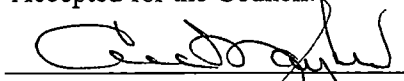
We have read this dissertation
and recommend its acceptance:


Vasilios Alexiades


Paul B. Crilly


Jack S. Lawler

Accepted for the Council:


Interim Vice Provost and
Dean of The Graduate School

Design and Analysis of a Novel Electric Machine and Drive

A Dissertation

Presented for the

Doctor of Philosophy

Degree

The University of Tennessee, Knoxville

Daniel S. Daniel

August 2001

Dedication

To the memory of Drs. John Nunley Snider and Herbert Neff, Jr. and to my loving wife Anamary and our daughter Anastasia .

Acknowledgments

Firstly, I wish to thank Dr. J. Milton Bailey for his continuous support and guidance throughout my academic and professional career. In addition, I would like to thank Professors Vasilios Alexiades, J.S. Lawler, and P.B. Crilly for serving as my supervisory committee.

I would also like to thank the Engineering Technology Division at the Oak Ridge National Laboratory for their financial support during this effort. In particular, I am extremely grateful to Dr. John McKeever for facilitating this effort.

Finally, I wish to pay tribute to my wife Anamary for her relentless support and infinite patience throughout my degree-seeking years. Without her influence, this endeavor could never have been accomplished.

Abstract

In many areas of engineering, the improvements in material properties have enabled designers to create sophisticated and previously unrealizable geometries feasible.

A new low cost integrated electric machine is designed, analyzed and characterized in this dissertation. The material properties and their effect on motor performance are discussed and examined, the motor design equations are developed and analyzed. The performance test results are compared to analytical expressions previously derived and verified by simulation. Due to the nature by which the machine develops torque, the machine requires an inverter with position feedback which is discussed in detail, additional motor geometries are also presented.

In addition, an overview of Maxwell's equations and their applicability to the electromagnetic, magnetostatic and magnetodynamic problem is presented. Finally, a new method of solving the eddy current problem using the control-volume method is explained and numerical results are presented.

Contents

1	Introduction	1
1.1	Electric Machines	1
1.2	Advances in Material Science	4
1.3	Organization and Contributions	10
2	Design of the Machine	13
2.1	Motor Geometry	13
2.2	Theory of Operation	18
2.3	Stator Design Equations	20
2.4	Design Variations	27
2.5	Prototype Design	29
3	Machine Performance	32
3.1	Analysis of Back-EMF	32
3.2	Torque	36
3.3	Experimental Results	38
4	Magnetic Field Analysis	47
4.1	General Form of Maxwell's Equations	48

CONTENTS

4.2	Low Frequency Case	49
4.2.1	Magnetostatic Case	49
4.2.2	Quasi-Static Case	53
4.2.3	Magnetodynamic Case	54
4.3	Summary of the Applicability of Maxwell's Equations	55
5	Finite-Volume and Finite-Difference Methods	58
5.1	Finite Difference Time Domain Method	59
5.2	Finite Volume Time Domain Method	64
5.3	Application of Finite Volume Technique to Eddy Current Problem	66
5.3.1	Numerical Formulation	67
6	Application of Numerical Methods to Sample Problem	74
6.1	Diffusion in a Conducting Slab	74
6.2	Numerical Implementation	77
6.3	Test Problem	79
6.3.1	Discussion of Numerical Results	80
6.4	Summary	80
7	Conclusions	84
7.1	Recommendations for Future Research	85
	References	87
	Appendices	90
A	Flux Derivation	91
A.1	Salient Motor Design Equations	91
A.1.1	Air Gap Flux	91

CONTENTS

A.1.2	Calculation of Permeances	94
B	Derivation of Back-EMF Equation	96
B.1	Round Magnets	96
B.1.1	Calculation of area and its derivative	97
B.2	Wedge Shaped Magnets	99
C	Electronic Drive Design	102
C.1	Controller Requirements	103
C.2	Power Circuitry	105
C.2.1	Circuit Description	106
C.3	Microcontroller Section	107
D	Microcontroller Source Code	112
E	Mechanical Drawings	118
F	Simulation Files	122
Vita		129

List of Figures

1.1	Conventional axial gap stator.	3
1.2	Typical B-H curve.	7
1.3	Core Loss of Ancorsteel TC-80 vs 3 % Si-Fe lamination.	8
1.4	Initial permeability of Ancorsteel TC-80.	10
2.1	3D solid model of modular motor.	14
2.2	Exploded view of the modular motor.	16
2.3	Movement of rotor magnets over stator poles.	19
2.4	Stator physical dimensions.	21
2.5	Mean magnetic flux paths.	23
2.6	Square Back-emf Machine.	28
3.1	Magnet sweeping area over pole face.	33
3.2	Numerically generated no load waveforms.	35
3.3	Plots of approximating waveforms.	37
3.4	Experimental test setup.	40
3.5	Experimentally determined voltage.	41
3.6	Waveform created from approximating equation.	42
3.7	Flux linkage of experimentally determined waveform.	43

LIST OF FIGURES

3.8	Experimentally determined voltage at 2975 $\frac{rev}{min}$	44
3.9	Generated voltage with winding under load.	45
3.10	Generated voltage vs speed for winding #2.	46
4.1	Replacement of permanent magnet with equivalent sheet current.	52
4.2	Application of Maxwell's equations.	56
5.1	Yee cell.	60
5.2	Control volume in cartesian coordinates.	65
5.3	Control volume in 2D.	72
6.1	Transient diffusion test problem.	76
6.2	Magnetic diffusion into copper slab.	81
6.3	Analytical solution combined with numerical results.	82
6.4	Error in solution.	83
A.1	Reluctance model of single air gap stator.	91
B.1	Geometrical representation of magnet rotating over pole face	97
B.2	Wedge shaped magnets.	99
B.3	Graph of actual versus theoretical back-emf.	101
C.1	Inverter Square Wave Mode.	105
C.2	Power Section.	110
C.3	Microcontroller Section.	111
E.1	Prototype stator drawing.	119
E.2	Prototype rotor drawing.	120
E.3	Prototype shaft drawing.	121

List of Tables

3.1	Magnitudes of odd harmonics.	36
3.2	Winding parameters.	39
6.1	Sample data for simulation.	79

List of Symbols

R = mean radius to pole centers

r_s = radius of shaft

R_o = radius of stator material

d_p = diameter of pole piece

D_s = diameter of shaft

t_m = thickness of stator back iron

t_r = thickness of rotor back iron

g = air gap

A_p = area of pole piece

A_m = area of magnet surface

A_{sw} = area swept as a function of rotation angle

r_c = radius of clearance for shaft

T_m = magnet thickness

N_{mp} = number of magnet poles

h_p = height of pole piece

r_b = radius of bearing

b_{th} = bearing wall thickness

B_{wth} = bobbin wall thickness

r_{ob} = outer radius of bobbin

r_{ib} = inner radius of bobbin

C_{hc} = coil height clearance

l_{rs} = magnetic path length through rotor

l_{sm} = magnetic path length through stator

N_{tc} = number of turns per coil

d_{wire} = diameter of magnet wire

r_w = resistance of winding

\hat{H} magnetic field intensity, *amperes/m*, $\frac{A}{m}$

\hat{B} magnetic flux density, *tesla*, T

\hat{A} magnetic vector potential

\hat{D} electric flux density, *coulomb/m²*, $\frac{C}{m^2}$

\hat{E} electric field strength, *volts/m*, $\frac{V}{m}$

\hat{J} current density, *amperes/m²*, $\frac{A}{m^2}$

ρ volume density of free electric charge, *coulomb/m³*, $\frac{C}{m^3}$

σ electrical conductivity, *mhos/m*, $\frac{\Omega}{m}$

Chapter 1

Introduction

1.1 Electric Machines

Electric machines¹ have, over the years, been the preferred method of converting electrical energy into mechanical energy. Although, the electric machine has been in production for over 150 years little has changed in their basic design. Most rotating electric machines are constructed from the following components: a rotating element (rotor), a stationary element (stator) including current carrying conductors, a shaft with support bearings, a frame and end bells to support the bearings. Rotating machines can be classified into two distinct types dependent on the direction of the air gap flux in relation to the shaft axis; the two types are axial gap and radial gap. The flux in the air gap of the radial gap machine is perpendicular to the rotating axis of the shaft; whereas, the air gap flux flow in the axial gap machine is directed along the rotational axis of the shaft. The radial gap configuration is, by far, the most popular geometry for rotating electric machines. Since the torque in the radial gap machine is proportional to its axial length, this configuration is adequate in applications where the long axial length can be tolerated. Radial gap machines in various types have been mass produced for over 125 years; therefore, the design, analysis and

¹The term electric machine denotes use as a motor or generator

CHAPTER 1. INTRODUCTION

manufacture of the stator and rotor assemblies is well defined.

For applications where space is at a premium, other configurations such as the axial gap machine can provide a suitable alternative. Even though Faraday developed a primitive disc type machine, the predecessor to the modern axial gap machine, in 1821 the use of this configuration has largely been ignored.² Several advances at the Oak Ridge National Laboratory and technological advances in power electronics has increased the exposure of the axial gap machine as a viable structure, especially in reference to electric vehicle drive systems and high specific power applications. Figure 1.1 depicts a typical stator used in a permanent magnet synchronous machine (PMSM) and a brushless DC machine (BDCM).

One of the drawbacks to the axial gap configuration shown in Figure 1.1 is the complexity of the mechanical structure necessary to support a complete machine. A machine of this type is usually constructed from an epoxied, tightly wound low loss magnetic tape. Once epoxied, the structure is mechanically sound but does not lend itself to machining. In particular, the slots must be individually machined and the mounting holes drilled and tapped. Since the current carrying conductors extend past the outside radius of the stator, a significant mounting problem exists since there cannot be any type of mechanical interference between the electrical conductors and any part of the surrounding mechanical structure. Thus, the stator must be secured to the supporting structure by drilling and tapping mounting holes in the rear of the stator. The drilling and tapping of a structure constructed from thin sheets of metal epoxied together has been found [10] to result in a less than optimal retention scheme for the stator. It has been observed, that the axial force of the permanent magnets on the stator has been sufficient to separate the stator from its mount.

In addition, the shape of the coil requires that the volume occupied by the current carrying conductors at the inner and outer radii be equal. Since the available winding volume at the inner radius is much less than that at the outer radius, a severe problem exists since the number of

²There have been developments in Homopolar and printed circuit motors

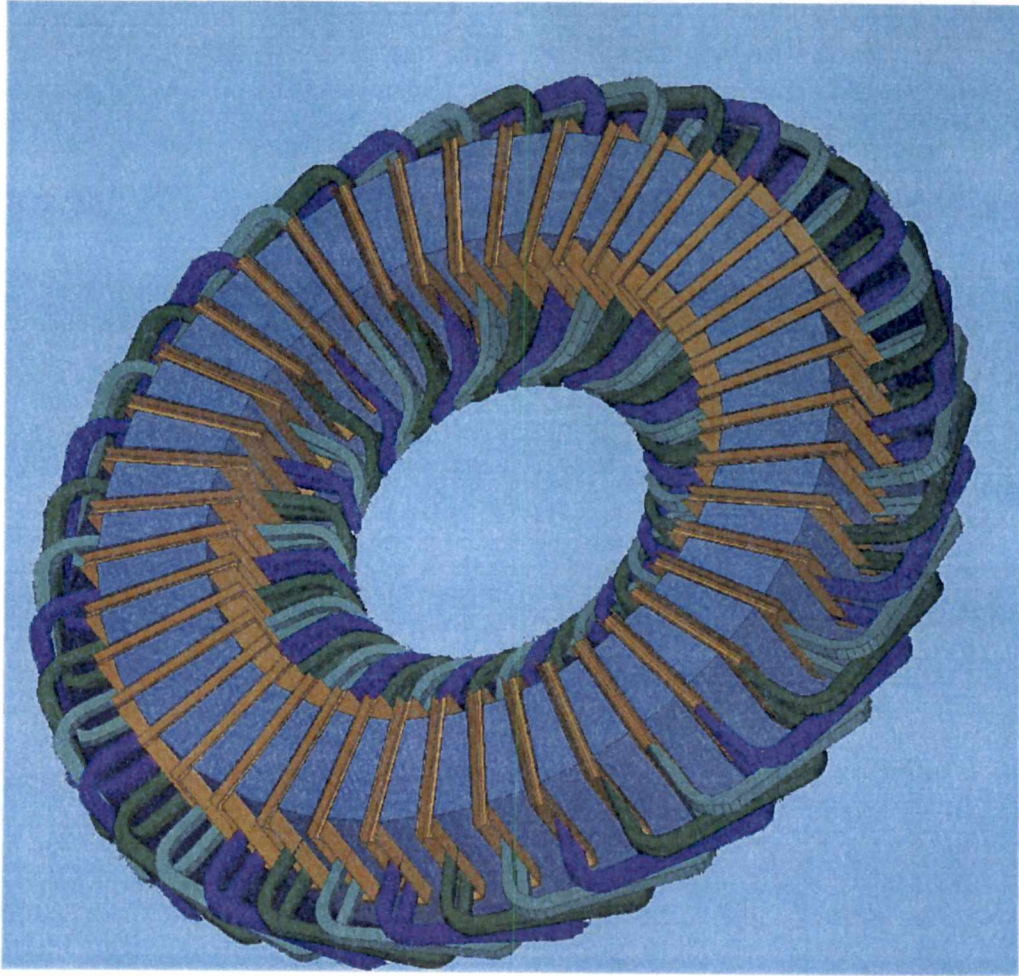


Figure 1.1: Conventional axial gap stator.

conductors per slot must be reduced to facilitate the placement of the winding due to conductor bunching at the inner radius. This reduction in slot area utilization results in higher copper losses. Another drawback to the stator design in Figure 1.1 is the maintainability of the current carrying conductors. In the event of a winding failure, it would be necessary to completely remove the stator assembly for rewinding.

To circumvent these shortcomings, a new axial gap electric machine is presented and analyzed in this dissertation. To facilitate this new geometry it is necessary to utilize a relatively new type of material to construct the stator. The next section explores the features of this new material and how it can be used to create alternate geometries for electric machine use.

1.2 Advances in Material Science

Many of the advances in electric machines have been the result of the development of better materials. Advances in core materials, permanent magnets and insulation have provided machine designers with materials to design lighter, more powerful and higher efficiency electric machines than ever possible before. With these advances in mind, the traditional machine structure can now be modified to create an modular machine where the structure supporting the flux also provides mechanical support. The use of *powder metallurgy P/M* techniques can be utilized to create a modular motor resulting in a more compact unit. The *powder metallurgy* materials possess several properties that make it particularly attractive to machine designers. Firstly, since it is produced in a bulk powdered form it is easily transported to the manufacturer where it must be molded into its final shape. The process of molding can be performed at the manufacturer's plant allowing one bulk material to be used for several different machine geometries. The molding process allows the generation of complex three-dimensional shapes with little post molding machine work. This particular structure would require little machining resulting in decreased production time, less wasted material and therefore a lower overall cost. One of the more beneficial features of

the material is its loss characteristics, particularly at high frequencies. In order to gain a better understanding of the impact of the P/M technology on core losses, a brief overview of the factors affecting magnetic material losses is given below.

Material Losses

The efficiency of all electric machines is directly proportional to the amount of loss within the system. The predominant losses in electric machines are: copper loss I^2R , hysteresis loss, eddy current loss and windage loss. The ability to minimize any or all of these losses improves the efficiency of the machine.

The hysteresis loss relates to the amount of energy loss due to traversing a B-H curve as shown in Figure 1.2. The empirical relation predicting the hysteresis loss in laminated steel is

$$P_{lh} = k_h V f B_m^n \quad (1.1)$$

where k_h is a constant of proportionality determined from the material properties; V is the volume of the core material used; f is the frequency at which the hysteresis loop is traversed. The exponent n is also a function of the material properties and generally ranges from 1.5 to 2.5. B_m represents the maximum value of flux density as depicted in Figure 1.2. Another form of equation 1.1 can be written as,

$$P_{lh} = k_h A_{loop} f \quad (1.2)$$

where A_{loop} represents the area of the loop traversed as the magnetic domains reorient themselves during a cycle.

Eddy currents arise from the changing B field inducing voltages and currents in the flux carrying material. Since the flux carrying material is electrically conductive, the currents induced result in a energy loss proportional to the current squared and the conductivity σ of the material.

CHAPTER 1. INTRODUCTION

For sinusoidally excited systems, the loss can be estimated based on the volume of the material V , frequency f , lamination thickness τ , maximum flux density B_m and a constant of proportionality $k_e(\sigma)$. The equation was empirically found by Steinmetz to be,

$$P_{le} = k_e V f^2 \tau^2 B_m^2 \quad (1.3)$$

It can be seen that equation 1.3 follows the square law in reference to applied or induced frequency. Therefore, for a given rate of change of the induced flux, the loss due to eddy currents is proportional to the square of the frequency. Generally, for soft magnetic materials used in electric machines, the area of the B-H curve traversed is small. Thus, the eddy current loss dominates the total core loss.

Given this fact, it is important to be able to predict and reduce the loss due to eddy currents in order to develop highly efficient electric machines. The use of *powder metallurgy* materials reduces the loss resulting from the flow of eddy currents. An electric machine designed to utilize this material is presented in this document. In addition, a new method to calculate eddy currents is also presented.

Although the particular machine described in this document was not designed to operate at high speeds; as power density requirements increase, the need to operate at higher flux levels and operating frequencies becomes a necessity. The tradeoff in operating at higher frequencies is the detrimental effect on the efficiency due to increased core loss. Figure 1.3 compares M-19 3% Si-Fe lamination steel with the Ancorsteel TC-80, the loss curves show that for operating frequencies above 1000 Hz, the Ancorsteel material is considerably less lossy. Even though the crossover point is effectively an 8-pole machine operating at 15,000 RPM, today's speeds reach in excess of 50,000 RPM. An 8 pole machine operating at 50,000 RPM would require a drive waveform frequency of 3,333 Hz and would result in about $3 \frac{\mu W}{cm^3}$ loss for the M-19 material as opposed to about $.75 \frac{\mu W}{cm^3}$ loss for the Ancorsteel TC80. This simple analysis neglects the effect of

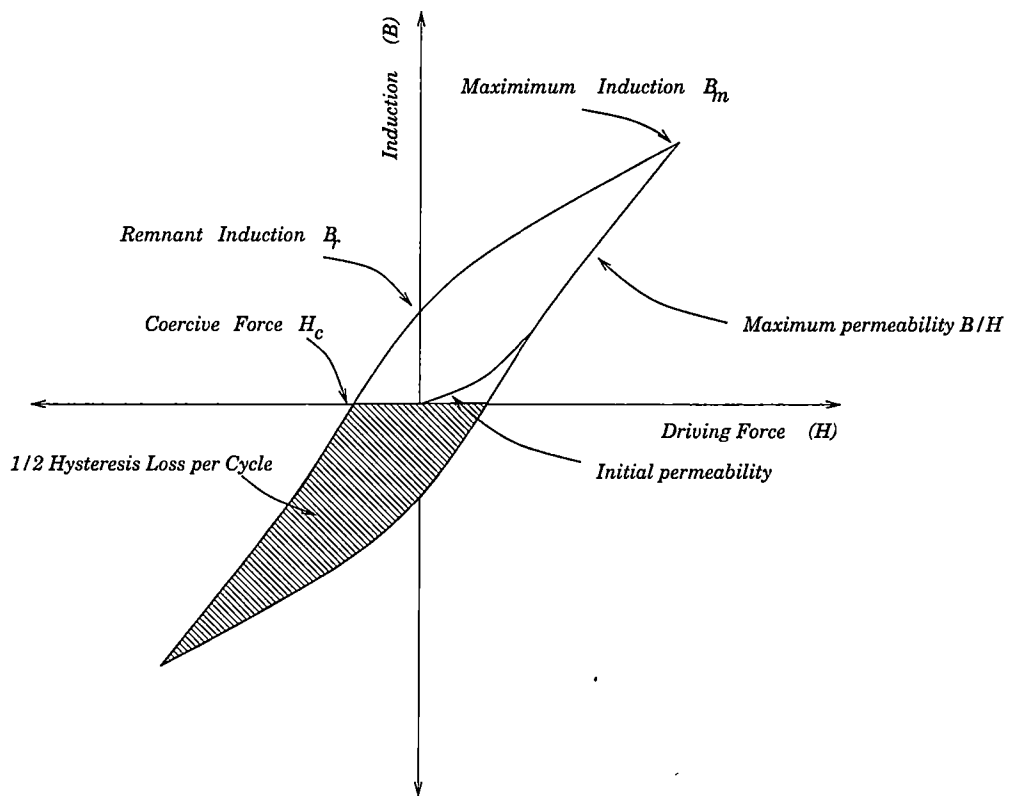


Figure 1.2: Typical B-H curve.

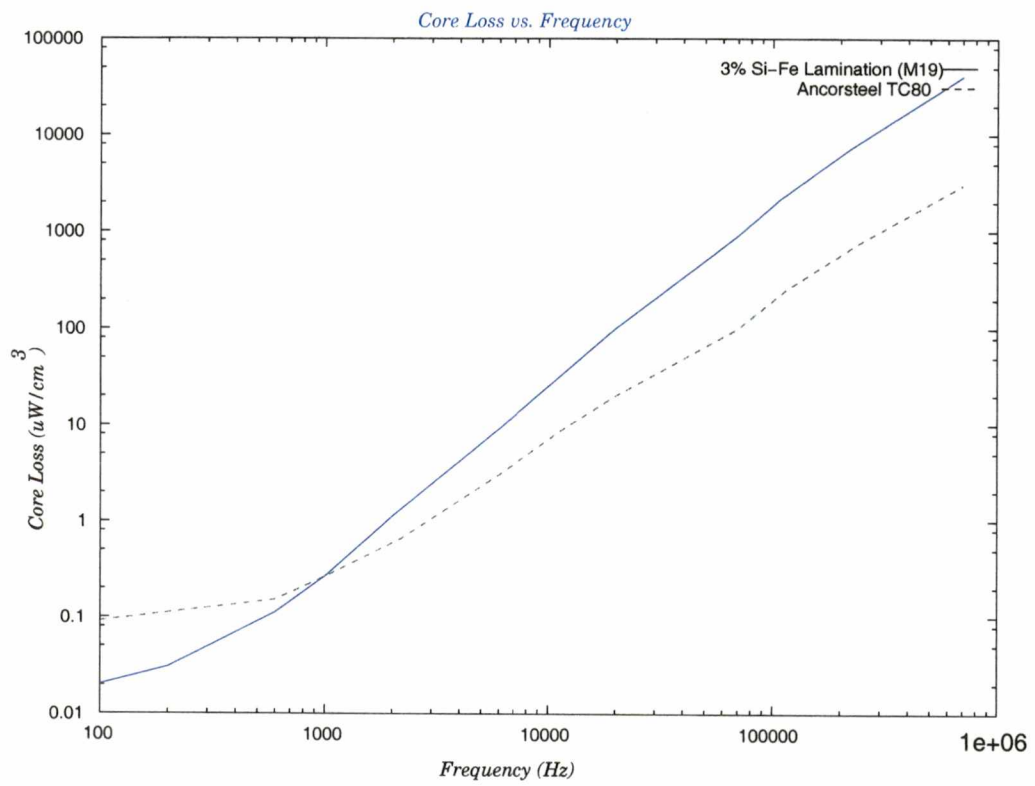


Figure 1.3: Core Loss of Ancorsteel TC-80 vs 3 % Si-Fe lamination.

harmonic frequencies on the loss and only performed utilizing one type of *P/M* material . The *P/M* technology provides a means to custom tailor the material for particular applications. For instance, the material properties may be altered to provide low loss in a range of frequencies specified by the designer. This is accomplished by altering the amount and type of ferrous material added to compound; this may be likened to the doping of semiconductor materials to alter the transfer characteristics of a transistor.

Material Permeability

The permeability of the magnetic material is a measurement of how easily the material is magnetized. At the atomic level, the permeability provides a quantitative measure of the ease at which the magnetic domains can be oriented in one direction. Soft magnetic materials are characterized by a high relative permeability μ_r , low coercive force H_c and a small hysteresis loop. Thus, given these qualities the preferred material used in electric machines are of this type.

The previous section presented an overview of the types of core losses found in electric machines. In addition, the loss properties of the TC-80 *P/M* material manufactured by Hoeganaes was presented. The TC-80 material provides a significant reduction of core loss at elevated frequencies. Unfortunately, the material possesses a very low initial and maximum relative permeability. The initial permeability of the TC-80 material is shown in Figure 1.4; the initial permeability represents the slope of the B-H curve at the beginning of the magnetization process and provides a measure of the amount of H necessary to initiate the magnetic flux B since $B = \mu_r \mu_o H$ where $\mu_o = 4\pi \times 10^{-7}$ and is the permeability of free space. After the initial magnetization process, the maximum value of the permeability for the TC-80 material is $\mu_{r_{max}} = 210$.

The low value of $\mu_{r_{max}}$ presents certain issues that are not usually considered in most electric machine designs. The majority of electric machines are designed with soft magnetic materials with relative permeabilities $1000 \leq \mu_r \leq 2000$. The low μ_r of the TC-80 results in the material having a high reluctance which impedes flux. The use of the low permeability material requires

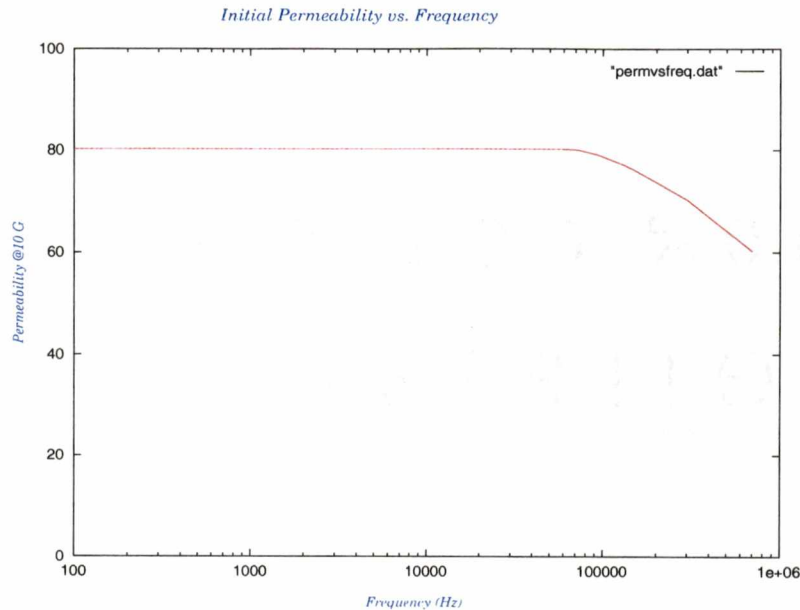


Figure 1.4: Initial permeability of Ancorsteel TC-80.

that the equation estimating flux reflect the additional reluctance as the flux passes through the members of the structure. The derivation for the air gap flux reflecting this change is developed for the slotted stator as well as for the machine described in this document.

1.3 Organization and Contributions

This dissertation is organized in the following manner:

- Chapter 2 describes the concept of a new type of modular electric machine where the stator not only provides the conduit for flux but also provides the mechanical support for the bearing and shaft assembly. The theory of operation and the relevant mechanical and electrical design equations are described and where necessary derived. In addition, alternate configurations are discussed.
- The machine's terminal characteristics are derived and correlated in Chapter 3. The ma-

CHAPTER 1. INTRODUCTION

chine was built and tested to verify the derived back-emf equation for the unusual round magnet/round salient pole machine structure.

- The study of any electromagnetic device begins with Maxwell's equations which have been presented in a variety of literature. Chapter 4 organizes and presents the equations in a manner relevant to the electric machine designer. The general form of Maxwell's equations are reduced to the cases for magnetostatic, quasi-static and magnetodynamic analysis.
- Chapter 4 provides the mathematical foundation for the numerical calculation of the B field under transient conditions presented in chapter 5. The discretization of the quasi-static form used in eddy current analysis is presented. In addition, the chapter provides an overview of finite-difference and finite-volume techniques as they apply to electrical engineering problems.
- To verify the numerical algorithm developed in Chapter 5, a 1D sample problem is solved in Chapter 6. A FORTRAN program is written to numerically solve the transient B field problem and is compared to the analytical solution.
- The appendices contain the schematics and software for the electric drive used to operate the modular motor. In addition, the derivation for the air gap flux as well as the simulation files are included there.

Several important contributions are contained in this document that are not only useful in the design of an modular electric machine but also pertain to the design and analysis of all type of electric machines. The major contributions presented in this dissertation are enumerated below:

1. Modular machine design concept - A new type of machine which can be molded inexpensively from *powder metallurgy* material is presented as are alternate configurations. The use of this material allows the molding of complex shapes including the mechanical structure

to support the shaft and bearing assemblies. The concept of creating a rotating machine without end bells and using the stator structure to support the bearings and shaft is unique as well as cost effective.

2. Analysis of counter emf - The equation that predicts the shape and magnitude of the generated voltage for an electric machine with disc shaped magnets rotating over round salient poles is presented. This is particularly important, since the round disc shaped magnets are easily obtainable in a variety of diameters and thicknesses. Furthermore, the use of the *P/M* facilitates the use of round pole pieces. Additionally, the counter-emf analysis is performed for the alternate wedge shaped configuration.
3. Estimation of flux - The development of the equations for estimating the flux in electric machines designed with low permeability materials. The equations are developed for the conventional axial gap configuration as well as for the salient pole derivative presented in this document.
4. Application of finite-volume methods - A new method to solve the eddy current problem is developed, explained and verified. As discussed in this chapter, the accurate prediction of eddy currents is necessary to estimate the efficiency of an electric machine. The method developed utilizes an explicit time-stepped method to calculate the eddy currents based on magnetic diffusion. The algorithm utilizes a simple data structure and can be easily integrated into a design/synthesis/analysis software package for axial gap electric machines.

Chapter 2

Design of the Machine

2.1 Motor Geometry

The use of powder metallurgy technology allows the formation of complex three-dimensional shapes. By utilizing this feature, a designer can construct unique shapes and address shortcomings that exist in present motor designs.

As previously mentioned, conventional machines are constructed from the following parts: laminated stator material, current carrying conductors, bearings, shaft and a physical structure to support the entire system. If a designer could eliminate any of the pieces that make up the system without adversely affecting the motor performance, a significant reduction in cost and complexity would result. A cutaway view of one such structure is shown in Figure 2.1, and represents a new concept in motor design.

The basic concept of the motor is to utilize the stator core to support the flux necessary for torque production as well as provide mechanical support. This is accomplished by either machining or pressing the bearing housings, pole pieces and mounting structure from P/M material. Ideally, in production, the stator core would be manufactured by pressing the P/M material into a mold. By utilizing the molding concept, the stator core would require only superficial machining

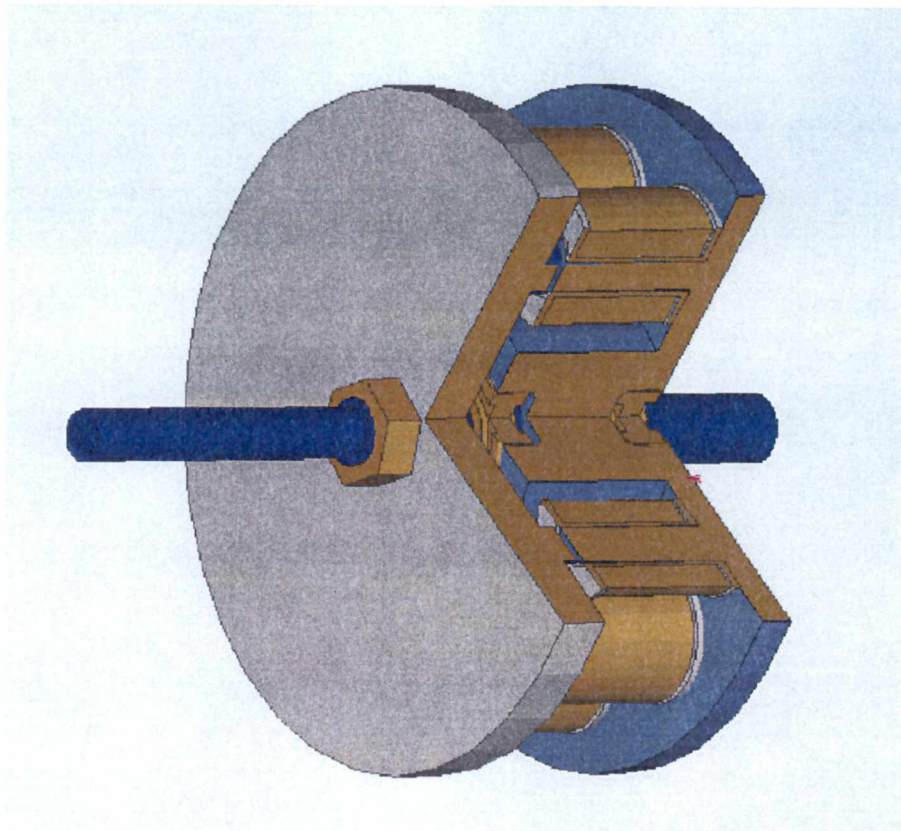


Figure 2.1: 3D solid model of modular motor.

to produce a finished assembly. Figure 2.2 represents an exploded view of the machine to better illustrate the various parts that constitute the modular motor.

Electric machines require three elements to produce torque: flux, current and a mechanical structure to support a rotating member. The flux in the modular motor is provided by permanent magnets embedded in the rotor. The rotor may be constructed from any type of high permeability ferrous material. As with any solid ferrous structure subject to an alternating field, losses result from the flow of eddy currents. Even though the magnets are mounted on the rotor and rotating at the same speed, the rotor is subject to induced currents resulting from armature reaction. Depending on the maximum speed of the machine, it is feasible to construct the rotor from the P/M material. The main concern being the centripetal forces acting on the molded rotor. Most high speed rotors are either machined from a solid billet or wrapped with carbon fiber to prevent them from disintegrating at elevated speeds.

The current in the machine is provided by insulated magnet wire wound on simple plastic bobbins similar to the type used in high frequency chokes. Finally, the mechanical structure is provided by the stator, shaft, front and rear bearings, locking nut and a rear circlip. Clearly, from Figure 2.2 it can be seen that the bearing races are supported by the one piece stator assembly and represent a departure from conventional motor designs.

There are several advantages to this design as opposed to a conventional axial gap machine constructed from amorphous tape. The comparison can be broken down into three areas: manufacturability, maintainability and cost. The discussion will focus on the attributes of the modular motor versus the conventional axial gap machine discussed in Chapter 1. A comprehensive discussion comparing the attributes of radial gap versus axial gap machines is presented by Krishnan [16].

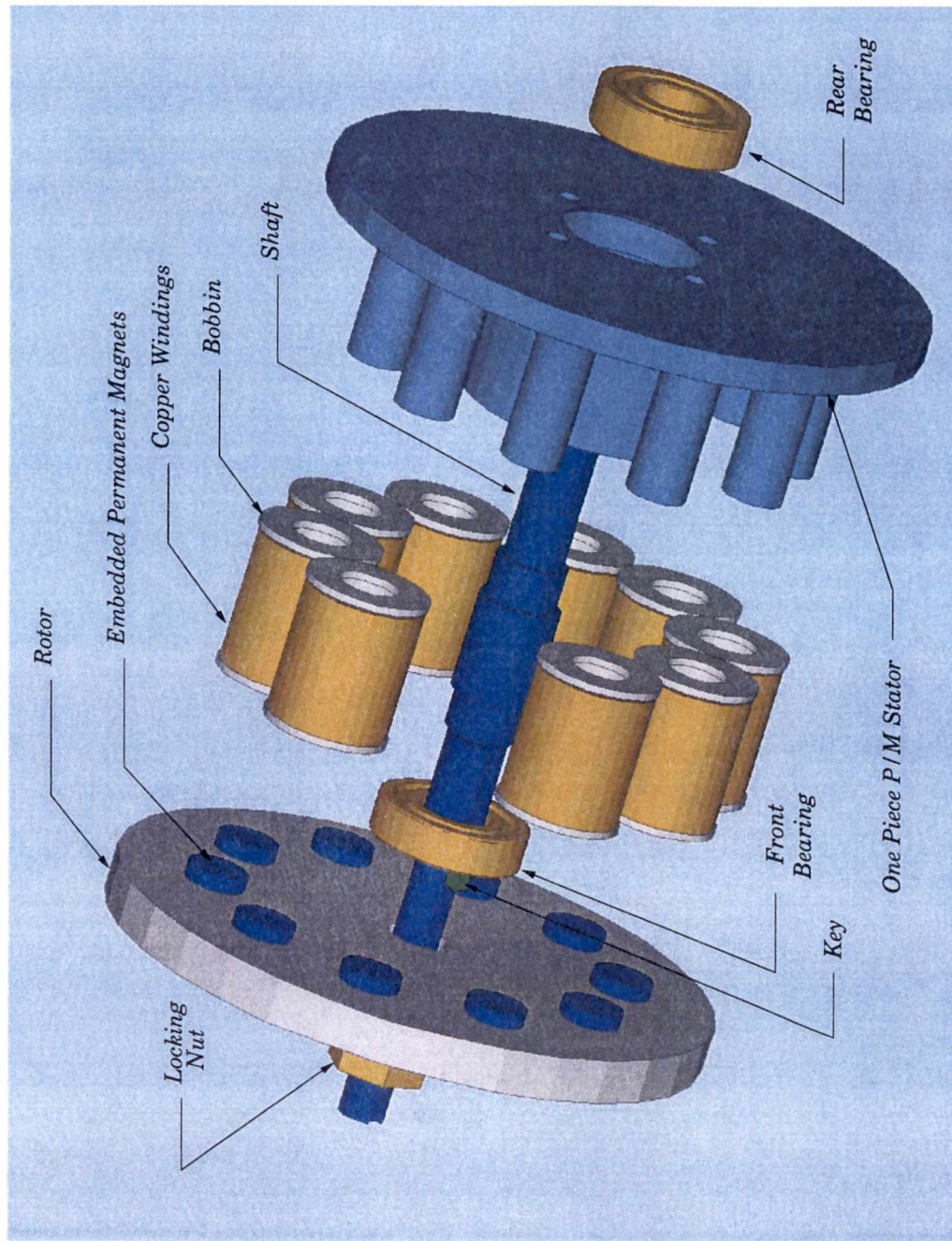


Figure 2.2: Exploded view of the modular motor.

Manufacturability

Conventional axial gap machines are generally constructed from a thin amorphous tape wound in a toroidal shape with the current carrying windings inserted in slots and wound to produce a spatially distributed flux. The slotting of the stator can be accomplished by either a specially designed indexed punch or by machining the toroid after it has been epoxied. In either case, the process does not lend itself to mass production. Additionally, even though the slots tend to be open or semi-closed, the windings are extremely difficult to place, particularly at the inner radius.

In contrast, the modular motor is pressed into shape from a metalized powder with salient pole pieces *en masse*. The use of round salient poles facilitate the use of winding bobbins similar to those used in switch-mode power supply transformers which are inexpensive and readily available. The cost associated with placing windings on this type of bobbin is very low due to its cylindrical geometry. Additionally, since the winding of a complete machine consists of several individual coils in series, each coil can be considered a separate part for manufacturing purposes; the implication of this is discussed below.

Maintainability

As depicted in Figure 2.1, the rotor is held into place by one threaded nut. The removal of this nut, coupled with the use of a gear puller to counteract the attractive force of the permanent magnets, allows a technician direct access to the windings. The windings, in the event of a failure, could be replaced *in situ* as opposed to the conventional axial gap machine that would require removal of the stator. In fact, each coil of the winding can be replaced individually as a result of the simple design. Since the coils are pre-wound and constitute their own entity, a repair facility could easily stock the coil assembly for field installation.

Cost

The cost associated with machining a part as opposed to pressing is well known and discussed in [13, 18]. The pressing process of the integrated machine is one step and requires little post-pressing machining. The time required to diagonally cut slots in the conventional epoxied toroid is lengthy and does not lend itself to automation. In addition, the time required to wind the conventional axial gap machine far exceeds the time necessary to place a pre-wound coil over the pole piece and make a connection.

2.2 Theory of Operation

The motor and control is designed to be as simple as possible since it is intended for low cost applications. Unlike most commercially available motors which are line operated, the modular motor requires a synchronized bipolar drive voltage. Thus, to produce even semi-continuous torque the modular motor requires an electronic commutating scheme synchronized to the relative position of the rotor magnets. To gain a better understanding of the torque produced by the machine; Figure 2.3 depicts the movement of the rotor magnets (filled circles) over the stationary pole pieces (hatched circles).

At rest, the natural or equilibrium rotor position is one of minimum energy, this condition occurs when the rotor magnets are aligned directly over the pole pieces. In Figure 2.3, the rotor position is shown to move from angle θ_0 to angle θ_3 , at angle θ_0 the rotor is at a position of instability. If rotated from the equilibrium position to $\theta = \theta_0$ and released, the rotor can either move in a positive $\theta = \theta^+$ or a negative $\theta = \theta^-$ direction due to the reluctance torque present in the machine, this reluctance torque is due to the large change in reluctance as the rotor turns. When the coils are energized, the process of continuous rotation can be described as follows:

If the rotor is assumed to be rotating in a θ^+ direction just past $\theta = 0$ and pole P^{1a} and pole P^{1b} are energized so as to produce south and north poles respectively, the rotor will be

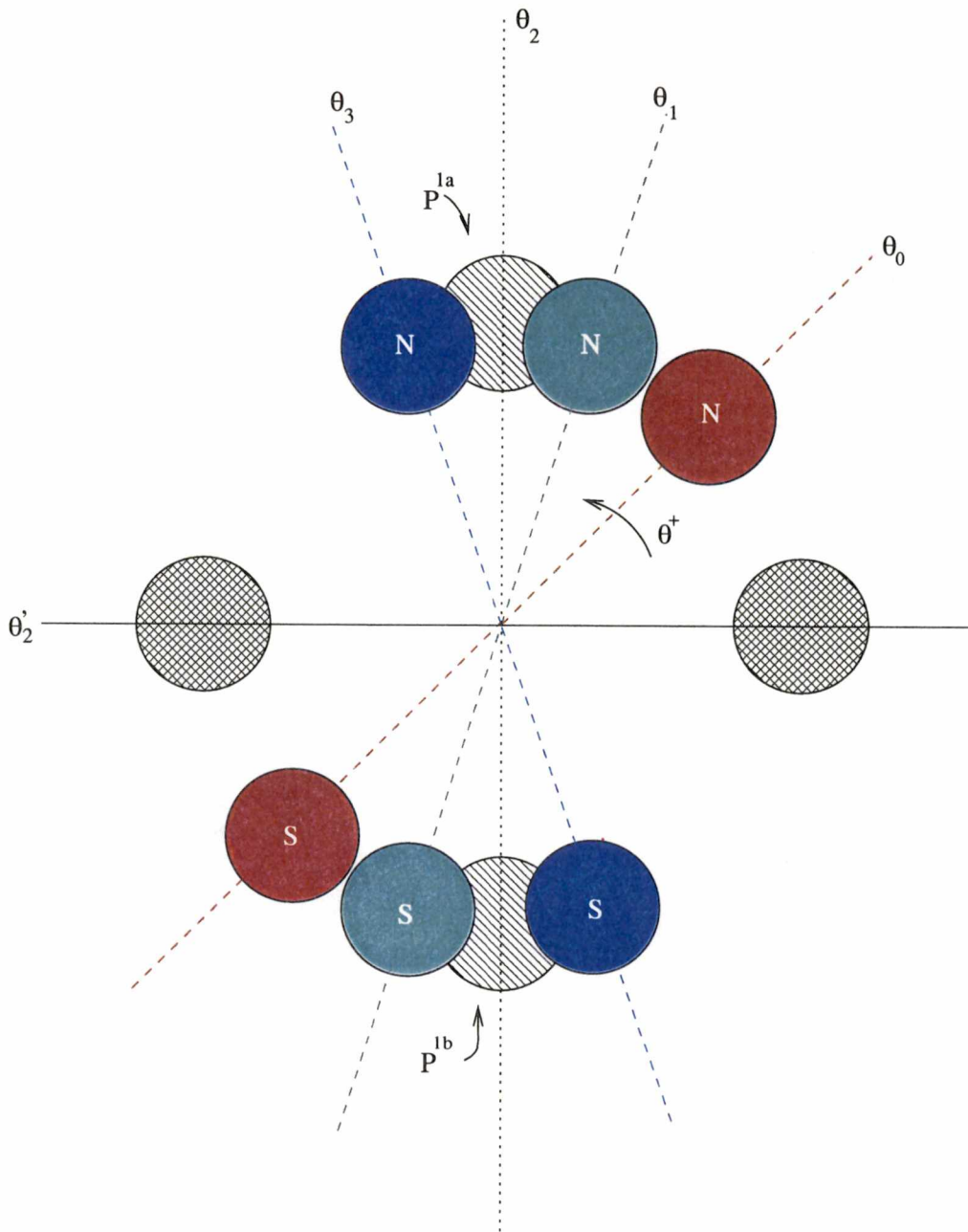


Figure 2.3: Movement of rotor magnets over stator poles.

drawn towards $\theta = \theta_1$ and subsequently towards $\theta = \theta_2$. As the rotor moves to $\theta = \theta_2$ the torque begins to decrease as the opposite poles become aligned. At this point the electronic commutation reverses the direction of the current in the stator coils and pole P^{1a} becomes poled in a northerly direction and pole P^{1b} directed southerly. This change in coil polarity causes the rotor to be repelled towards θ_3 and continues until θ'_2 ; whereby, the entire cycle repeats itself and continuous rotation is achieved. In this 4 pole example the commutation occurs every 90° ; whereas, in a P pole machine this would occur every $\theta_{sw} = \frac{360^\circ}{P}$ degrees.

To start the machine from rest it is necessary to properly energize the coils so as to cause rotation. Unfortunately, there is no way to know *a priori* the alignment of the poles. One solution is to employ an expensive absolute encoder for position feedback. This solution is very undesirable from a cost and reliability standpoint. Another solution is provided by software; the algorithm is designed to ignore any pulses from the relative encoder that result from rotation in the undesired direction. The implementation of the algorithm is simple, if the counter in the microcontroller is not counting upward after a slight delay, it may be assumed that the rotor is not moving, the polarity of the current is reversed and the switching pattern to cause continuous rotation in the desired direction is established.

2.3 Stator Design Equations

To properly design the stator, it is necessary to derive the equations that dictate the physical constraints of the machine. The design equations are based on first order approximations and neglect leakage flux. Since the machine is a salient pole design with relatively large distances between poles, any effect due to leakage flux will be minimal. The definitions of variables used to describe the physical geometry are given in the text and are summarized at the beginning of this document.

The relationship of the above quantities are depicted in Figure 2.4. The mean radius to a pole

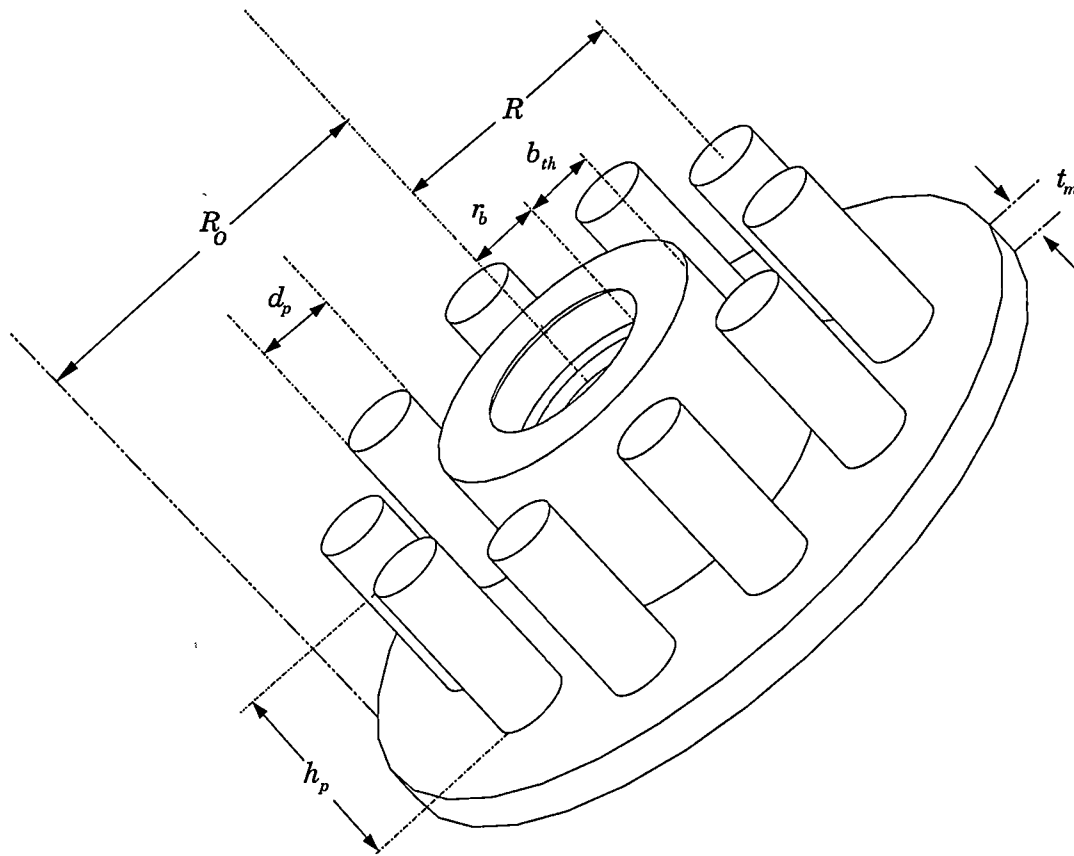


Figure 2.4: Stator physical dimensions.

center can be shown to be:

$$R = \frac{R_o - (r_b + b_{th})}{2}, \quad (2.1)$$

where R_o represents the outer radius of the machine, r_b the radius of the outer race of the bearing and b_{th} the thickness of the bearing wall. The mean radius represents the physical parameter relating the motor geometry to the magnitude of the back-emf and thereby, the torque of the machine.

Mean Magnetic Path Lengths

From Figure 2.5, it can be seen that $l_1 = l_5$, $l_2 = l_8$, $l_3 = l_7 = h_p$ and $l_4 = l_6$; therefore, the flux path lengths through the machine can be calculated. The flux path length through the rotor steel for an N_{mp} pole machine is,

$$l_{rs} = 2l_2 + l_1 = t_r + \frac{2\pi R}{N_{mp}}. \quad (2.2)$$

The length through the stator material can be shown to be:

$$\begin{aligned} l_{sm} &= 2l_3 + 2l_4 + l_1 \\ &= \underbrace{2h_p}_{\text{Pole path}} + \underbrace{t_m + \frac{2\pi R}{N_{mp}}}_{\text{Back iron path}}. \end{aligned} \quad (2.3)$$

Reluctance

The reluctance represents an impedance to flux much like a resistor to the flow of current. The total reluctance in a magnet circuit being driven by an magnetomotive force (MMF) determines the flux in the machine, the relation based on electric circuit analogies is,

$$\phi \mathfrak{R} = NI. \quad (2.4)$$

Here, ϕ is magnetic flux in webers and NI is MMF expressed in ampere-turns. Reluctance is proportional to the length of the magnetic path ℓ , the permeability of the material μ and the cross-section area a that the magnetic flux passes through and is defined as,

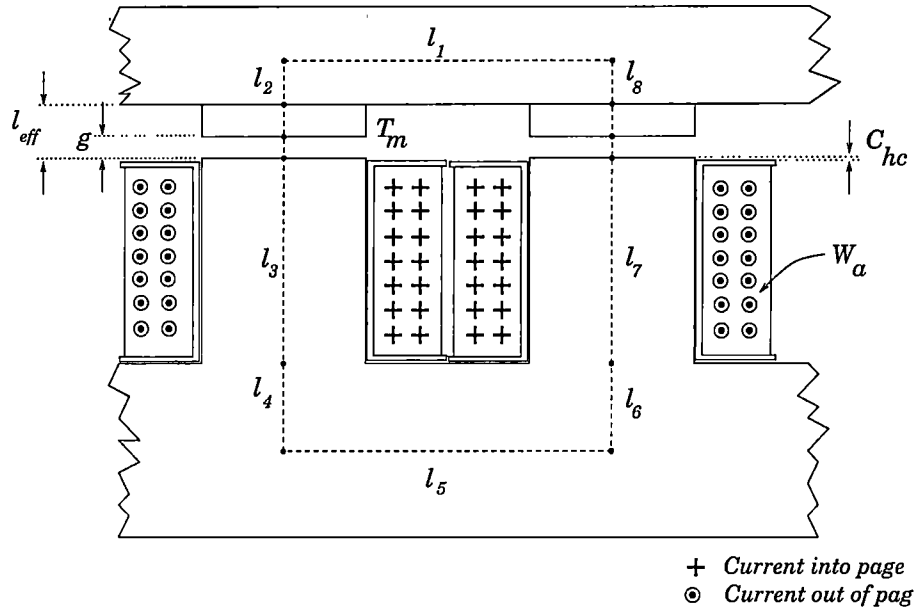


Figure 2.5: Mean magnetic flux paths.

$$\mathcal{R} = \frac{\ell}{\mu a}. \quad (2.5)$$

For the modular motor, the reluctance presented to the source MMF provided by the permanent magnets is,

$$\mathcal{R}_t = 2\mathcal{R}_{eff} + \mathcal{R}_r + \mathcal{R}_s. \quad (2.6)$$

Where the effective reluctance of the gap \mathcal{R}_{eff} is given by,

$$\mathcal{R}_{eff} = \frac{g + T_m/\mu_{rm}}{\mu A_p}. \quad (2.7)$$

In equation 2.7, A_p is the cross-section area of the pole piece, T_m the thickness of the magnet and μ_{rm} the relative permeability of the magnet. Similarly, the reluctance of the rotor \mathcal{R}_r can be found as,

$$\mathfrak{R}_r = \frac{t_r N_{mp} + 2\pi R}{\mu_{rr} N_{mp} A_{rotor}}; \quad (2.8)$$

here A_{rotor} represents the cross-section area of the rotor and μ_{rr} the relative permeability of the rotor material. The reluctance of the stator \mathfrak{R}_s is the sum of the reluctance of the salient pole piece and the yoke and is

$$\mathfrak{R}_s = \frac{2h_p}{\mu_{sm}\mu_o A_p} + \frac{t_m N_{mp} + 2\pi R}{\mu_{sm}\mu_o N_{mp} A_{yoke}}. \quad (2.9)$$

Equation 2.9 can be further simplified as,

$$\mathfrak{R}_s = \frac{2h_p N_{mp} A_{yoke} + t_m N_{mp} A_p + 2\pi R A_p}{\mu_{sm}\mu_o A_p N_{mp} A_{yoke}}; \quad (2.10)$$

where A_{yoke} is the cross-section area of the yoke and μ_{sm} is the relative permeability of the stator material.

Utilizing the expression for the total reluctance developed above, an equation representing the inductance of the winding can be derived.

Inductance

Since the stator is single phase with one winding, the inductance at the stator terminals is comprised of only a self-inductance term. Furthermore, there are two coils with N_{tc} turns per coil in the magnetic path; therefore, the self-inductance is given by

$$L = \frac{(2N_{tc})^2}{\mathfrak{R}_t}. \quad (2.11)$$

Air Gap Flux

The air gap flux and subsequently the flux density can be derived utilizing a reluctance model as derived in appendix A. By eliminating the leakage flux from equation A.4, the air gap flux for the modular motor can be calculated as,

$$\phi_g = \frac{4\phi_r \mathfrak{R}_m}{4\mathfrak{R}_m + 4\mathfrak{R}_g + \mathfrak{R}_s + \mathfrak{R}_r}. \quad (2.12)$$

Since the area of the magnet is equal to the area of the pole piece, equation 2.12 can be further simplified using \mathfrak{R}_{eff} as,

$$\phi_g = \frac{4\phi_r \mathfrak{R}_m}{4\mathfrak{R}_{eff} + \mathfrak{R}_s + \mathfrak{R}_r}. \quad (2.13)$$

Here, \mathfrak{R}_m represents the reluctance of the permanent magnet and is,

$$\mathfrak{R}_m = \frac{T_m}{\mu\mu_{rm}A_p}.$$

Similarly, the air gap flux density B_g can be estimated by,

$$B_g = \frac{4B_r \mathfrak{R}_m}{4\mathfrak{R}_{eff} + \mathfrak{R}_s + \mathfrak{R}_r};$$

where B_r is the remanent flux density of the magnet.

Winding Area

One of the more important aspects of the design is the available winding area. The winding area coupled with the diameter of the magnet wire determines the maximum amount of turns and thus the magnitude of the generated voltage. In addition, the number of turns and wire size directly affect the i^2R copper losses. The winding height is constrained by the height of the pole

piece h_p , bobbin thickness B_{wth} , and a clearance distance C_{hc} and can be shown to be

$$W_h = h_p - C_{hc} - 2B_{wth}. \quad (2.14)$$

By utilizing the law of cosines, the distance between poles and therefore the winding thickness can be found. The distance C between poles is

$$C = R\sqrt{2\left(1 - \cos\left(\frac{2\pi}{N_{mp}}\right)\right)}. \quad (2.15)$$

Subtracting the diameter of the pole piece d_p and two bobbin wall thicknesses; the thickness of the winding build is then

$$W_{th} = C - d_p - 2B_{wth} \quad (2.16)$$

$$= R\sqrt{2\left(1 - \cos\left(\frac{2\pi}{N}\right)\right)} - d_p - 2B_{wth} \quad (2.17)$$

Therefore, with the introduction of a winding fill factor k_w to account for the uneven packing of the magnet wires the winding area is,

$$A_w = k_w W_h W_{th} = k_w R (h_p - C_{hc} - 2B_{wth}) \left[\sqrt{2\left(1 - \cos\left(\frac{2\pi}{N}\right)\right)} - d_p - 2B_{wth} \right]. \quad (2.18)$$

Winding Resistance

The total resistance of the winding is calculated on the basis of a mean circumference of the bobbin and is,

$$r_w = \frac{N_{mp}\rho_{cu}(r_{ob} + r_{ib})}{4d_{wire}^2} \quad (2.19)$$

where d_{wire} is the diameter of the magnet wire, ρ_{cu} represents the conductivity of copper and r_{ob} , r_{ib} represent the outer and inner radius of the winding bobbin, respectively.

2.4 Design Variations

Due to the high reluctance of the core material, the magnet thickness necessary to produce a given flux density in the air gap is greater than that necessary for the same air gap flux density in conventional steel. Given this fact, the additional amount of reluctance due to an additional magnetic interface would only marginally increase the magnet thickness. By making this assumption, the pole pieces may be molded or machined in a variety of shapes and subsequently bolted in place. This concept would allow the designer to create several different pole face designs and would also provide improved mechanical support for the copper windings. A 3D solid model shown in Figure 2.6 illustrates this concept.

By altering the pole face geometry, the designer could reduce or even eliminate the cogging effect caused by the rapidly changing reluctance as a function of rotation angle. The cogging causes vibrations throughout the machine which results in the machine being far noisier acoustically than conventional machines of similar power rating. Consider Figure 2.5 showing a linearized version of the original design with round magnets and round pole faces. As the rotor moves to the right or left, the magnetic path length remains constant but the flux travels through air with a $\mu_r = 1$. Since the relative permeability of the stator material is several hundred times that of air, the rapid change in reluctance causes a detent torque. In servo applications this is generally advantageous; in constant speed applications this can cause stability problems. Figure 2.6 presents an alternate configuration where the pole face and the magnet are wedge shaped; the adjacent pole face is in close proximity so the variance in reluctance as a function of rotation angle is minimized. The area swept as a function of rotation angle θ increases linearly to a maximum when the magnet is directly over the pole face and decreases linearly as the magnet rotates towards the adjacent

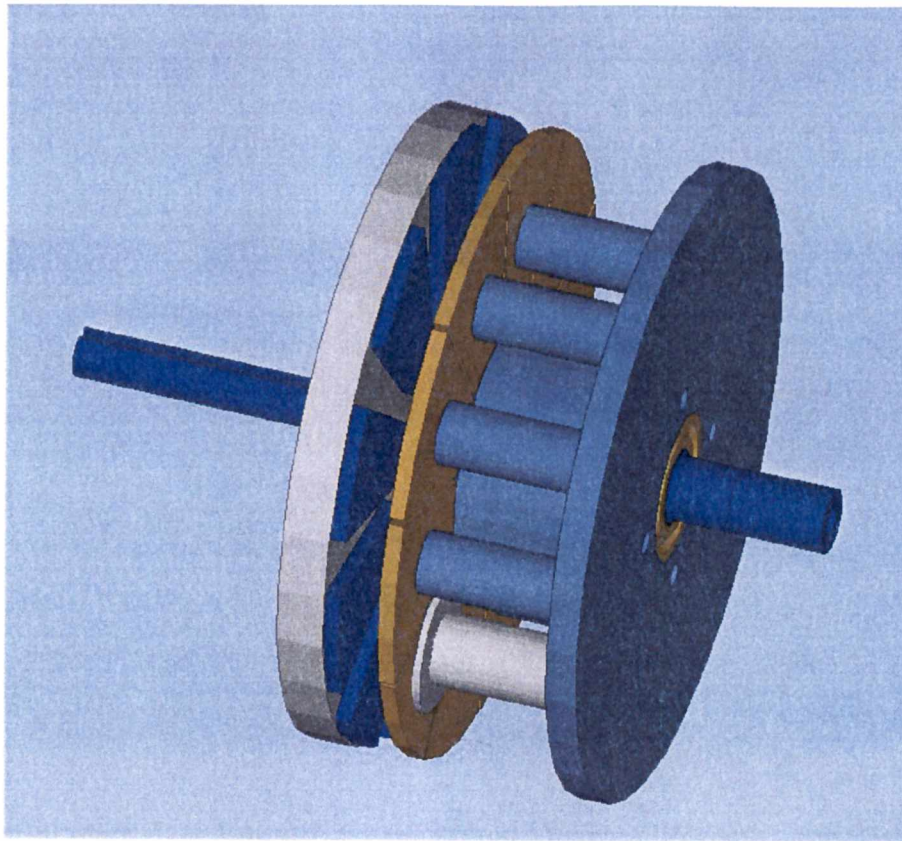


Figure 2.6: Square Back-emf Machine.

pole face. This linear change in area produces an approximate square-wave generated voltage, the derivation is given in Appendix B.

In certain applications where the cost of a rare earth magnet would be prohibitive, the stator could become a hybrid of the P/M for the pole pieces and traditional amorphous wound tape for the stator back-iron. In this arrangement, the amount of magnetomotive force required to overcome the stator reluctance would be small and a low cost ceramic magnet could be utilized.

2.5 Prototype Design

To prove the concept of the modular motor it was necessary to design, build and test a prototype machine. The prototype design was severely constrained by the availability of raw materials. Since the P/M material is generally molded at the customer's site, the only type of sample material supplied is in compacted form. The sample received was compacted from TC-80 powder in the shape of a cylinder with a height of 1.6 inches and a diameter of 5 inches. These dimensions, coupled with the use of readily available 0.5 inch diameter plug magnets dictated the design of the prototype. The stator was designed with the constrained dimensions of the sample material to have a rotor magnet leaving a pole just as the adjacent magnet enters a pole. The main purpose is to create a continuous generated voltage as the rotor rotates. Since the flux from the magnet is directed perpendicular to the magnet face, if a magnet does not enter another pole as one leaves, the flux will diminish and flat spots will occur in the generated voltage. The closest integer pole pair number that would enable the proper distance between adjacent poles was $N_{mp} = 10$. Therefore, the prototype represents a proof of concept and does not constitute an optimal design. The drawings for the prototype machine appear in Appendix E.

Rotor

The rotor needs to be able to sustain a flux density of approximately 1.3 Tesla and be of high permeability. Given these broad constraints, the material for the rotor was chosen from several scrap flat plates by empirically testing the retention of a permanent magnet to the face of the plate. The amount of force necessary to remove the magnet provided a relative measure of the permeability of the material, with the higher force being associated with a higher permeability. Based on prior experience, it is believed that the permeability of the rotor material $\mu_{rr} \geq 500$.

The rotor was machined into a disc shape, bored and keyed to the proper dimensions. Additional machining included boring 10 equally spaced counter-sunk holes on the disk face to provide

mechanical support for the magnets. The counter-sunk holes were chosen to provide mechanical support as opposed to a more costly magnet retainer machined from a non-magnetic material.

Stator

As mentioned above, the sample of the TC-80 material was preformed in the shape of a cylinder. Therefore, to obtain the shape shown in Appendix E extensive machining operations were required. First, the center of the cylinder was bored out to the proper dimension. The purpose of this operation was twofold; firstly the hole is required by the drawing and secondly to determine the machining qualities of the material. It was found during this operation that the material is somewhat difficult to machine with conventional cutting tools but grinds using abrasives quite well. Unfortunately, due to the shape of the stator, grinding the cylinder into its final form would be cost prohibitive.

The process of machining the cylinder into the final form was straightforward with the exception of the salient pole pieces. Due to their shape and offset from the centerline of the cylinder, an offset rotary table was used in conjunction with a milling machine to accomplish this task. The final machining operations were performed to drill and tap the stator mounting holes. This operation was performed easily and was found to provide excellent retention of the mounting bolts.

Although there were difficulties in machining the bulk material, it should be noted that the mass production of the modular motor would be based on the use of a mold to create the final shape; therefore, requiring little or no machining.

Shaft and Bearings

The design of the shaft for the prototype machine was based on the bearings chosen and the bore available in the stator. The bearings were arbitrarily chosen as standard 203 style bearings commonly found in fractional horsepower electric motors. In addition to providing the bearing

surfaces, keyway and encoder shaft hole, the shaft contains a groove at the rear for the circlip and threads at the front to secure the rotor via a locking nut. The shaft was machined to the proper dimensions from cold-rolled shaft stock.

Assembly

The assembly of the machine is simple. The rear bearing is lightly tapped into the stator housing, the shaft inserted and the rear circlip secured. The front bearing is then lightly tapped into place and the individual coils are installed over the salient pole pieces. Before the rotor and keyway are installed, the shims determining the air gap are placed over the shaft. Next, the rotor is installed using a gear puller to counteract the attraction of the rotor to the stator pole faces. Finally, the locking nut is securely tightened.

Summary

The equations presented in this chapter provide a basis for the design of the prototype modular motor. The prototype modular motor was designed and built according to the drawings given in Appendix E. The next chapter presents the equations representing the generated voltage as well as torque. In addition, experimental results are provided for the machine described in this chapter.

Chapter 3

Machine Performance

The amplitude and shape of the back-emf plays an important role in the performance of permanent magnet machines. The amplitude determines the range of speed over which the machine can operate with constant torque from a fixed bus voltage. The shape of the back-emf coupled with the shape of the driving voltage determines the amount of torque ripple. Depending upon the inertia of the load, the torque pulsations can cause instabilities in closed loop systems. The ability to determine analytically the waveform for the back-emf is paramount in determining the current, power and torque. The expression for the back-emf is analyzed and used to develop a torque expression. To accurately predict the amplitude of the back-emf, the value of the air gap flux must be known. The expressions for back-emf, air gap flux and torque are developed and the experimental results are discussed below.

3.1 Analysis of Back-EMF

To calculate the counter-emf or generated voltage of the machine it is necessary to develop the expression for the area swept by the magnet as a function of rotation angle ψ as depicted in Figure 3.1. The complete derivation is shown in appendix B. The area swept as the rotor magnet

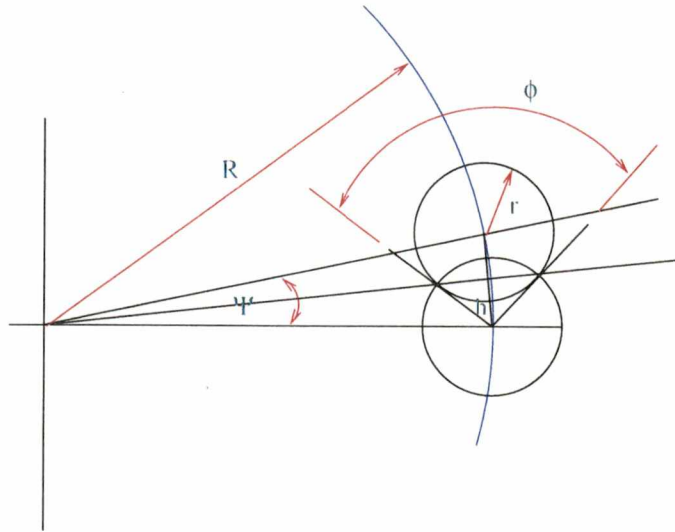


Figure 3.1: Magnet sweeping area over pole face.

moves over the pole face is

$$A_{sw} = 2 \left[\cos^{-1} \left(\frac{R \sin \left(\frac{\psi}{2} \right)}{r} \right) r^2 - R \sin \left(\frac{\psi}{2} \right) \sqrt{r^2 - R^2 \sin^2 \left(\frac{\psi}{2} \right)} \right], \quad (3.1)$$

and is valid for:

$$\psi \leq 2 \sin^{-1} \left(\frac{r}{R} \right). \quad (3.2)$$

The generated emf is given by:

$$e = -N_{tc} \frac{d\phi}{dt}, \quad (3.3)$$

where ϕ is the flux in Webers and given by $\phi = BA$, B is flux density and considered constant, N_{tc} is the number of turns per coil:

$$e = -N_{tc} B \frac{dA}{dt}, \quad (3.4)$$

which may also be written as:

$$e = -N_{tc} B \frac{dA}{d\psi} \frac{d\psi}{dt} = -N_{tc} B \frac{dA}{d\psi} \omega_m, \quad (3.5)$$

and for a machine with N_{mp} magnet poles,

$$e = -N_{tc}N_{mp}B \frac{dA}{d\psi} \frac{d\psi}{dt} = -NN_pB \frac{dA}{d\psi} \omega_m. \quad (3.6)$$

Taking the derivative and substituting into equation 3.6 the expression for the generated voltage as a function of mechanical degrees is,

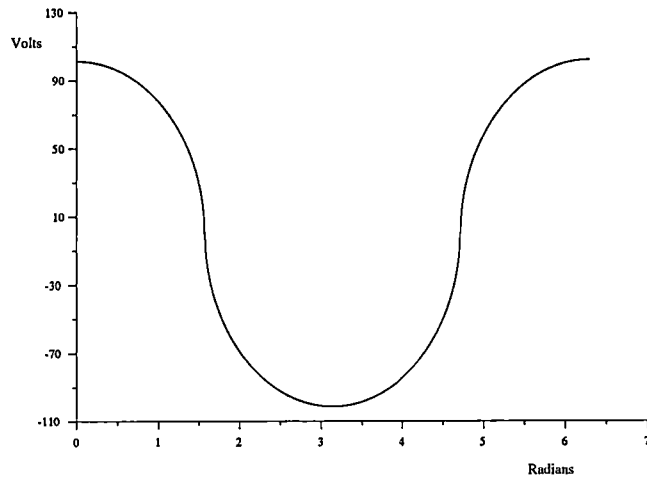
$$e = \frac{-N_{tc}N_{mp}B\omega_m}{\sqrt{r^2 - R^2 \sin^2\left(\frac{\psi}{2}\right)}} \left[\left(\frac{R^3}{2}\right) \left(\sin\left(\frac{\psi}{2}\right) \sin(\psi) - \cos\left(\frac{\psi}{2}\right) \cos(\psi) + \cos\left(\frac{\psi}{2}\right)\right) - 2r^2R \cos\left(\frac{\psi}{2}\right) \right]. \quad (3.7)$$

Since equation 3.7 is only valid for the condition given in equation 3.2, it was necessary to create a full cycle waveform from the quarter cycle data. A Scilab file, shown in appendix F, was created to plot and perform an FFT on the full cycle waveform. Figure 3.2 shows a full cycle of the generated voltage produced by adding two sections, one inverted and shifted by π , of equation 3.7 together. By inspection, it also reveals a large harmonic content which is a result of the circular magnets rotating over the circular pole pieces. To support the assumption that the waveform is rich in harmonics, a fast fourier transform was performed on the full cycle data.

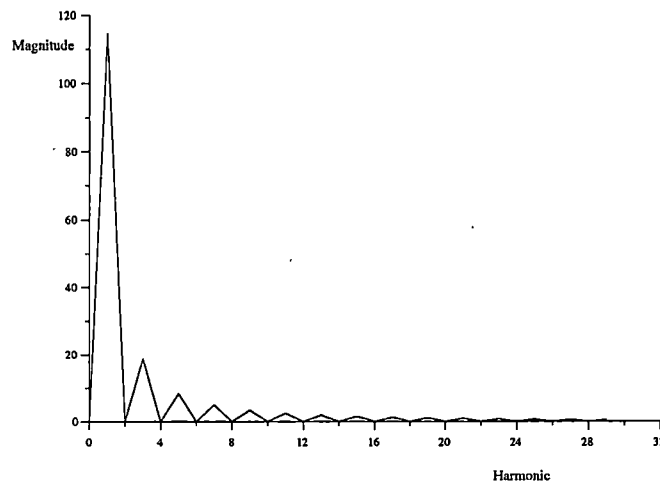
The FFT of the generated voltage waveform is shown in Figure 3.2 and reveals the concentration of odd harmonics with significant amplitudes up to the 25th harmonic. With the use of the results of the FFT, an approximate waveform can be constructed from the harmonics. By defining a normalization factor $k = N_{tc}N_pB\omega$, the normalized voltage is represented by

$$\bar{A}_n = \frac{A_n}{k}. \quad (3.8)$$

Table 3.1 gives the result for the first 8 odd harmonic terms of the Fourier expansion for



(a) Full cycle of generated voltage



(b) FFT of generated voltage

Figure 3.2: Numerically generated no load waveforms.

Table 3.1: Magnitudes of odd harmonics.

n	A_n Amplitude (V)	\bar{A}_n Normalized (μV)
1	114.55	620.44
3	18.56	100.54
5	8.29	44.92
7	4.92	26.64
9	3.32	17.00
11	2.43	13.19
13	1.87	10.15
15	1.50	8.13

$N_{tc} = 120$, $N_{mp} = 10$, $B = .60 T$, $\omega = 256.4 \frac{rad}{s}$, $R = 0.0432 m$, $r = 0.00635 m$ and for the normalized case.

By utilizing the normalization factor k , the approximating equation becomes:

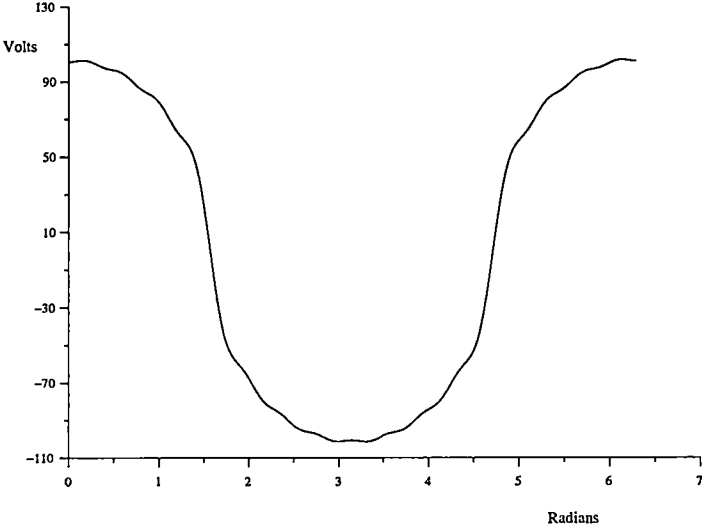
$$e = k \sum_{n=1,3,5,7..}^{nmax} \bar{A}_n \cos \left[\frac{nN_p \omega_m t}{2} + (n-1) \frac{\pi}{2} \right], \quad (3.9)$$

where for this particular case $k = 184600$.

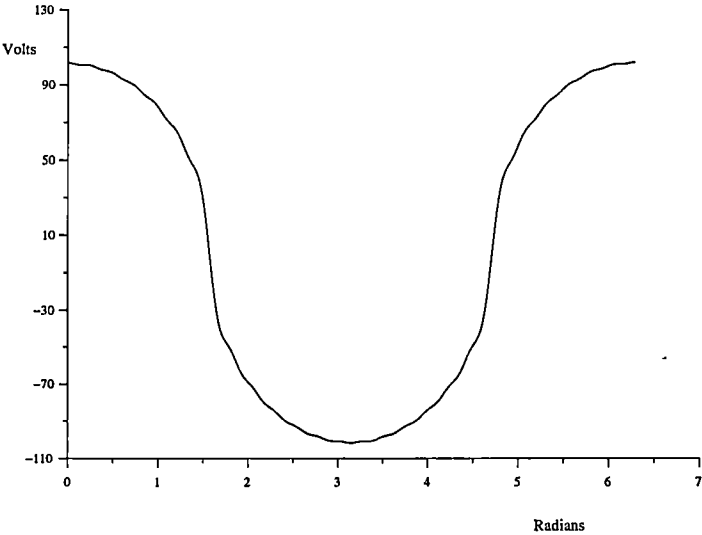
A plot of the odd harmonics up to $n = 15$ and $n = 25$ is shown in Figure 3.3. With $n = 15$ the resulting waveform is quite distorted; with the inclusion of odd harmonics up to the 25th, the approximating waveform more closely resembles the analytical expression for the generated voltage.

3.2 Torque

The prediction of the generated torque and torque ripple is necessary to determine the suitability of a particular machine to an application. The torque of an electric machine can be calculated from the microscopic point of view or the macroscopic. In the microscopic case, the torque is calculated by applying the Lorentz force law,



(a) Approximate waveform with $n=15$



(b) Approximate waveform with $n=25$

Figure 3.3: Plots of approximating waveforms.

$$\hat{F} = q (\hat{v} \times \hat{B}) \quad (3.10)$$

$$d\hat{F} = i d\hat{l} \times \hat{B} \quad (3.11)$$

From the macroscopic view, the torque can be calculated by utilizing conservation of energy principles; the mechanical torque in any machine is,

$$T = \frac{P}{\omega_m}. \quad (3.12)$$

The instantaneous power developed by the machine is $P(t) = ei$; thus, using equation 3.12 the torque is given by

$$T = \frac{ei}{\omega_m}; \quad (3.13)$$

utilizing equation 3.9 and equation 3.13 an expression for the torque in terms of the approximated waveform can be written as,

$$T = iN_{tc}N_{mp}B \sum_{n=1,3,5,7..}^{nmax} \bar{A}_n \cos \left[\frac{nN_p\omega_m t}{2} + (n-1)\frac{\pi}{2} \right]. \quad (3.14)$$

3.3 Experimental Results

To verify the derived equations, the motor was driven as a generator by another machine at various speeds. The test was performed by coupling a DC motor to the experimental machine and monitoring the open circuit and loaded voltages by a digital oscilloscope and current probe; the experimental test setup is shown in Figure 3.4. Several different windings were used to extract data from the machine. Winding data for two separate cases is given in Table 3.2. A plot of the

Table 3.2: Winding parameters.

	Winding #1	Winding #2
# of turns per coil	120	16
Poles	10	10
Total # of series turns	1200	160
Wire size	2 #24 in series with 1 #21	2 #16

experimentally determined voltage for winding #1 is shown in Figure 3.5. Figure 3.6 depicts the voltage waveform created from equation 3.9.

The shape of the voltage waveform shown in Figure 3.5 differs from the analytically derived waveform particularly at the peaks. The peaks represent the change from a positive slope to a negative slope. In terms of the machine, this represents the point at which the magnet is first beginning to overlap the pole piece. In the case of the modular motor, there is a mechanical dead space between poles where the rotor magnet is not overlapping either pole face. Therefore, if no area is swept as a function of rotation angle there cannot be any generated voltage as supported by equation 3.6. Also, since the B field is directed along the shaft of the machine, the flux does not bridge the void between the two poles. The mechanical void was not taken into consideration in Figure 3.6; it may be accounted for by modifying the weight of the third harmonic in equation 3.9. It will be shown later that when there is a disturbance of the air gap flux, the slight voltage drop is diminished.

The experimentally determined voltage data was numerically integrated to determine the flux linkage and is shown in Figure 3.7. The averaging effect of the integration smoothed the rapidly changing peak in Figure 3.5.

Winding #1

The first winding of 120 turns per coil was wound on 10 bobbins machined from Delrin™, an easily machined insulating material. The air gap for the test was set at 0.038” which was the minimum gap for which the Hall probe could be inserted between the pole piece and magnet. The

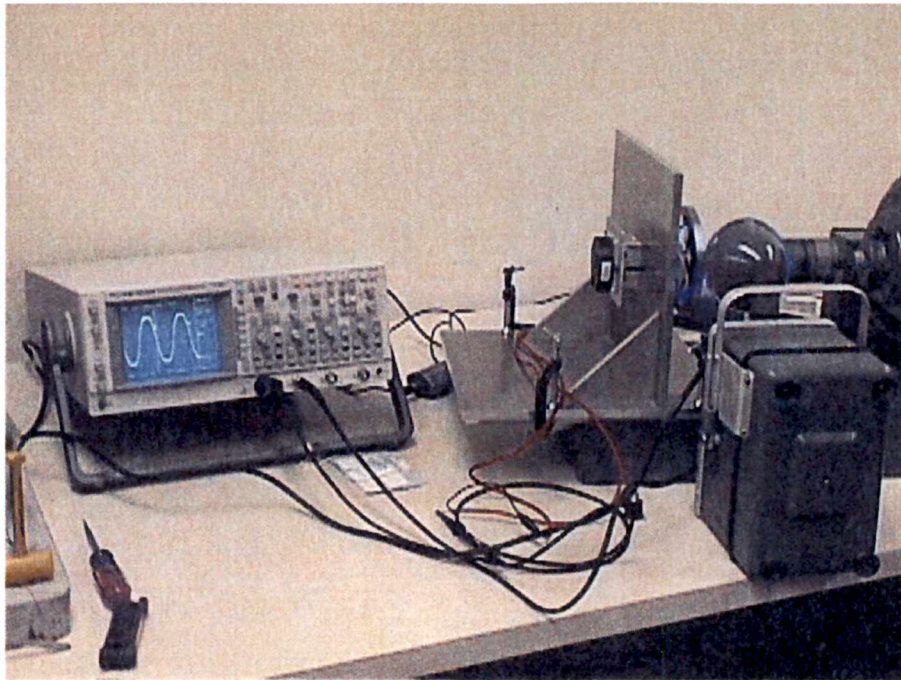


Figure 3.4: Experimental test setup.

modular motor was accelerated to $2975 \frac{rev}{min}$ where the open circuit voltage was recorded and is depicted in Figure 3.8. In addition, the figure contains the FFT of the generated voltage illustrating the harmonic content. In particular, it can be seen that the third harmonic is proportionally larger in reference to the fundamental in Figure 3.8 than in Figure 3.2. While running at $2975 \frac{rev}{min}$, the winding was resistively loaded to $I_{rms} = 0.2$ Amps; the result is shown in Figure 3.9a. It can be observed that the voltage dip at the peak of the waveform is slightly smaller than the dip in the open circuit voltage. This is due to armature reaction disturbing the air gap flux. Figure 3.9b was recorded with $I_{rms} = 1.6$ Amps and shows the distortion of the waveform due to the disturbed flux. In addition, the figure shows the effect of the coil resistance reducing the output voltage. The high resistance of the winding is due to the large number of turns per coil with small magnet wire. To reduce the amount of coil resistance, another winding with fewer turns and larger wire was built and is discussed below.

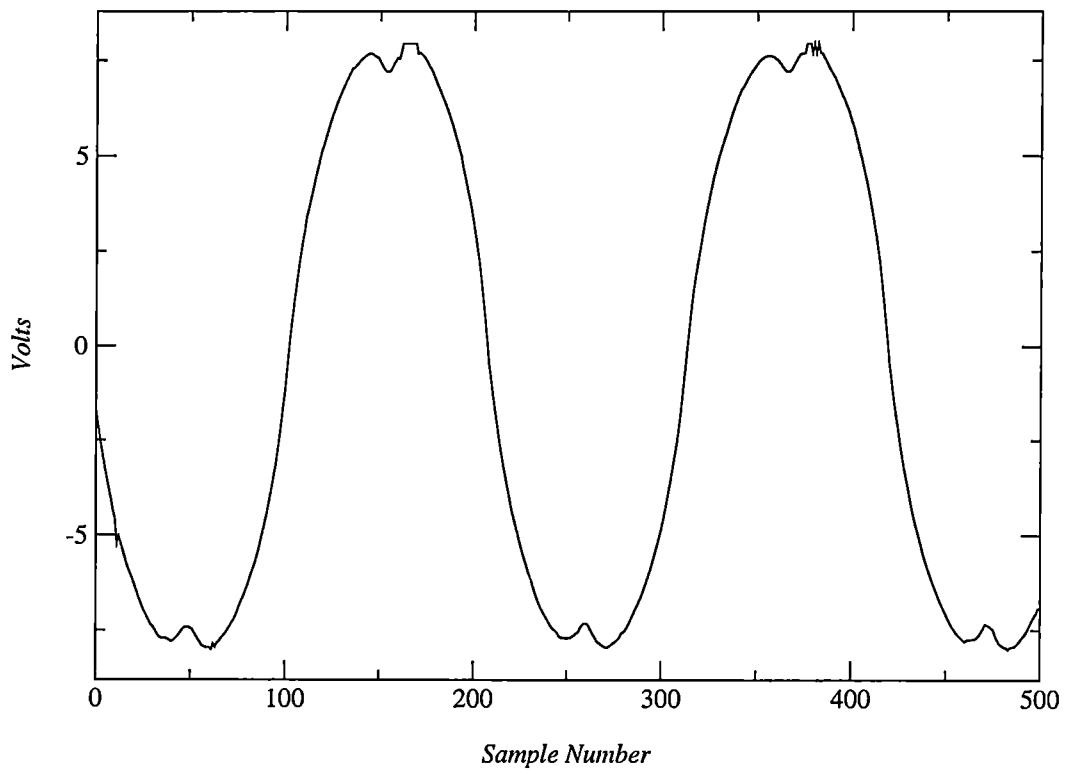


Figure 3.5: Experimentally determined voltage.

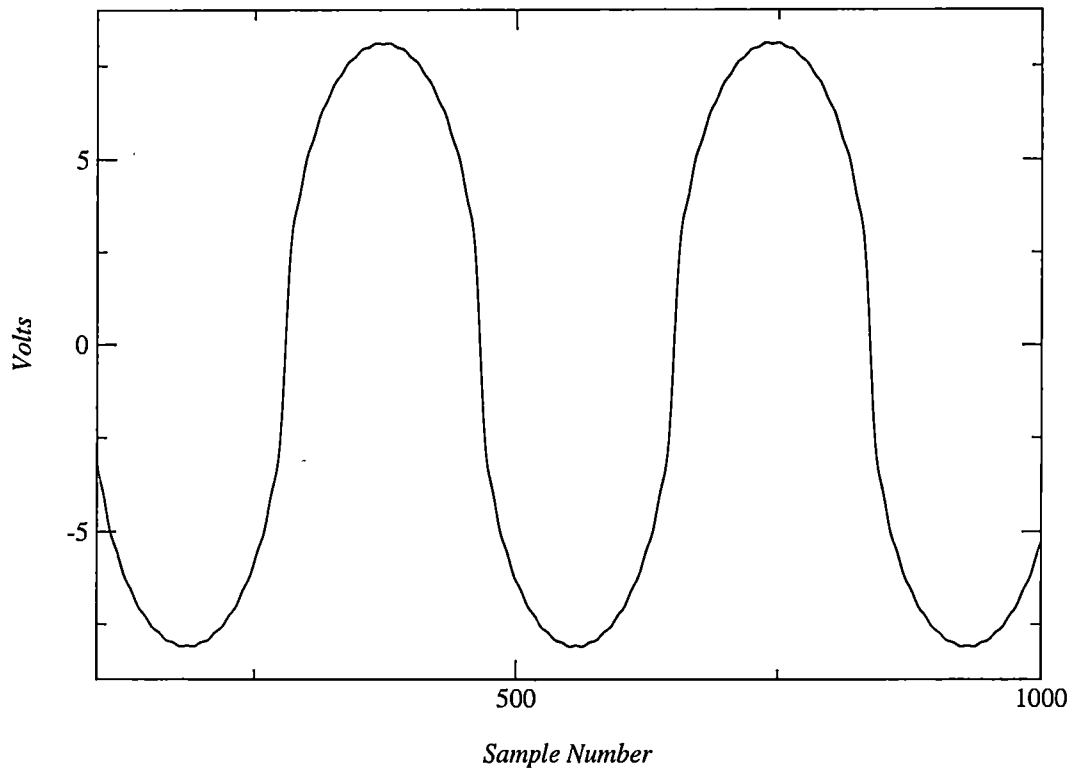


Figure 3.6: Waveform created from approximating equation.

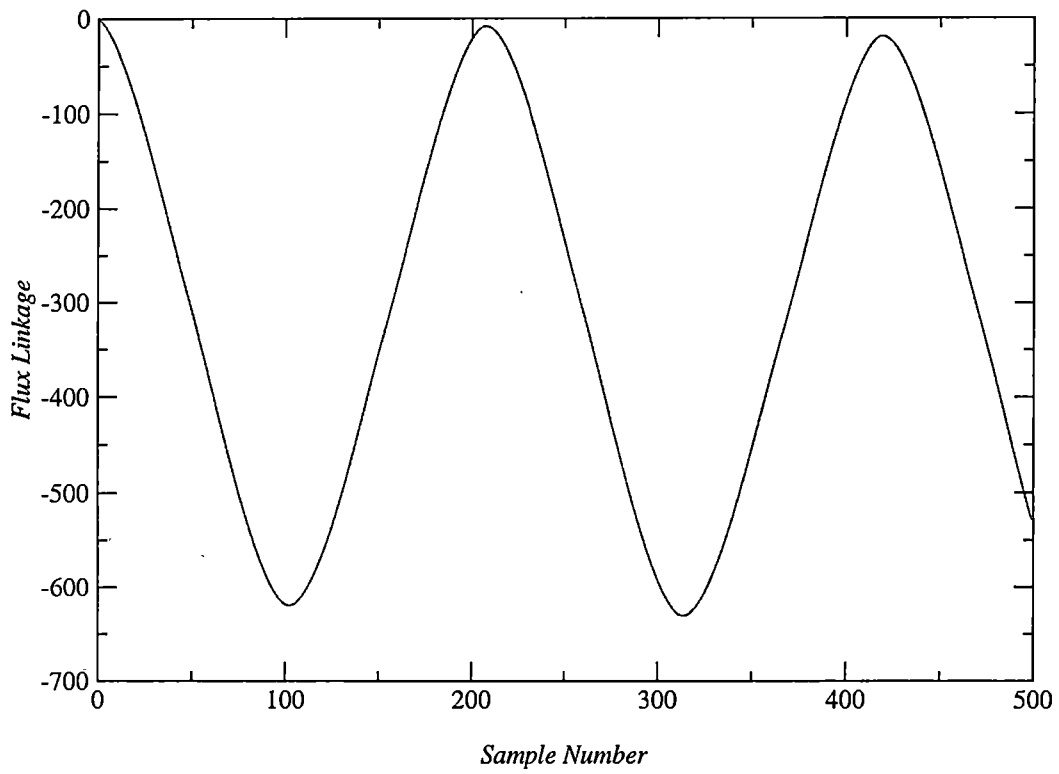
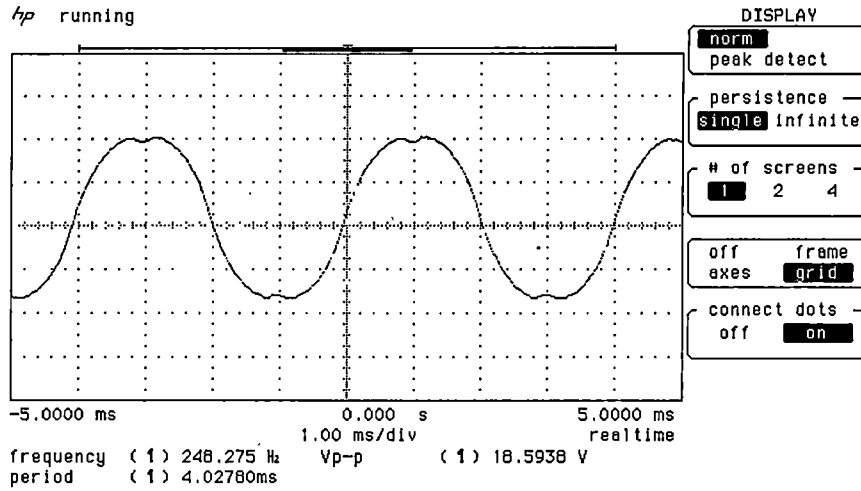
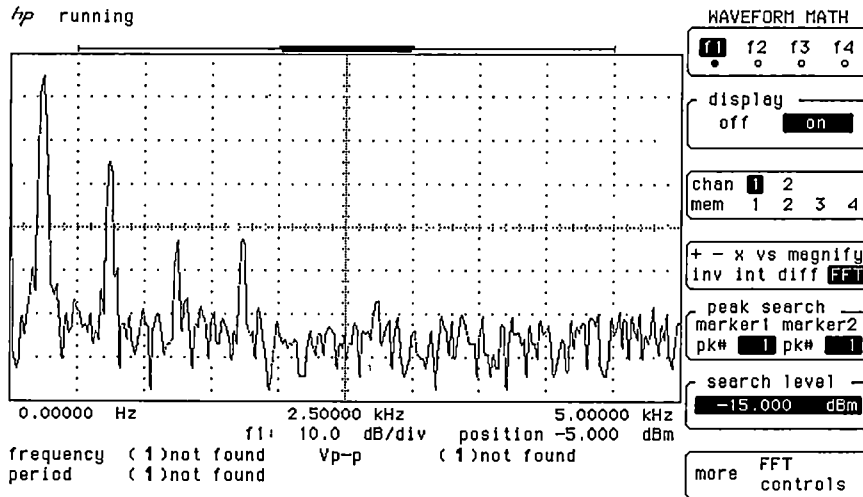


Figure 3.7: Flux linkage of experimentally determined waveform.

CHAPTER 3. MACHINE PERFORMANCE

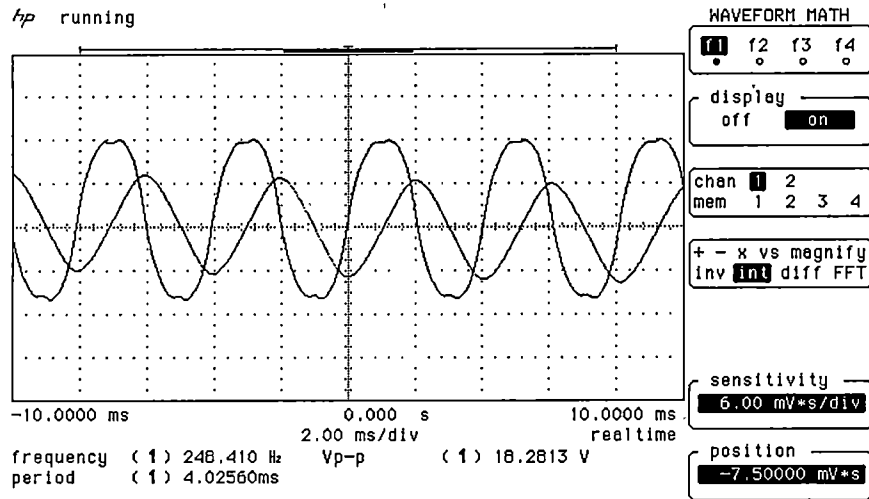


(a) Open circuit voltage.

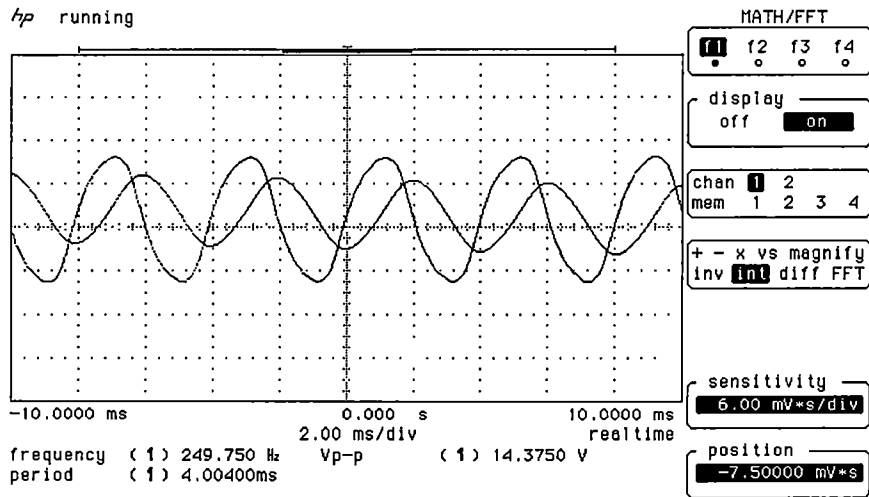


(b) FFT of open circuit voltage.

Figure 3.8: Experimentally determined voltage at 2975 $\frac{rev}{min}$.



(a) Terminal voltage with $I=0.2A$



(b) Terminal voltage with $I=1.6A$

Figure 3.9: Generated voltage with winding under load.

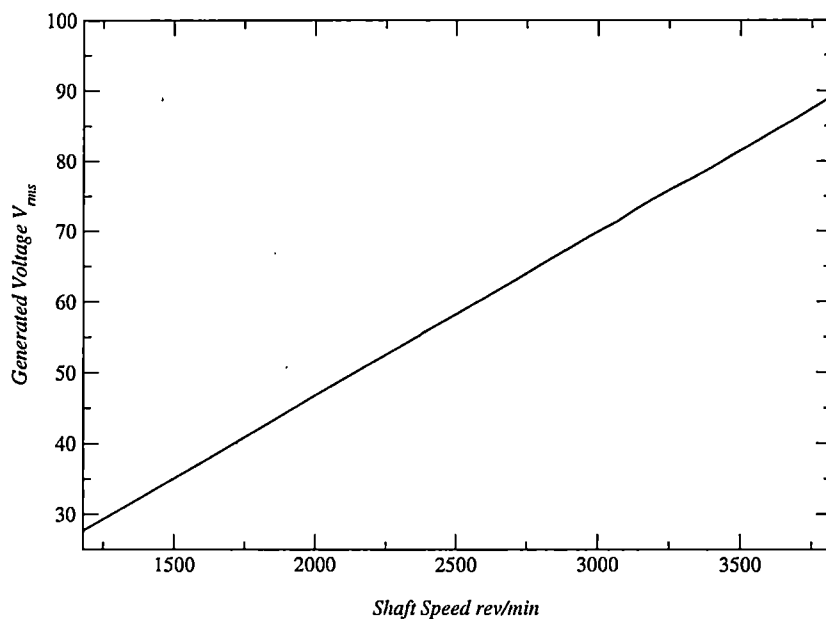


Figure 3.10: Generated voltage vs speed for winding #2.

Winding #2

A second winding was designed and built according to Table 3.2. The open circuit voltage as a function of speed is shown in Figure 3.10 and illustrates the linear relationship between the speed and generated voltage.

Summary

The data presented in this chapter validate the equations developed for the generated voltage. The discrepancies between the theoretical and measured values have been accounted for. The next chapter develops the mathematical basis for the magnetic analysis of electric machines. Although this subject appears in a variety of literature, it has been condensed to equations and concepts of particular interest to machine designers.

Chapter 4

Magnetic Field Analysis

Maxwell's equations describe all electromagnetic phenomena; the equations are general and are expressed in various forms. To use them properly it is necessary to understand which form applies to a particular problem and the assumptions used to model the problem. Electromagnetic problems can range from high frequency applications, the completely coupled \hat{E} and \hat{H} field, to the magnetostatic, uncoupled case where all time dependency is suppressed. Between these two extremes is the low frequency case where a solution is desired only for the \hat{H} or \hat{B} field. This case results in the formulation of the time dependent eddy current problem. Included in the problem formulation must be the nonlinear behavior and directional effects of the material. In addition, the effects due to permanent magnets and moving media must be accounted for.

This chapter provides an explanation of the different forms of Maxwell's equations and their applicability to different problems, such as the magnetostatic, quasi-static and magnetodynamic cases. This will provide the basis for chapter 5 where numerical techniques will be employed to solve the quasi-static magnetic field problem for electric machines by utilizing the control-volume method.

4.1 General Form of Maxwell's Equations

The most general form of Maxwell's equations are given below:

$$\nabla \times \hat{H} = \hat{J} + \frac{\partial \hat{D}}{\partial t} \quad (4.1)$$

$$\nabla \times \hat{E} = -\frac{\partial \hat{B}}{\partial t} \quad (4.2)$$

$$\nabla \cdot \hat{B} = 0 \quad (4.3)$$

$$\nabla \cdot \hat{D} = \rho \quad (4.4)$$

$$\hat{B} = \mu \hat{H} \quad (4.5)$$

$$\hat{D} = \epsilon \hat{E} \quad (4.6)$$

$$\hat{J} = \sigma \hat{E}. \quad (4.7)$$

Where,

\hat{H} is the magnetic field intensity, *amperes/m*, $\frac{A}{m}$

\hat{B} is the magnetic flux density, *tesla*, T

\hat{D} is the electric flux density, *coulomb/m²*, $\frac{C}{m^2}$

\hat{E} is the electric field strength, *volts/m*, $\frac{V}{m}$

\hat{J} is current density, *amperes/m²*, $\frac{A}{m^2}$

ρ is volume density of free electric charge, *coulomb/m³*, $\frac{C}{m^3}$

σ is electrical conductivity, *mhos/m*, $\frac{\Omega}{m}$

Equation 4.3 is the continuity of flux equation, $\mu = \mu_r \mu_0$ is the permeability of the material and in general $\mu(H)$. The permittivity is $\epsilon = \epsilon_r \epsilon_0$ and is also generally $\epsilon(E)$. The relative permeability μ_r and the relative permittivity ϵ_r can also be functions of direction ie. *non-isotropic*.

For the non-isotropic case, μ and ϵ become tensors.

These equations represent a coupled set and must be solved as such. Maxwell's equations in this form are applicable to high frequency problems such as antennas and radar. These types of problems can be solved numerically in a variety of ways including finite-volume time domain (FVTD) and finite-difference time domain (FDTD) methods. The formulation for solving the equations using FVTD and FDTD techniques is outlined in Chapter 5.

4.2 Low Frequency Case

In the case where we are concerned with low frequencies ($< 10^6 \text{ Hz}$) and no large static charges exist within the machine; the displacement current, the term $\frac{\partial \hat{D}}{\partial t}$, can be neglected and equation 4.1 can be reduced to :

$$\nabla \times \hat{H} = \hat{J}. \quad (4.8)$$

4.2.1 Magnetostatic Case

If one only wishes to study the static behavior of the field, the equation governing the magnetostatic case can be derived by using equations 4.8 and 4.2, and if a magnetic vector potential is defined as \hat{A} and is considered to be solenoidal as proven in [20], we can write:

$$\nabla \times \hat{A} = \hat{B}, \quad (4.9)$$

$$\nabla \cdot \hat{A} = 0. \quad (4.10)$$

Equation 4.10 is referred to as the *Coulomb gauge*. Using the constitutive laws we have:

$$\hat{H} = \nu \hat{B}. \quad (4.11)$$

where $\nu = 1/\mu$. Then by substitution of equation 4.11 into equation 4.8, the result is:

$$\nabla \times \nu \hat{B} = \hat{J}. \quad (4.12)$$

By substituting equation 4.9 into equation 4.12, the result is the curl-curl equation,

$$\nabla \times \nabla \times \nu \hat{A} = \hat{J}. \quad (4.13)$$

Using the vector identity,

$$\nabla \times \nabla \times \hat{C} = \nabla (\nabla \cdot \hat{C}) - \nabla^2 \hat{C} \quad (4.14)$$

$$= \nabla (\nabla \cdot \hat{C}) - \nabla \cdot (\nabla \hat{C}) \quad (4.15)$$

and setting $C = \nu \hat{A}$ and substituting into equation 4.13,

$$\nabla (\nabla \cdot \nu \hat{A}) - \nabla^2 \nu \hat{A} = \hat{J} \quad (4.16)$$

$$\nabla (\nabla \cdot \nu \hat{A}) - \nabla \cdot (\nu \nabla \hat{A}) = \hat{J}. \quad (4.17)$$

Applying the *Coulomb gauge* $\nabla \cdot \nu \hat{A} = 0$, equation 4.16 becomes Poisson's equation:

$$\nabla \cdot (\nu \nabla \hat{A}) = -\hat{J}. \quad (4.18)$$

When ν is uniform in space, equation 4.18 becomes,

$$\nabla \cdot (\nabla \hat{A}) = -\mu \hat{J} \quad (4.19)$$

$$\nabla^2 \hat{A} = -\mu \hat{J}. \quad (4.20)$$

Equation 4.18 is relevant in the regions where a source term exists; in machines, this is generally the slot region and the permanent magnet region. In regions without current, equation 4.18 becomes Laplace's equation,

$$\nabla^2 \hat{A} = 0. \quad (4.21)$$

Equations 4.18 and 4.21 describe the magnetic vector potential throughout the entire structure for the magnetostatic case. These two equations coupled with imposing the *coulomb gauge*, can be solved by finite-differences or by finite-elements. The resulting equations are tridiagonal and can be solved very efficiently by a variety of tridiagonal matrix solvers.

Permanent Magnets

Many electromechanical devices contain permanent magnets to supply flux. The use of permanent magnets results in higher power densities. Higher power density is achieved since the applied current does not need to create a sustaining field and can be used entirely to produce a force or torque. In the analysis of the fluxes and flux densities it is necessary to account for the use of permanent magnets. To accomplish this, equation 4.8 is written as,

$$\nabla \times [\nu B - \hat{H}_c] = \hat{J}. \quad (4.22)$$

and can be rearranged as

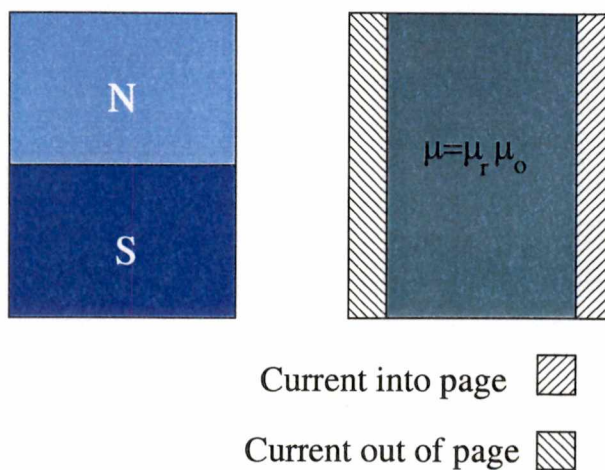


Figure 4.1: Replacement of permanent magnet with equivalent sheet current.

$$\nabla \times \nu B = \widehat{J} + \underbrace{\nabla \times \widehat{H}_c}_{\widehat{J}_m}. \quad (4.23)$$

In equation 4.23, \widehat{J}_m can be considered as an equivalent *ampere-turn* source since,

$$\oint H \bullet dl = NI \quad (4.24)$$

and if a sheet current is considered, 4.24 can be written as,

$$H_c l_m = I.$$

By using the length of the magnet and knowing its material property H_c , the coercivity, an equivalent sheet current can be utilized to model the permanent magnet.

4.2.2 Quasi-Static Case

By utilizing equations 4.8 and 4.2 the equations governing the quasi-static case can be developed. Beginning with equation 4.2 and using the definition of the magnetic vector potential in equation 4.9, one can write:

$$\nabla \times \hat{E} = -\frac{\partial \hat{B}}{\partial t} \quad (4.25)$$

$$= -\frac{\partial}{\partial t} [\nabla \times \hat{A}] \quad (4.26)$$

$$= \nabla \times \frac{\partial \hat{A}}{\partial t}. \quad (4.27)$$

Equation 4.27 can be written as,

$$\nabla \times \left[\hat{E} + \frac{\partial \hat{A}}{\partial t} \right] = 0 \quad (4.28)$$

by utilizing the vector relationship

$$\nabla \times (\nabla \Phi) = 0$$

an electric scalar potential

$$-\nabla \Phi = \hat{E} + \frac{\partial \hat{A}}{\partial t} \quad (4.29)$$

can be defined. By combining equations 4.7 and 4.29 the current density becomes,

$$\hat{J} = \underbrace{-\sigma \nabla \Phi}_{\hat{J}_a} - \sigma \underbrace{\frac{\partial \hat{A}}{\partial t}}_{\hat{J}_i}. \quad (4.30)$$

where the induced and applied components are represented by \hat{J}_i and \hat{J}_a , respectively. An alternate form of equation 4.18 is,

$$\nabla \cdot (\nu \nabla \hat{A}) = -\hat{J}. \quad (4.31)$$

Finally, by substituting equation 4.30 into equation 4.31,

$$\nabla \cdot (\nu \nabla \hat{A}) = \sigma \frac{\partial \hat{A}}{\partial t} + \sigma \nabla \Phi \quad (4.32)$$

or equivalently as,

$$\sigma \frac{\partial \hat{A}}{\partial t} + \nabla \cdot (-\nu \nabla \hat{A}) = \hat{J}_a. \quad (4.33)$$

Equation 4.33 represents *magnetic diffusion* and can be written in a more general form as,

$$\sigma \hat{A}_t + \nabla \cdot \hat{F} = \hat{S}. \quad (4.34)$$

4.2.3 Magnetodynamic Case

To include the effect of material motion, an additional source term is added to the right hand side of equation 4.32 with a polarity in opposition to the applied source. Thus,

$$\nabla \cdot (\nu \nabla \hat{A}) = \sigma \frac{\partial \hat{A}}{\partial t} + \sigma \nabla \Phi - \sigma(v \times B) \quad (4.35)$$

where the term $v \times B$ represents the *speed voltage* and v represents relative velocity. In terms of magnetic vector potential,

$$\nabla \cdot (\nu \nabla \hat{A}) = \sigma \frac{\partial \hat{A}}{\partial t} + \sigma \nabla \Phi - \sigma(v \times \nabla \times A). \quad (4.36)$$

Rearranging, in a form similar to equation 4.33,

$$\sigma \frac{\partial \hat{A}}{\partial t} + \nabla \cdot (-\nu \nabla \hat{A}) = -\hat{J}_a + \sigma(v \times \nabla \times A). \quad (4.37)$$

4.3 Summary of the Applicability of Maxwell's Equations

It is instructive to summarize the applicability of Maxwell's equations to the electric machine problem. Figure 4.2 depicts the use of Maxwell's equations beginning with the most general form pertaining to all electromagnetic phenomena. The right branch of the figure illustrates the use of Maxwell's equations for the completely static case where all time dependency has been removed. The significance of the suppression of time dependency is that the resulting equations are now completely un-coupled and represent the electrostatic and magnetostatic cases independently. Since we are restricting the discussion to the analysis of electric machines, the magnetostatic case is of most interest.

The magnetostatic analysis is used by magnetic designers to estimate the static flux in various parts, including the air gap, of the electric machine. The estimation of the flux in the yoke, teeth and air-gap determine the characteristics of the machine's overall performance. The results of the analysis are used to refine the design of the machine to produce the desired results. The introduction of the magnetic vector potential reduces the set of equations shown in box 2R in Figure 4.2 to Poisson's equation shown in box 3R. Furthermore, in source less regions, Laplace's equation results. Poisson's equation as well as Laplace's equations are used throughout engineering and science to model the behavior of various processes. Therefore, very efficient solvers have been developed to rapidly produce results for equations of this form.

The left branch of Figure 4.2 depicts the path to applying Maxwell's equations to solve the eddy current problem encountered when objects are subject to a changing \hat{B} field with respect to time. Box 1L represents the set of equations that govern the quasi-static case. It is worth noting that the \hat{E} field is still dependent on the \hat{B} field; therefore, the equations are still coupled. By introducing a magnetic vector potential and a scalar electric potential, box 2R shows the resulting curl-curl equation governing the magnetic vector potential is equal to a source term dependent on a time varying \hat{A} and an applied potential. Finally, box 3L illustrates that the equations in box

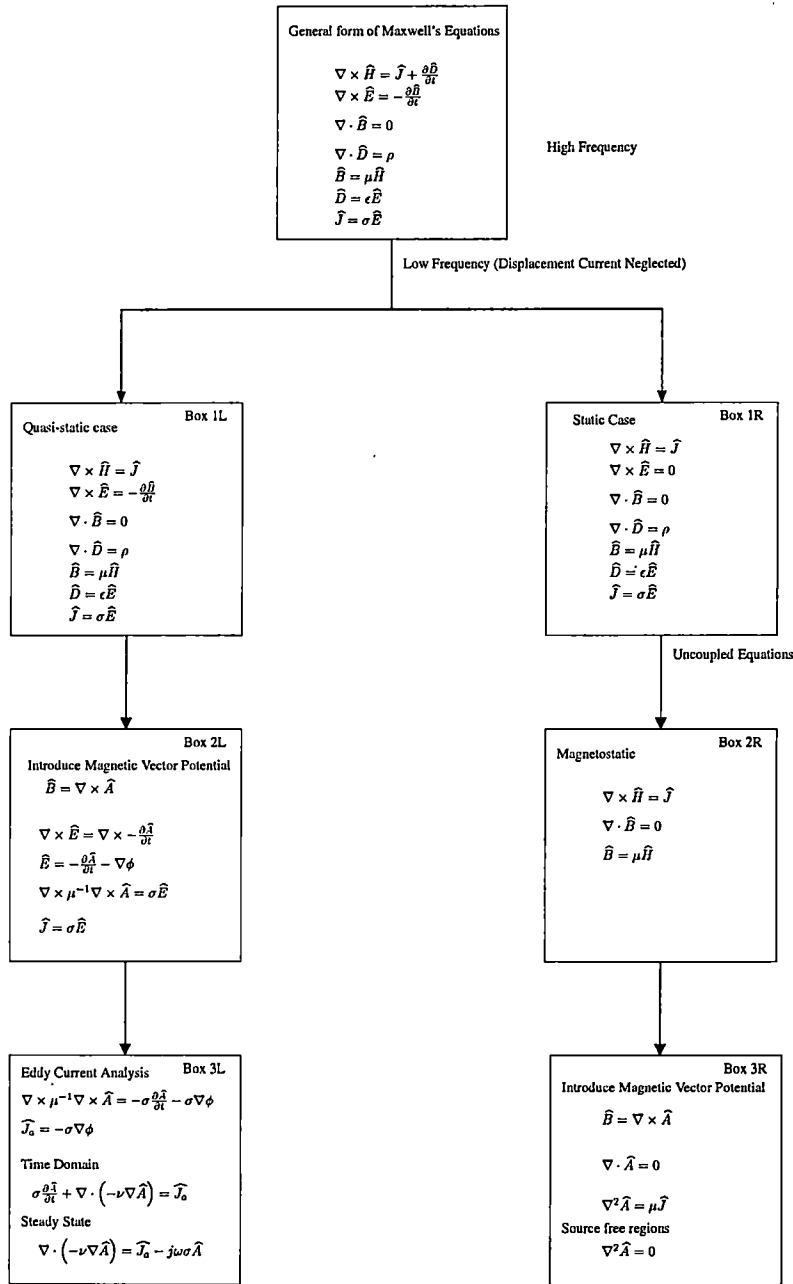


Figure 4.2: Application of Maxwell's equations.

2L can be written in a form representing magnetic diffusion. A further reduction can be achieved if the transient solution to the sinusoidally driven problem is neglected. In this case, a phasor rotating at the applied frequency is used to represent the time-varying magnetic vector potential.

To simplify Figure 4.2, the magnetodynamic case has not been included. The inclusion would simply result in an additional source term applied to the right hand side of the first equation in box 3L. While the magnetodynamic case is important to the machine designer, it is beyond the scope of the present work. The overview presented in this section provides a premise for the next chapter which develops a new approach to the solution of the magnetic diffusion equation governing the transient eddy current problem.

Chapter 5

Finite-Volume and Finite-Difference Methods

The solution of the magnetic field problem remains an important part of the electric machine design verification process, estimating the flux density in various parts of the machine is necessary to avoid saturation. In addition, the ability to predict the losses in machines is extremely important in high performance applications.

Many methods have been devised throughout the years to solve the field problem for the electric machine. Beginning in the 1960's the finite difference approach to solving Maxwell's equations was heavily used [11]. This approach produced reasonable results but was extremely costly computationally; this led researchers to reformulate the problem to efficiently use the limited computer resources of the day. This work led to the finite element method (FEM). In general, the FEM approach subdivides the supplied geometry, solution domain, into a series of smaller triangular mesh elements, sub-domains. The solution of the field problem is performed using variational methods to arrive at a solution to a minimized energy function as opposed to directly solving the equation that governs the physical problem. Once the problem is formulated, a set of

matrix equations are solved. Most of these algorithms were designed to solve the magnetostatic problem and did not address the transient electromagnetic problem or the time harmonic problem.

Research has produced other methods such as the boundary element method (BEM), finite difference time domain (FDTD) and the finite volume time domain (FVTD) method. The BEM emerged during the middle to late 1980's but has not gained much support in the marketplace. The FDTD and FVTD methods have become heavily researched topics during the 1990's as they apply to the electromagnetic scattering problem, primarily due to the intuitive nature of the approach and the low cost of computing. Research advances in computational fluid dynamics (CFD) has prompted researchers to re-examine the use of these methods as they apply to Maxwell's equations.

This chapter presents an overview of the research in applying FVTD and FDTD methods to solving Maxwell's equations. The application of FDTD/FVTD techniques to problems in electrical engineering range from the solution of antenna propagation to scattering problems to field analysis for electric machines. In the electric machine field problem, it is not generally necessary to solve for the total field due to the relatively low frequencies. Additionally, the application of FVTD methods to the solution of the eddy current problem is presented. The application of FVTD methods to solving the magnetic diffusion problem presented in Chapter 4.2.2 is, to the author's knowledge, a new approach.

As with all numerical approximations, it is advantageous to compare the numerical results utilizing a problem with a known analytical solution. This chapter provides the foundation for the numerical algorithm applied to a 1D sample problem presented in Chapter 6.

5.1 Finite Difference Time Domain Method

The FDTD method was first proposed by Yee [26] in 1966 and did not receive widespread attention until the 1980's due to its high computational cost. As the cost of computing dramat-

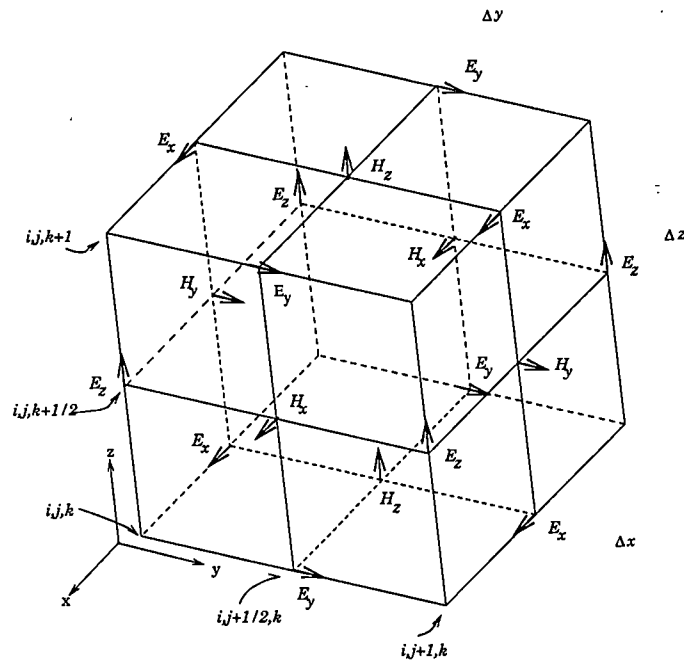


Figure 5.1: Yee cell.

ically fell during the 1990's the FDTD method became viable. The method proposed by Yee was designed around a staggered grid as depicted in Figure 5.1, the updates of \hat{H} and \hat{E} occur at different locations in time and space due to the offset grid. The Yee algorithm was found to have second-order accuracy in both space and time but the algorithm was not fully examined until 1988 when Taflove [21] analyzed the errors and correctly developed the stability criteria. The Yee algorithm was initially developed for Cartesian coordinates but has been extended to other coordinate systems by Holland [14].

One of the disadvantages of using a staggered grid, is that it does not provide the field values at the same point in time and space. The need to store field values at different grid points and time steps requires a more complicated data structure. Later works reformulated Yee's algorithm to be applied to a collocated grid where the field quantities are stored at the same grid point. Additionally, the inability of the uniform-grid to properly model certain waveguide problems led to work by White *et al.* [17] to develop a multigrid method which modifies the uniform-grid to

include a refined mesh in regions of interest.

The FDTD algorithm proposed by Yee is based on the discretization of

$$\nabla \times \hat{H} = \hat{J} + \frac{\partial \hat{D}}{\partial t} \quad (5.1)$$

$$\nabla \times \hat{E} = -\frac{\partial \hat{B}}{\partial t} \quad (5.2)$$

by replacing the space and time derivatives at a lattice point i, j, k in cartesian coordinates with forward differences

$$\frac{\partial f^n(i, j, k)}{\partial x} = \frac{f^n(i+\frac{1}{2}, j, k) - f^n(i-\frac{1}{2}, j, k)}{\Delta x} \quad (5.3)$$

$$\frac{\partial f^n(i, j, k)}{\partial t} = \frac{f^{n+\frac{1}{2}}(i, j, k) - f^{n-\frac{1}{2}}(i, j, k)}{\Delta t} \quad (5.4)$$

Here, equation 5.3 would be modified to represent derivatives in the y and z directions. By applying these approximated derivatives to equations 5.1 and 5.2, the resulting set of finite difference equations utilizing a uniform mesh $\Delta = \Delta x = \Delta y = \Delta z$ are

$$\begin{aligned}
 H_x^{n+\frac{1}{2}}(i, j + \frac{1}{2}, k + \frac{1}{2}) &= H_x^{n+\frac{1}{2}}(i, j + \frac{1}{2}, k + \frac{1}{2}) + \frac{\Delta t}{\mu(i, j + \frac{1}{2}, k + \frac{1}{2})\Delta} \\
 &\quad \left[E_y^n(i, j + \frac{1}{2}, k + 1) - E_y^n(i, j + \frac{1}{2}, k + \frac{1}{2}) \right. \\
 &\quad \left. + E_z^n(i, j, k + \frac{1}{2}) - E_z^n(i, j + 1, k + \frac{1}{2}) \right]
 \end{aligned} \tag{5.5}$$

$$\begin{aligned}
 H_y^{n+\frac{1}{2}}(i + \frac{1}{2}, j, k + \frac{1}{2}) &= H_y^{n+\frac{1}{2}}(i + \frac{1}{2}, j, k + \frac{1}{2}) + \frac{\Delta t}{\mu(i + \frac{1}{2}, j, k + \frac{1}{2})\Delta} \\
 &\quad \left[E_z^n(i + 1, j, k + \frac{1}{2}) - E_z^n(i, j, k + \frac{1}{2}) \right. \\
 &\quad \left. + E_x^n(i + \frac{1}{2}, j, k) - E_x^n(i + \frac{1}{2}, j, k + 1) \right]
 \end{aligned} \tag{5.6}$$

$$\begin{aligned}
 H_z^{n+\frac{1}{2}}(i + \frac{1}{2}, j + \frac{1}{2}, k) &= H_z^{n+\frac{1}{2}}(i + \frac{1}{2}, j + \frac{1}{2}, k) + \frac{\Delta t}{\mu(i + \frac{1}{2}, j + \frac{1}{2}, k)\Delta} \\
 &\quad \left[E_x^n(i + \frac{1}{2}, j + 1, k) - E_x^n(i + \frac{1}{2}, j, k) \right. \\
 &\quad \left. + E_y^n(i, j + \frac{1}{2}, k) - E_y^n(i + 1, j + \frac{1}{2}, k) \right]
 \end{aligned} \tag{5.7}$$

$$\begin{aligned}
 E_x^{n+1}(i + \frac{1}{2}, j, k) &= \left[1 - \frac{\sigma(i + \frac{1}{2}, j, k)\Delta t}{\epsilon(i + \frac{1}{2}, j, k)} \right] E_x^n(i + \frac{1}{2}, j, k) \\
 &+ \frac{\Delta t}{\epsilon(i + \frac{1}{2}, j, k)\Delta} \left[H_z^{n+\frac{1}{2}}(i + \frac{1}{2}, j + \frac{1}{2}, k) - H_z^{n+\frac{1}{2}}(i + \frac{1}{2}, j - \frac{1}{2}, k) \right. \\
 &\quad \left. + H_y^{n+\frac{1}{2}}(i + \frac{1}{2}, j, k - \frac{1}{2}) - H_y^{n+\frac{1}{2}}(i + \frac{1}{2}, j, k + \frac{1}{2}) \right]
 \end{aligned} \tag{5.8}$$

$$\begin{aligned}
 E_y^{n+1}(i, j + \frac{1}{2}, k) &= \left[1 - \frac{\sigma(i, j + \frac{1}{2}, k)\Delta t}{\epsilon(i, j + \frac{1}{2}, k)} \right] E_y^n(i, j + \frac{1}{2}, k) \\
 + \frac{\Delta t}{\epsilon(i, j + \frac{1}{2}, k)\Delta} &\left[H_x^{n+1}(i, j + \frac{1}{2}, k + \frac{1}{2}) - H_x^{n+1}(i, j + \frac{1}{2}, k - \frac{1}{2}) \right. \\
 &\left. + H_z^{n+1}(i - \frac{1}{2}, j + \frac{1}{2}, k) - H_z^{n+1}(i + \frac{1}{2}, j + \frac{1}{2}, k) \right]
 \end{aligned} \tag{5.9}$$

$$\begin{aligned}
 E_z^{n+1}(i, j, k + \frac{1}{2}) &= \left[1 - \frac{\sigma(i, j, k + \frac{1}{2})\Delta t}{\epsilon(i, j, k + \frac{1}{2})} \right] E_z^{n+\frac{1}{2}}(i, j, k + \frac{1}{2}) \\
 + \frac{\Delta t}{\epsilon(i, j, k + \frac{1}{2})\Delta} &\left[H_y^{n+1}(i + \frac{1}{2}, j, k + \frac{1}{2}) - H_y^{n+1}(i - \frac{1}{2}, j, k + \frac{1}{2}) \right. \\
 &\left. + H_x^{n+1}(i, j - \frac{1}{2}, k + \frac{1}{2}) - H_x^{n+1}(i, j + \frac{1}{2}, k + \frac{1}{2}) \right].
 \end{aligned} \tag{5.10}$$

Here, the superscripts denote time and the subscripts denote field component at grid points i, j, k .

The Yee algorithm uses the staggered leapfrog method to solve the set of hyperbolic partial differential equations; the updated values for \hat{H} and \hat{E} are functions of the past values and the other field vectors at appropriate points. Taflové [22] found the correct stability criteria to be

$$v_{max}\Delta t \leq \frac{1}{\sqrt{\left(\frac{1}{\Delta x^2} + \frac{1}{\Delta y^2} + \frac{1}{\Delta z^2}\right)}}. \tag{5.11}$$

The value of v_{max} is the maximum phase velocity expected.

A tremendous amount of literature has been published during the 1990's in regards to the application of FDTD techniques to various problems in electrical engineering. Much of the research focuses on alternate gridding schemes, material modeling and applications; an excellent survey paper by Shlager and Schneider [19] presents an overview and references for most of the

important advances in FDTD algorithms and applications. The next section explores the use of the advances in computational fluid dynamics (CFD) applied to electrical engineering problems.

5.2 Finite Volume Time Domain Method

Finite volume (FV) techniques were first used by researchers to solve CFD problems; the technique is based on conservation of energy principles. Fundamentally, this can be viewed as *amount gained = amount into, through boundaries + amount generated inside* a particular control volume. The application of FV methods to electrical engineering are based on formulating Maxwell's equations in conservation form. In order to place Maxwell's equations in this form, it is necessary to provide a mathematical basis for FV methods, which is presented below.

Mathematically, the fundamental conservation principle can be represented in differential form as

$$\frac{\partial Q}{\partial t} + \nabla \cdot \vec{F} = S \quad (5.12)$$

where Q represents the amount in the control volume, F the flux of Q over an area per unit time and S the source of Q per volume per time. One might note that equation 5.12 is quite general and can be used for processes that can be modeled by conservation principles. By developing the flux term to describe a particular process (diffusion, advection, etc.) one can study various processes by simply altering the form of the flux term.

Equation 5.12 can be placed in integral form by integrating it over the control volume V , shown in Figure 5.2,

$$\frac{d}{dt} \int_{\Omega} Q \, dx dy dz + \int_{\Omega} \nabla \cdot \vec{F} \, dx dy dz = \int_{\Omega} S \, dx dy dz \quad (5.13)$$

and by applying Gauss's Divergence theorem, the second term of equation 5.13 can be written as

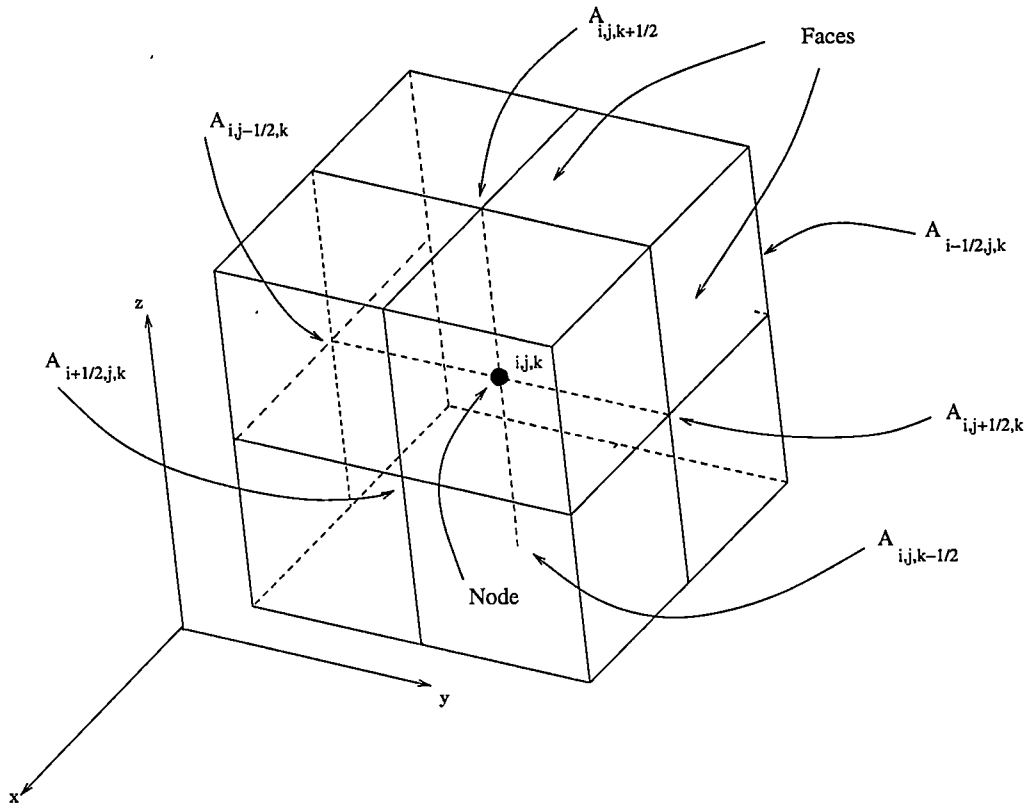


Figure 5.2: Control volume in cartesian coordinates.

a surface integral; therefore, equation 5.13 becomes,

$$\frac{d}{dt} \int_{\Omega} Q \, dx \, dy \, dz + \int_{\partial\Omega} \vec{F} \cdot \vec{n} \, da = \int_{\Omega} S \, dx \, dy \, dz, \quad (5.14)$$

where $\vec{n} = n_x \vec{a}_x + n_y \vec{a}_y + n_z \vec{a}_z$ represents a unit vector directed outwardly from each of the six faces. It is interesting to note that the integral form of the conservation law represents an average of Q over the cell; thus, rapid changes at material interfaces do not adversely affect the solution.

Conservation-Law Form of Maxwell's Equations

The FV discretization of Maxwell's equations was derived by Mohammadian *et al.* [1] to solve the scattering problem. Maxwell's equations were formulated into a set of conservation

equations and solved numerically. The formulation was based on a modified form of equation 5.12 and is

$$\frac{\partial Q}{\partial t} + \nabla \cdot F = S, \quad (5.15)$$

where Q is a vector with components,

$$Q^T = \{B_x, B_y, B_z, D_x, D_y, D_z\}$$

and F has components $\{\vec{F}_x, \vec{F}_y, \vec{F}_z\}$

$$\begin{aligned} \vec{F}_x &= \left\{ 0 \frac{-D_z}{\epsilon} \frac{D_y}{\epsilon} 0 \frac{B_z}{\mu} \frac{-B_y}{\mu} \right\} \\ \vec{F}_y &= \left\{ 0 \frac{-D_z}{\epsilon} \frac{D_y}{\epsilon} 0 \frac{B_z}{\mu} \frac{-B_y}{\mu} \right\} \\ \vec{F}_z &= \left\{ \frac{D_z}{\epsilon} 0 \frac{-D_x}{\epsilon} \frac{-B_z}{\mu} 0 \frac{B_x}{\mu} \right\}. \end{aligned}$$

5.3 Application of Finite Volume Technique to Eddy Current Problem

The previous section discusses the solution of the total field problem utilizing FD and FV techniques. In many low frequency applications, it is not necessary to solve the complete field problem. One such case is the solution of the eddy current problem in electric machines. Eddy currents arise in electric machines due to a changing \hat{B} field inducing currents in the material supporting the flux that produces torque. The study of eddy currents is quite important in determining loss in the magnetic material which, coupled with hysteresis, windage and I^2R loss, determines the overall efficiency of the machine.

There has been a tremendous amount of research in accurately solving the eddy current problem. Most authors [9, 23] formulate the problem using steady state sinusoidal analysis and finite element analysis to produce a solution. The error in applying sinusoidal steady state analysis to the eddy current problem is the application of linear system analysis to an inherently non-linear problem. Most electric machines utilize magnetic material that possesses a non-linear permeability μ_r . By utilizing a time-stepping approach the effects of the non-linear nature of μ_r can be accounted for. Additionally, the time-stepping approach allows the investigator the ability to study the effects of a time-dependent source. The formulation of solving the time-dependent eddy current problem utilizing a numerical finite volume method is developed below.

5.3.1 Numerical Formulation

The development of the numerical technique begins with the equations that describe the physical phenomenon to be modeled. The equations used to model *magnetic diffusion* in cartesian coordinates from Chapter 4 are,

$$\begin{aligned}\sigma \frac{\partial A_x}{\partial t} + \nabla \cdot \vec{F}_x &= J_x \\ \sigma \frac{\partial A_y}{\partial t} + \nabla \cdot \vec{F}_y &= J_y \\ \sigma \frac{\partial A_z}{\partial t} + \nabla \cdot \vec{F}_z &= J_z,\end{aligned}\tag{5.16}$$

where $\vec{F}_i = -v \nabla A_i$ represents the flux. with $v = \mu^{-1}$.

By considering only one component, for simplicity, of the magnetic vector potential \hat{A} and using the integral form of the conservation law given as equation 5.14, a numerical scheme can be developed. Integrating the first term of equation 5.14 over the control volume V_{ijk} and in time $[t_n, t_{n+1}]$

$$\int_{t_n}^{t_n+\Delta t_n} \frac{d}{dt} \int_{V_{ijk}} \sigma A(x, y, z, t) dx dy dz dt \quad (5.17)$$

we can then write

$$\sigma_{i,j,k} A_{i,j,k}^n = \frac{1}{\Delta V_{ijk}} \underbrace{\left[\int \int \int \sigma A(x, y, z, t) dx dy dz \right]}_{\text{mean value of } A \text{ over control volume}},$$

where i, j, k represents values at the grid nodes and the superscript represents time and $\Delta V_{ijk} = (x_{i+1} - x_i)(y_{j+1} - y_j)(z_{k+1} - z_k)$; when a uniform mesh is utilized $\Delta V_{ijk} = \Delta x \Delta y \Delta z$. Numerically, the first term of equation 5.14 becomes

$$\Delta V_{ijk} \left[\sigma_{i,j,k} A_{i,j,k}^{N+1} - \sigma_{i,j,k} A_{i,j,k}^N \right]. \quad (5.18)$$

The discretization for the second term of equation 5.14 follows in similar fashion. The mean flux through the rear face in Figure 5.2 during the time interval $[t_n, t_n + \Delta t_n]$ is

$$F_{i-\frac{1}{2},j,k}^{n+\theta} = \frac{1}{\Delta t_n} \int_{t_n}^{t_n+\Delta t_n} \frac{1}{a_{i-\frac{1}{2},j,k}} \int_{a_{i-\frac{1}{2},j,k}} \vec{F} \cdot \vec{n} da dt. \quad (5.19)$$

The net fluxes in the x, y, z directions can be represented numerically as

$$\begin{aligned} \Delta t_n \left[(Fa)_{i+\frac{1}{2},j,k}^{n+\theta} - (Fa)_{i-\frac{1}{2},j,k}^{n+\theta} \right] & \quad x \text{ directed} \\ \Delta t_n \left[(Fa)_{i,j+\frac{1}{2},k}^{n+\theta} - (Fa)_{i,j-\frac{1}{2},k}^{n+\theta} \right] & \quad y \text{ directed} \\ \Delta t_n \left[(Fa)_{i,j,k+\frac{1}{2}}^{n+\theta} - (Fa)_{i,j,k-\frac{1}{2}}^{n+\theta} \right] & \quad z \text{ directed.} \end{aligned}$$

Finally, the source term can be represented numerically by following the steps performed for equation 5.18, thus

$$S_{i,j,k}^{n+\theta} = \frac{1}{\Delta t_n} \int_{t_n}^{t_n+\Delta t_n} \frac{1}{\Delta V_{ijk}} \int_{\Omega_i} S(x, y, z, t) dx dy dz dt, \quad (5.20)$$

where the mean value of S over the control volume is,

$$\frac{1}{\Delta V_{ijk}} \int_{\Omega_i} S(x, y, z, t) dx dy dz. \quad (5.21)$$

Thus, numerically the source term is represented as,

$$\Delta t_n \Delta V_{i,j,k} S_{i,j,k}^{n+\theta}. \quad (5.22)$$

The discretized PDE based on the conservation law becomes

$$\begin{aligned} \Delta V_{ijk} \left[\sigma_{i,j,k} A_{i,j,k}^{n+1} - \sigma_{i,j,k} A_{i,j,k}^n \right] = & \Delta t_n \left[(Fa)_{i+\frac{1}{2},j,k}^{n+\theta} - (Fa)_{i-\frac{1}{2},j,k}^{n+\theta} \right] \\ & + \Delta t_n \left[(Fa)_{i,j+\frac{1}{2},k}^{n+\theta} - (Fa)_{i,j-\frac{1}{2},k}^{n+\theta} \right] \\ & + \Delta t_n \left[(Fa)_{i,j,k+\frac{1}{2}}^{n+\theta} - (Fa)_{i,j,k-\frac{1}{2}}^{n+\theta} \right] \\ & + \Delta t_n \Delta V_{i,j,k} S_{i,j,k}^{n+\theta}. \end{aligned} \quad (5.23)$$

The flux terms in equation 5.23 contain an ambiguity in time represented by θ . The value of θ determines the type of solution method and assumes values $0 < \theta \leq 1$; when $\theta = 0$ the scheme is explicit and implicit when $\theta = 1$. When $\theta = .5$ the scheme is of the Crank-Nicholson type and is unconditionally stable as proven in [15]. The use of values of $\theta \neq 0$ would require the use of a tridiagonal solver to solve the resulting set of simultaneous equations at each time step; by setting θ to zero an explicit scheme results. By re-arranging equation 5.23 and setting $\theta = 0$ the resulting

equation based solely on past values of A and fluxes is

$$\begin{aligned}
 A_{i,j,k}^{n+1} = A_{i,j,k}^n &+ \frac{\Delta t_n}{\sigma_{i,j,k} \Delta V_{ijk}} \left[(Fa)_{i+\frac{1}{2},j,k}^{n+\theta} - (Fa)_{i-\frac{1}{2},j,k}^{n+\theta} \right] \\
 &+ \frac{\Delta t_n}{\sigma_{i,j,k} \Delta V_{ijk}} \left[(Fa)_{i,j+\frac{1}{2},k}^{n+\theta} - (Fa)_{i,j-\frac{1}{2},k}^n \right] \\
 &+ \frac{\Delta t_n}{\sigma_{i,j,k} \Delta V_{ijk}} \left[(Fa)_{i,j,k+\frac{1}{2}}^n - (Fa)_{i,j,k-\frac{1}{2}}^n \right] \\
 &+ \frac{\Delta t_n}{\sigma_{i,j,k}} S_{i,j,k}^n.
 \end{aligned} \tag{5.24}$$

Determination of Fluxes

It is worth noting that equation 5.24 is quite general. A could represent magnetic vector potential, temperature or fluid flow. The flux terms determine the overall form of equation 5.24. In this particular application the process to be modeled is diffusion and the flux is represented by

$$\vec{F} = -v \nabla A. \tag{5.25}$$

Therefore, it is necessary to develop a numerical expression to model equation 5.25. Considering a nonlinear v , the flux times area at time t_n for the rear face can be derived as

$$(Fa)_{i-\frac{1}{2},j,k}^n = \frac{-\Delta A a}{\frac{(x_{i+1}-x_i)}{v_{i-\frac{1}{2},j,k}}} = -\frac{(A_{i,j,k}^n - A_{i-1,j,k}^n)}{\mathcal{R}_{i-\frac{1}{2},j,k}}. \tag{5.26}$$

Since it would be advantageous to specify the value of v at nodes instead of faces, $\mathcal{R}_{i-\frac{1}{2},j,k}$ is written as

$$\mathcal{R}_{i-\frac{1}{2},j,k} = \frac{1}{a_{i-\frac{1}{2},j,k}} \left(\frac{x_{i+1} - x_i}{2v_{i-1}} + \frac{x_{i+1} - x_i}{2v_i} \right). \tag{5.27}$$

Similarly, the flux term for the left face can be written as

$$(Fa)_{i,j-\frac{1}{2},k}^N = \frac{(A_{i,j,k}^n - A_{i,j-1,k}^n)}{\mathcal{R}_{i,j-\frac{1}{2},k}}, \quad (5.28)$$

where,

$$\mathcal{R}_{i,j-\frac{1}{2},k} = \frac{1}{a_{i,j-\frac{1}{2},k}} \left(\frac{y_{j+1} - y_j}{2v_{j-1}} + \frac{x_{j+1} - x_j}{2v_j} \right) \quad (5.29)$$

and the flux term for the bottom face as

$$(Fa)_{i,j,k-\frac{1}{2}}^N = \frac{(A_{i,j,k}^n - A_{i,j,k-1}^n)}{\mathcal{R}_{i,j,k-\frac{1}{2}}}; \quad (5.30)$$

where,

$$\mathcal{R}_{i,j,k-\frac{1}{2}} = \frac{1}{a_{i,j,k-\frac{1}{2}}} \left(\frac{z_{k+1} - z_k}{2v_{k-1}} + \frac{z_{k+1} - z_k}{2v_k} \right). \quad (5.31)$$

The terms representing the fluxes for the front, right and top faces can be found by replacing the indexes in equations 5.26, 5.27, 5.28, 5.29 and 5.30, 5.31 with $i = i + 1$, $j = j + 1$ and $k = k + 1$; respectively. Considerable reduction occurs in the \mathcal{R} terms for a uniform grid.

2D Formulation

In the case of a two-dimensional problem where the source is directed along the z axis, the resultant magnetic vector potential contains only one component A_z . The problem can be formulated by considering the control volume given in Figure 5.3.

It can be seen from Figure 5.3 that the ΔV can be found by setting $\Delta z = 1$ as,

$$\Delta V_{ij} = \left(x_{i+\frac{1}{2}} - x_{i-\frac{1}{2}} \right) \left(y_{j+\frac{1}{2}} - y_{j-\frac{1}{2}} \right). \quad (5.32)$$

Similarly, the areas for the faces can be found as

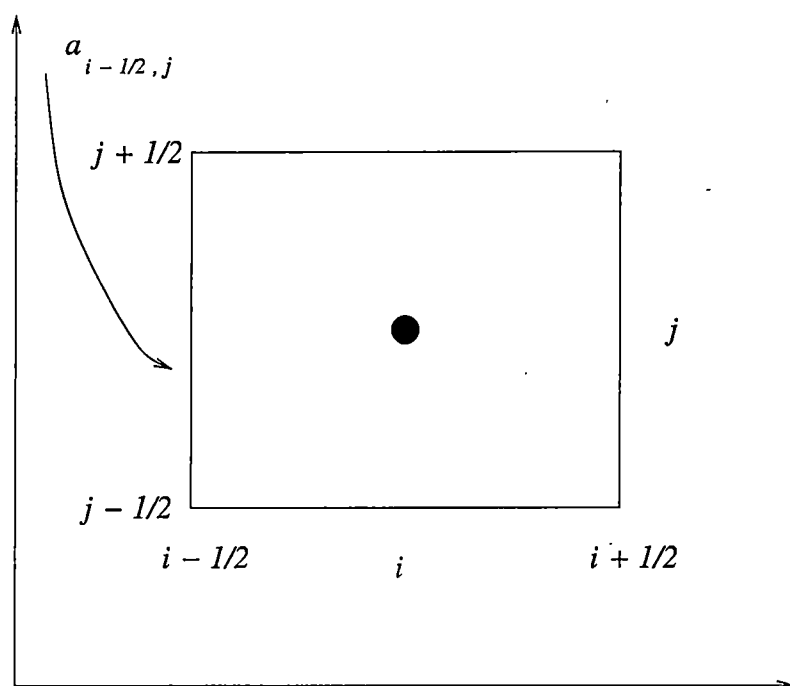


Figure 5.3: Control volume in 2D.

$$\begin{aligned}
 a_{i-\frac{1}{2},j} &= (y_{j+\frac{1}{2}} - y_{j-\frac{1}{2}}) = \Delta y_j \\
 a_{i+\frac{1}{2},j} &= (y_{j+\frac{1}{2}} - y_{j-\frac{1}{2}}) \\
 a_{i,j-\frac{1}{2}} &= (x_{i+\frac{1}{2}} - x_{i-\frac{1}{2}}) = \Delta x_i \\
 a_{i,j+\frac{1}{2}} &= (x_{i+\frac{1}{2}} - x_{i-\frac{1}{2}}).
 \end{aligned} \tag{5.33}$$

The discretized PDE in 2D is written as,

$$\begin{aligned}
 A_{i,j}^{n+1} = A_{i,j}^n &+ \frac{\Delta t_n}{\sigma_{i,j} \Delta x_i \Delta y_j} \left[\frac{(A_{i+1,j}^n - A_{i,j}^n)}{\mathcal{G}_{i+\frac{1}{2},j}} - \frac{(A_{i,j}^n - A_{i-1,j}^n)}{\mathcal{G}_{i-\frac{1}{2},j}} \right] \\
 &+ \frac{\Delta t_n}{\sigma_{i,j} \Delta x_i \Delta y_j} \left[\frac{(A_{i,j+1}^n - A_{i,j}^n)}{\mathcal{G}_{i,j+\frac{1}{2}}} - \frac{(A_{i,j}^n - A_{i,j-1}^n)}{\mathcal{G}_{i,j-\frac{1}{2}}} \right] \\
 &+ \frac{\Delta t_n}{\sigma_{i,j}} S_{i,j}^n.
 \end{aligned} \tag{5.34}$$

3D Formulation

The discretization of the conservation law approach to numerically solve the magnetic diffusion problem has been presented for the 1D and 2D cases. The 3D case would require discretizing three equations similar to equation 5.34 at each node to represent the magnetic vector potentials in the x , y and z directions. Equation 5.34 would be modified to include flux terms for the top and bottom faces of the control volume depicted in Figure 5.2. Additionally, the gauge condition $\nabla \cdot \hat{A} = 0$ would need to be satisfied at each time step to ensure a unique solution.

Chapter 6

Application of Numerical Methods to Sample Problem

In the previous chapter, a numerical algorithm was developed to solve the magnetic diffusion problem. The algorithm was formulated for the general case using the magnetic vector potential. The algorithm can be applied to any type of phenomena that can be modeled by conservation laws. This chapter utilizes the algorithm to solve a specific problem, the 1D magnetic diffusion of the B field in a slab of material. Therefore, the algorithm will be applied to a sample problem to directly solve for the magnetic flux density B . As with any simulation, the accuracy of the solution is the main interest; therefore, a test problem with a known solution is presented and solved using numerical techniques. A brief discussion of the FORTRAN program used to simulate the problem is presented as are the numerical results comparing the simulation to the analytical solution.

6.1 Diffusion in a Conducting Slab

To test the validity of the explicit algorithm developed in Chapter 5, a simple one dimensional problem proposed by Woodson [25] was chosen. The problem consists of a current source driving

a winding of N turns wrapped around a non-conducting $\sigma = 0$ C-core with infinite permeability $\mu = \infty$ as shown in Figure 6.1. A slab of thickness d , height w and length l with conductivity σ and permeability μ is placed in the air gap with the assumption that the height and length are much greater than the thickness of the slab. By making this assumption coupled with the assumption that there is no fringing at the air gap, the slab can be considered to be infinitely long in the y and z directions. Thus, the one dimensional partial differential equation governing the B field in the slab is

$$\frac{1}{\mu\sigma} \frac{\partial^2 B_x}{\partial z^2} = \frac{\partial B_x}{\partial t}. \quad (6.1)$$

It is instructive to note that equation 6.1 is a reduced version of equation 4.33. In this case, the applied current density $\widehat{J}_a = 0$ and the magnetic vector potential \widehat{A} has been replaced by flux density \widehat{B} . Furthermore, equation 4.33 is reduced to one dimension.

For $t < 0$ the switch is considered to be closed; at $t = 0$ the switch is opened and current flows in the winding. Due to the infinite permeability and zero conductivity of the C-core, the \widehat{B} field instantaneously migrates through the core to the air gap where the slab resides. The value of B_x on the top and bottom of the slab at the instant the switch is opened represent the boundary values for the solution of equation 6.1. The value of B_x at this time instant may be found from Ampere's law

$$Hl = NI. \quad (6.2)$$

By substituting $B = \mu H$ and noting that the magnetic path length $l = w$; equation 6.2 may be written as

$$B_o = \frac{\mu_o NI}{w}. \quad (6.3)$$

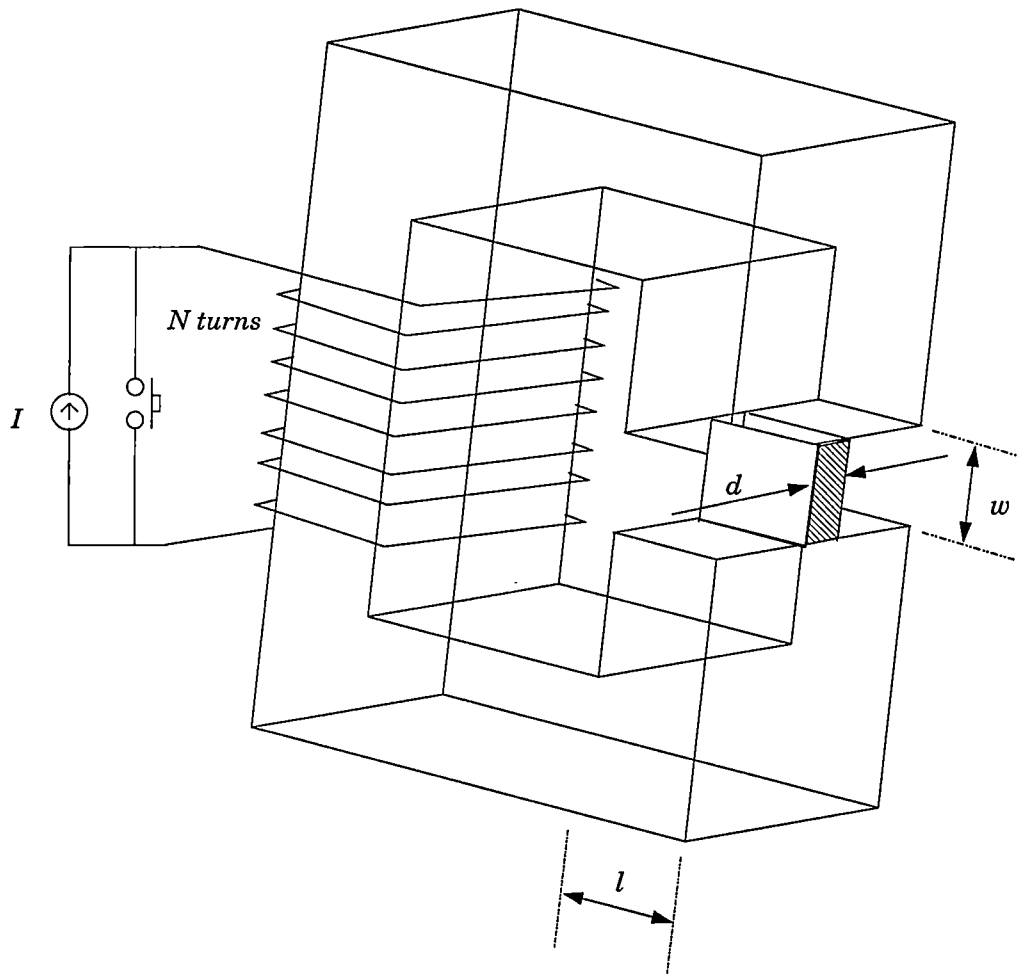


Figure 6.1: Transient diffusion test problem.

The separable solution to equation 6.1 is of the form

$$B_x = \bar{B}(z)e^{-\alpha t} + B_o, \quad (6.4)$$

by substituting equation 6.4 into equation 6.1, the partial differential equation becomes an ordinary differential equation of the form

$$\frac{1}{\mu\sigma} \frac{d^2 \bar{B}}{dz^2} = \frac{\partial \bar{B}}{\partial t}, \quad (6.5)$$

with a general solution

$$B_x(z, t) = (C_1 \sin \sqrt{\mu\sigma\alpha}z + C_2 \cos \sqrt{\mu\sigma\alpha}z) e^{-\alpha t} + B_o. \quad (6.6)$$

By applying the boundary conditions, a series solution can be found to be

$$B_x(z, t) = B_o \left(1 - \sum_{n \text{ odd}} \frac{4}{n\pi} \sin \frac{n\pi z}{d} e^{-n^2 t/\tau} \right), \quad (6.7)$$

where the diffusion time constant is

$$\tau = \frac{\mu\sigma d^2}{\pi^2}. \quad (6.8)$$

Equation 6.7 provides a basis for comparison of the validity of the numerical algorithm. The next section discusses the FORTRAN implementation of the algorithm developed in Chapter 5 applied to equation 6.1.

6.2 Numerical Implementation

A FORTRAN program was developed to numerically calculate the diffusion of the \hat{B} field in the slab of copper. The program implements the numerical algorithm as well as calculates the

analytical value of B_x at each time step and grid point. Additionally, the program calculates the error between the two. A brief discussion of the FORTRAN code appearing in Appendix F is given below.

Magdiffusion

The program *magdiffusion.f* requires 6 input parameters: number of mesh points, maximum time of simulation, print step, conductance, permeability and stability factor. The number of mesh points determines how finely the solution domain is divided, the maximum time of the simulation is the simulation time t that the simulation will run and the print step is the time increment at which data will be written to the output file. The conductance and permeability are the material properties. The stability factor is used to determine the step size used during the simulation. The step size is a critical factor in determining the stability of the algorithm.

Stability

The stability of the numerical routine is determined by utilizing the correct step size during the simulation. The proper step size can be determined by the Courant-Friedrich-Levy (CFL) condition which is derived by applying a positive coefficient rule to the right hand side of equation 5.24. For the 1D variation of equation 5.24, the CFL condition can be found to be

$$\Delta t_{explicit} = \frac{\sigma\mu\Delta z^2}{2}. \quad (6.9)$$

Equation 6.9 represents the maximum time step to ensure a stable solution, the introduction of the stability factor $stab \leq 1$ provides the program with a smaller time step to ensure stability. The time step is defined as

$$\Delta t = stab \cdot \Delta t_{explicit} \quad (6.10)$$

Table 6.1: Sample data for simulation.

Parameter	Program Variable	Value
Mesh points	m	100
Maximum time	$tmax$	8 s
Stability factor	$stab$	0.7
Print step	$dtout$	1 s
Conductivity	ρ	5.9×10^7
Permeability	μ	$4\pi \times 10^{-7}$

Main Program

The main program is responsible for gathering the input data from the user, calculating the time step, executing subroutines and incrementing the time step. The first subroutine called is named *mesh*, the *mesh* routine creates the nodes and faces of the control-volume. The second call is to the subroutine *flux* which calculates flux through the faces at time $t + \Delta t$. The fluxes are used to update the values of B_x at the nodes for the particular time step Δt . Once this is accomplished, the exact solution is calculated for equation 6.7 at Δt and the process is repeated for the next time step. The subroutines *output* and *error* are called when t is equal to the print step supplied by the user. The subroutine *output* stores the values of B_x for the simulation as well as for the exact solution. The subroutine *error* calculates the error between the exact solution and the numerical approximation.

6.3 Test Problem

Several test problems were run to test the program *magdiffusion.f*. Figure 6.2 shows the results of a simulation for a slab of copper with a thickness $d = 1$ m with the simulation parameters given in Table 6.1. The simulation results are presented for the normalized case where $B_x(z, t)$ is normalized by the boundary condition B_o .

6.3.1 Discussion of Numerical Results

Figure 6.2 shows the results of the numerical simulation of the copper slab placed in the air gap of the C-core in Figure 6.1. The simulation was performed over 8 seconds with values presented at 1 second intervals. Clearly, at $t = 0$ s there is no B_x in the center of the slab. Even at $t = 1$ s there is little flux at the center of the slab; thereby, agreeing with the boundary conditions. At $t = 8$ s, the flux density in the middle of the slab is approximately 60% of the flux density at the boundary when $t = 0$ s. Figure 6.3 is a composite graph of the numerical solution and the exact analytical solution. It should be noted that the solution is more accurate at the top of the slab than the bottom. As the simulation progresses, the discretization errors become cumulative; this error may be reduced by increasing the number of nodes at the expense of longer simulation times. The absolute error is shown in Figure 6.4, and shows that the maximum absolute error is approximately 0.025.

6.4 Summary

This chapter validated the effectiveness and accuracy of the algorithm developed in Chapter 5. Although the problem presented here was of one dimension, the extrapolation to multi-dimensions should produce the same results as long as the caveats presented in Chapter 5.3.1 are observed.

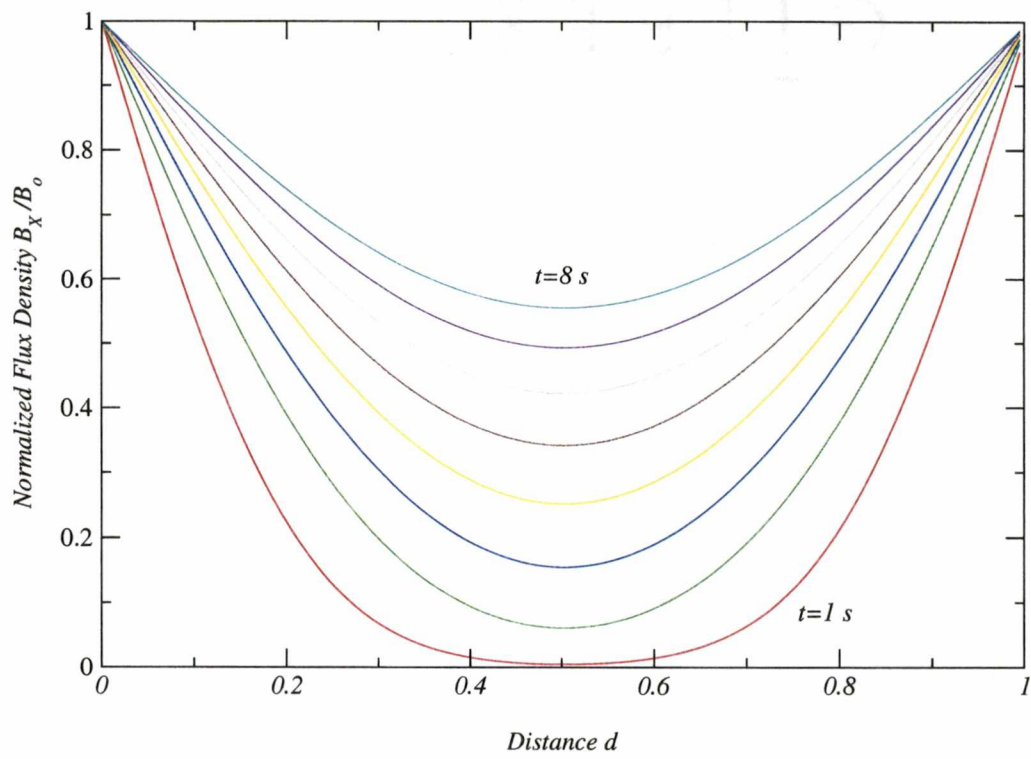


Figure 6.2: Magnetic diffusion into copper slab.

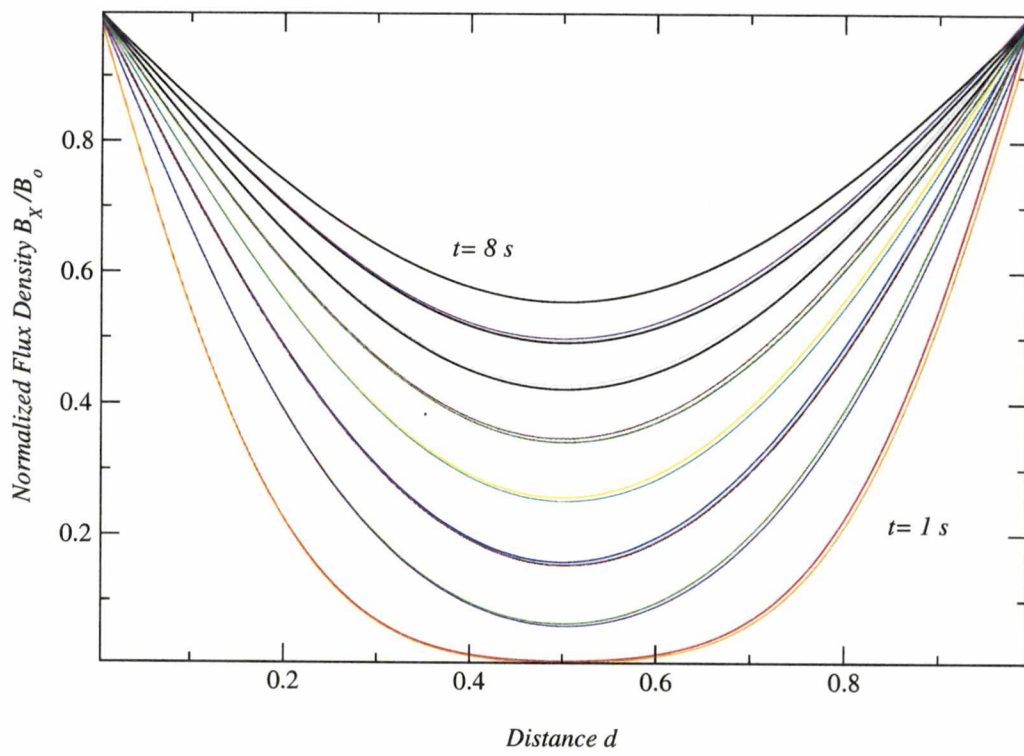


Figure 6.3: Analytical solution combined with numerical results.

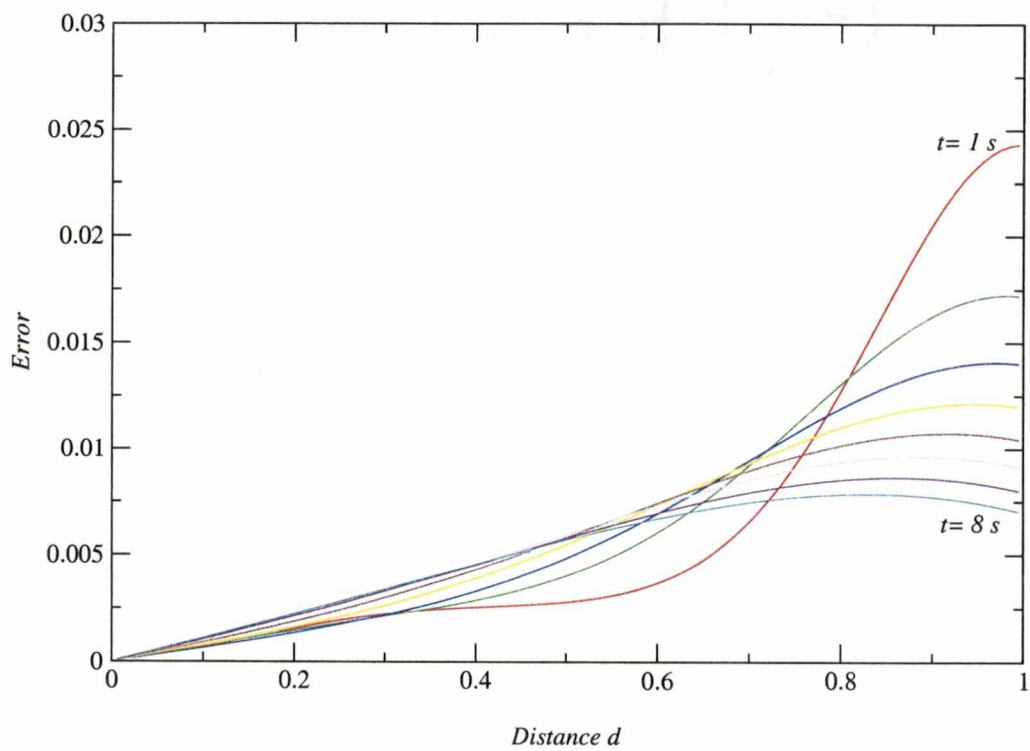


Figure 6.4: Error in solution.

Chapter 7

Conclusions

In this dissertation a new type of machine structure was developed and analyzed. The machine was constructed from a new class of materials which possess very small magnetic losses especially at elevated frequencies. The negative aspects of utilizing the material was overcome by using permanent magnets with high coercive force to produce a reasonable air gap flux density in the presence of the high reluctance material. The use of inexpensive round magnets rotating over round pole pieces presented a need to develop the governing equation for the back-emf. The equations for designing a motor of this configuration were developed. In addition, the back-emf was analyzed by Fourier methods to develop a simple representation for the generated voltage. The modular motor was characterized by operating the machine as a generator to verify the developed equations. The modular motor requires an inverter for operation; thus, the practical implementation of driving the machine with a microcontroller-based electric drive was developed and explained.

As with all machines, the overall efficiency is related to the losses. The losses in rotating electric machines are generally dominated by I^2R loss, hysteresis loss and eddy current loss. The ability to predict the amount of eddy current and thus the loss, is paramount in developing highly efficient electric machines. The development of an algorithm to calculate the eddy current

problem in an efficient way utilizing the control volume method was described. The algorithm was applied to a one dimensional test problem to validate the numerical approximation to the magnetic diffusion problem. The algorithm calculated the transient effect of a B field diffusing through a slab of material.

7.1 Recommendations for Future Research

The material presented in this document provides a basis for further study and research in the following key areas:

- Design and analysis of the separable pole piece machine with trapezoidal back-emf. Additionally, eliminating the encoder and simplifying the inverter drive to reduce cost.
- Develop an integrated design program to design a modular machine based on size and power constraints and incorporate the methods developed in Chapter 5 to calculate the eddy currents. Based on the accurate representation of the eddy current loss, develop optimizing routines to create an optimal machine.
- Extend the finite volume method to include the effects of moving media. In particular, apply the control volume technique to analyze the dynamic coupled circuit problem accounting for the effect of eddy current on the solution.

References

References

- [1] W. F. Hall A.H. Mohammadian, V. Shankarand. "Computation of the Electromagnetic Scattering and Radiation using a Time-domain Finite Volume Discretization Procedure". *Comp. Phys. Comm.*, (68):175–196, 1991.
- [2] V. Alexiades. "Math 579 Lecture Notes". May 1996.
- [3] V. Alexiades and A. D. Solomon. *Mathematical Modeling of Melting and Freezing Processes*. Hemisphere Publishing Corporation, 1993.
- [4] A.R. Bergen. *Power Systems Analysis*, chapter 10, pages 296–313. Prentice-Hall, Englewood Cliffs, N.J., 1986.
- [5] B.K. Bose. *Power Electronics and AC Drives*. Prentice-Hall, Englewood Cliffs, N.J., 1986.
- [6] B.K. Bose. *Power Electronics and Variable Frequency Drives*". IEEE Press, Piscataway, N.J., 1997.
- [7] P. Campbell. "The Magnetic Circuit of an Axial Field D.C. Electrical Machine". *IEEE Transactions on Magnetics*, MAG-11(5):1541–1543, September 1975.
- [8] Atmel Corporation. *AVR[®] RISC Microcontroller Databook*. Atmel Corporation, 1999.

REFERENCES

- [9] C.S. Biddlecombe, E.A. Heighway, J. Simkin and C.W. Trowbridge. "Methods for Eddy Current Computation in Three Dimensions". *IEEE Transactions on Magnetics*, MAG-18(2):492-497, March 1982.
- [10] D. S. Daniel and R.W. Wies. "Volume IV-A: Year 2 Final Subcontract Report". Technical report, University of Alaska, 2000.
- [11] E.A. Erdelyi. "Nonlinear Magnetic Field Analysis of DC Machines". *IEEE Trans. on Power Apparatus and Systems*, PAS-89:1546-1554, Sept.-Oct. 1970.
- [12] D.C. Hanselman. *Brushless Permanent Magnet Motor Design*. McGraw-Hill, 1994.
- [13] H.G. Rutz, F.G. Hanejko and G.W. Ellis. The Manufacture of Electromagnetic Components by the Powder Metallurgy Process. Chicago, IL, June 29 - July 2 1997. International Conference on Powder Metallurgy & Particulate Material.
- [14] R. Holland. "Finite-difference solution of Maxwell's Equations in generalized nonorthogonal coordinates". *IEEE Trans. Nucl. Sci.*, NS-30:pp. 4589-4591, 1983.
- [15] E. Isaacson and H.B. Keller. *Analysis of numerical methods*. John Wiley & Sons New York, 1966.
- [16] R. Krishnan and A.J. Beutler. "Performance and Design of an Axial Field PM Synchronous Motor Servo Drive". pages pp 634-640. IEEE - IAS Conference Record, Oct. 1985.
- [17] M.F. Magdy M. J. White and Z. Huang. Development of a multigrid FDTD Code for Three-Dimensional Applications. *IEEE Transactions on Antennas and Propagation*, 45(10):1512-1517, October 1997.
- [18] H.G. Rutz and F.H. Hanejko. High Density Processing of High Performance Ferrous Materials. Toronto, Canada, May 8-11 1994. International Conference & Exhibition on Powder Metallurgy & Particulate Materials.

REFERENCES

- [19] K.L. Shlager and J.B. Schneider. "A Selective Survey of the Finite-Difference Time-Domain Literature". *IEEE Antennas & Propagation Magazine*, 37(4):39–56, March 1995.
- [20] C.W. Steele. *Numerical Computation of Electric and Magnetic Fields*. Chapman & Hall, 1997.
- [21] A. Taflove. "Review of the formulation and application of the finite-difference time-domain method for numerical modeling of electromagnetic wave interactions with arbitrary structures". *Wave Motion*, 10(6):pp. 547–582, 1988.
- [22] A. Taflove and M.E. Brodwin. "Numerical Solution of Steady-State Electromagnetic Scattering Problems Using the Time-Dependent Maxwell's Equations". *IEEE Transactions on Microwave Theory and Techniques*, MTT-23(8):623–630, August 1975.
- [23] T.W.Preston and A.B.J. Reece. Solution of 3-Dimensional Eddy Current Problems The T- Ω Method. *IEEE Transactions on Magnetics*, MAG-18(2):486–491, March 1982.
- [24] A.J. Wijenayake. Design and efficiency optimization of an axial gap permanent magnet synchronous machine adjustable speed drive. University of Tennessee-Knoxville, PhD. Dissertation, August 1995.
- [25] H.H. Woodson and J.R. Melcher. *Electromechanical Dynamics*, volume I,II,III. John Wiley and Sons, Inc., 1968.
- [26] K.S. Yee. "Numerical solution of initial boundary value problems involving Maxwell's equations in isotropic media". *IEEE Transactions on Antennas and Propagation*, AP-14(4):pp302–307, 1966.

Appendices

Appendix A

Flux Derivation

A.1 Salient Motor Design Equations

A.1.1 Air Gap Flux

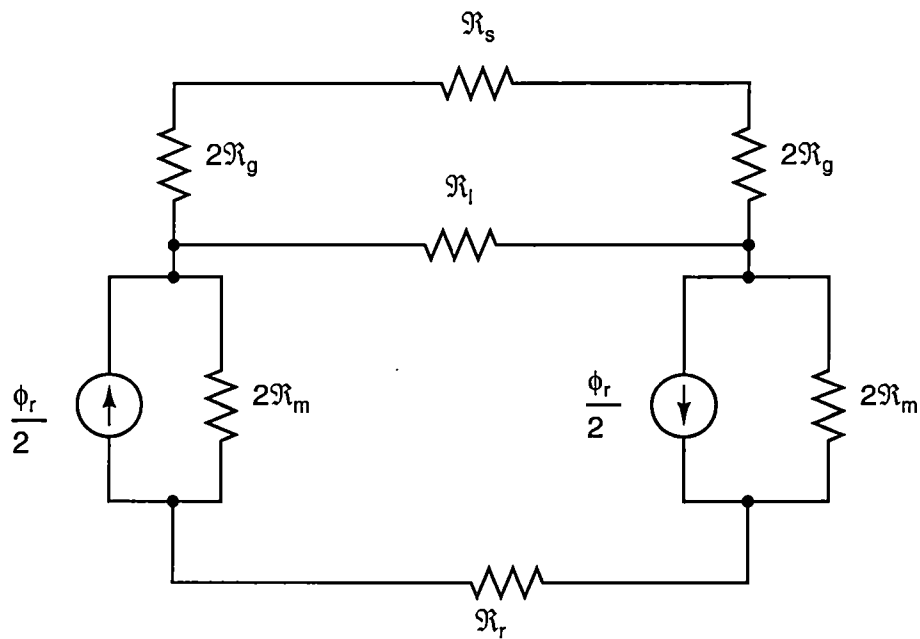


Figure A.1: Reluctance model of single air gap stator.

APPENDIX A. FLUX DERIVATION

A first order approximation for the airgap flux is calculated by utilizing the simple reluctance model of the single airgap machine as shown in Figure A.1. By utilizing a source transformation, the equations governing the equivalent circuit may be written as:

$$\begin{bmatrix} 4\mathfrak{R}_m + \mathfrak{R}_l + \mathfrak{R}_r & -\mathfrak{R}_l \\ -\mathfrak{R}_l & 4\mathfrak{R}_g + \mathfrak{R}_l + \mathfrak{R}_s \end{bmatrix} \begin{bmatrix} \phi_b \\ \phi_t \end{bmatrix} = \begin{bmatrix} 2\phi_r \mathfrak{R}_m \\ 0 \end{bmatrix}. \quad (\text{A.1})$$

Solving A.1 for ϕ_t , the flux through the stator:

$$\phi_t = \frac{2\phi_r \mathfrak{R}_m \mathfrak{R}_l}{\Delta R} \quad (\text{A.2})$$

where ΔR is the determinant of the reluctance matrix in A.1,

$$\Delta R = 16\mathfrak{R}_m \mathfrak{R}_g + 4\mathfrak{R}_m \mathfrak{R}_l + 4\mathfrak{R}_m \mathfrak{R}_s + 4\mathfrak{R}_g \mathfrak{R}_l + \mathfrak{R}_l \mathfrak{R}_s + 4\mathfrak{R}_g \mathfrak{R}_r + \mathfrak{R}_r \mathfrak{R}_l + \mathfrak{R}_r \mathfrak{R}_s \quad (\text{A.3})$$

The airgap flux ϕ_g can be observed to be $2\phi_t$ from Figure A.1, combining this with A.2, the air gap flux can be written as:

$$\phi_g = \frac{4\phi_r \mathfrak{R}_m \mathfrak{R}_l}{\Delta R}. \quad (\text{A.4})$$

For a machine utilizing the Hoeganees material or a material that has a low permeability equation A.4 provides a starting point for estimating the air gap flux. The flux expression can be used to develop an expression for the air gap flux density by noting that for the modular motor with round magnets and round pole pieces $A_m = A_g$ so that equation A.4 becomes,

$$B_g = \frac{4B_r \mathfrak{R}_m \mathfrak{R}_l}{\Delta R}. \quad (\text{A.5})$$

For machines where the permeability of stator and rotor steel is 300-1000 times μ_o , $\mathfrak{R}_g \gg \mathfrak{R}_s$ and

APPENDIX A. FLUX DERIVATION

$\mathfrak{R}_g \gg \mathfrak{R}_r$, we can let $\mathfrak{R}_s = \mathfrak{R}_r = 0$, simplifying equation A.4, the air gap flux can be represented as

$$\phi_g = \frac{\phi_r \mathfrak{R}_m \mathfrak{R}_l}{4\mathfrak{R}_m \mathfrak{R}_g + \mathfrak{R}_m \mathfrak{R}_l + \mathfrak{R}_g \mathfrak{R}_l}. \quad (\text{A.6})$$

A more natural form of equation A.6 can be formed by converting all of the reluctances into permeances and since $\wp = \frac{1}{\mathfrak{R}}$ we can substitute into equation A.4, equation A.6 and simplify. The air gap flux becomes a ratio of the permeances multiplied by the permanent magnet residual flux and can be shown to be for the low permeability material,

$$\phi_g = \frac{2\wp_g \wp_r \wp_s \phi_r}{\wp_{den}} \quad (\text{A.7})$$

where,

$$\wp_{den} = 16\wp_l \wp_r \wp_s + 4\wp_g \wp_r \wp_s + 4\wp_l \wp_g \wp_r + 4\wp_m \wp_r \wp_s + 4\wp_m \wp_l \wp_s + \wp_m \wp_r \wp_g + \wp_m \wp_g \wp_s + \wp_m \wp_l \wp_g$$

and for the second case where the relative permeability of the material is high,

$$\phi_g = \frac{\wp_g \phi_r}{4\wp_l + \wp_g + \wp_m}. \quad (\text{A.8})$$

Equation A.8 relates the residual flux of the permanent magnets to the air gap flux, to determine the air gap flux density and generated EMF it is necessary to develop several additional relationships. The air gap flux and residual magnet flux are represented as:

$$\begin{aligned} \phi_g &= B_g A_g \\ \phi_r &= B_r A_m, \end{aligned} \quad (\text{A.9})$$

for the wedged shaped magnets used in the semi-square wave motor, the ratio of the area of the magnet to the air gap can be defined as,

$$\tau = \frac{A_m}{A_g}. \quad (\text{A.10})$$

Combining equation A.10 and equation A.9 with equation A.8, the air gap flux can be written as,

$$B_g = \frac{2\tau\varphi_g\varphi_r\varphi_s B_r}{\varphi_{den}}, \quad (\text{A.11})$$

and for the high permeability material,

$$B_g = \left(\frac{\tau B_r \varphi_g}{4\varphi_l + \varphi_g + \varphi_m} \right). \quad (\text{A.12})$$

By setting $\widehat{\varphi}_m = 4\varphi_l + \varphi_m$ in equation A.12 it is written as

$$B_g = \frac{\tau B_r \varphi_g}{\varphi_g + \widehat{\varphi}_m}. \quad (\text{A.13})$$

A.1.2 Calculation of Permeances

The general form of reluctance is defined as $\mathfrak{R} = \frac{l}{\mu A}$, the magnet reluctance is written as

$$\mathfrak{R}_m = \frac{T_{ma}}{\mu_r \mu_o \pi r_m^2}; \quad (\text{A.14})$$

thus, the magnet permeance becomes

$$\varphi_m = \frac{\mu_r \mu_o \pi r_m^2}{T_m}. \quad (\text{A.15})$$

To calculate the permeance due to leakage, it is necessary to make use of an equation for the leakage permeance, this equation is presented in and was formulated based on wedge shaped magnets with a constant spacer τ_f ,

$$\varphi_l = \frac{\mu_o (R_o - R_i)}{\pi} \ln \left[1 + \pi \frac{g}{\tau_f} \right]$$

to allow for the round magnets with non-constant τ_f , the thickness between the magnets will be approximated as $\tau_f = 4\tau_{fmin}$, then the leakage permeance for an axial gap, round magnet machine may be approximated as

$$\varphi_l = \frac{\mu_o (R_o - R_i)}{\pi} \ln \left[1 + \pi \frac{g}{4\tau_{fmin}} \right]. \quad (\text{A.16})$$

The air gap permeance is

$$\varphi_g = \frac{\mu_o A_g}{g_e} = \frac{\pi \mu_o (R_o^2 - R_i^2)}{g_e N_m} \quad (\text{A.17})$$

where g_e is known as the effective gap area and results from the slotting of the core.

The slotting of the core lengthens the effective air gap, therefore; g_e is highly dependent on the slot geometry and is represented by $g_e = k_c g$ where k_c is the Carter coefficient, the factor representing the alteration of the air gap due to the shape of the slot. The Carter coefficient has various forms and is discussed in a variety of literature [12], the form used in the present design is

$$k_c = \left[1 - \frac{1}{\frac{2\pi R_i}{w_s N_s} \left(5 \frac{g_c}{w_s} + 1 \right)} \right], \quad (\text{A.18})$$

where $g_c = g + \frac{T_m}{\mu_r}$. Where g represents the physical air gap between the rotor magnets and the factor $\frac{T_m}{\mu_r}$ represents the effective distance due to the permanent magnets. The expressions for air gap flux and flux densities have been derived, the next step is to develop an expression for the generated voltage based on speed, flux density and the physical geometry of the machine.

Appendix B

Derivation of Back-EMF Equation

The analysis that follows assumes the following:

1. The flux is constant over the pole surface and directed in the \hat{z} direction. This is not generally the case but, a first order approximation can be made.
2. There is no interaction with the stator field, i.e. armature reaction is neglected.

B.1 Round Magnets

To develop the generated voltage equation it is necessary to begin with Faraday's law and modify it for this particular case. Thus,

$$e = -N \frac{d\phi}{dt}, \quad (\text{B.1})$$

where ϕ is the flux and given by $\phi = BA$, $B = \text{constant}$, $N = \# \text{ of turns}$:

$$e = -NB \frac{dA}{dt} \quad (\text{B.2})$$

which may also be written as:

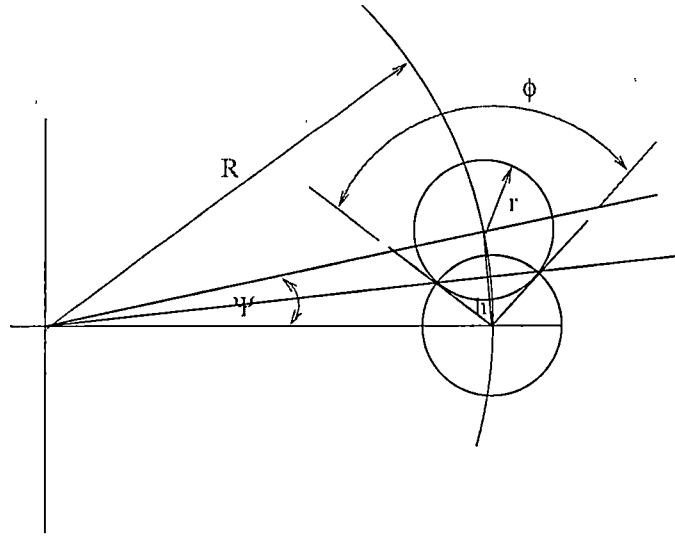


Figure B.1: Geometrical representation of magnet rotating over pole face

$$e = -NB \frac{dA}{d\psi} \frac{d\psi}{dt} = -NB \frac{dA}{d\psi} \omega, \quad (\text{B.3})$$

where ψ = rotation angle and ω = speed $\frac{\text{rad}}{\text{s}}$.

B.1.1 Calculation of area and its derivative

To derive the final equation it will be necessary to develop an expression for the area swept as a function of rotation angle ψ and then to differentiate the result. To aid in developing an expression for the area as a function of rotation angle Figure B.1 illustrates the case. The approach is to calculate the total area swept from ϕ_1 to ϕ_2 and then to subtract the areas of the two triangles inscribed within the circle. Once this has been achieved, the area swept is related to the global coordinate system. The area of the pole piece is given by:

$$A_p = \frac{\phi}{2} r^2. \quad (\text{B.4})$$

The area of each inscribed triangle is:

APPENDIX B. DERIVATION OF BACK-EMF EQUATION

$$A_t = \frac{1}{2} h \sqrt{r^2 - h^2}. \quad (\text{B.5})$$

The area swept is,

$$A = \frac{\phi}{2} r^2 - h \sqrt{r^2 - h^2}. \quad (\text{B.6})$$

Equation (B.6) may be simplified by noting that,

$$\frac{\phi}{2} = \arccos \left(\frac{h}{r} \right) \quad (\text{B.7})$$

and

$$h = R \sin \left(\frac{\psi}{2} \right). \quad (\text{B.8})$$

Substituting equations (B.7) and (B.8) into equation (B.6) the total area swept by the magnet across the pole face is:

$$A_{sw} = 2 \left[\cos^{-1} \left(\frac{R \sin \left(\frac{\psi}{2} \right)}{r} \right) r^2 - R \sin \left(\frac{\psi}{2} \right) \sqrt{r^2 - R^2 \sin^2 \left(\frac{\psi}{2} \right)} \right]. \quad (\text{B.9})$$

Equation (B.9) is valid for $h \leq r$ which implies that,

$$\psi \leq 2 \arcsin \left(\frac{r}{R} \right). \quad (\text{B.10})$$

Differentiating equation (B.9) and substituting into equation (B.3) it can be shown that,

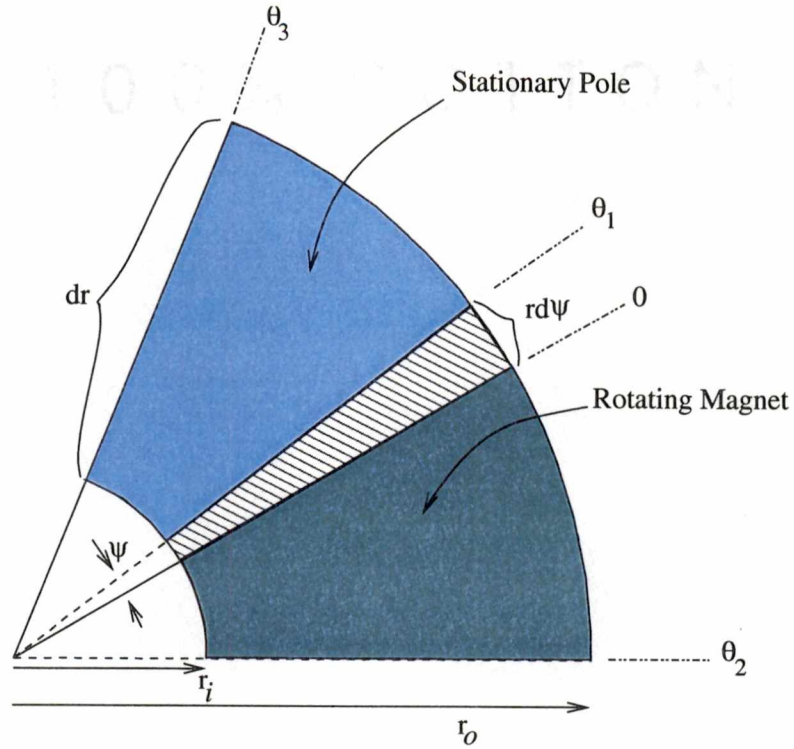


Figure B.2: Wedge shaped magnets.

$$e = \frac{-NB\omega}{\sqrt{r^2 - R^2 \sin^2 \left(\frac{\psi}{2} \right)}} \left[\left(\frac{R^3}{2} \right) \left(\sin \left(\frac{\psi}{2} \right) \sin (\psi) - \cos \left(\frac{\psi}{2} \right) \cos (\psi) + \cos \left(\frac{\psi}{2} \right) \right) - 2r^2 R \cos \left(\frac{\psi}{2} \right) \right].$$

(B.11)

B.2 Wedge Shaped Magnets

For the design with wedge shaped magnets, another equation can be derived that represents the generated voltage as the rotor turns. The analysis begins with utilizing B.3, and noting that

APPENDIX B. DERIVATION OF BACK-EMF EQUATION

the generated voltage becomes a function of the change in area as related to the global coordinate system ψ . Figure B.2 depicts the area swept as a function of ψ . As the magnet rotates counter-clockwise, in the region where $\theta_1 \leq \theta_3$ the area can be calculated by,

$$A_1 = \int_0^{\theta_1} \int_{r_i}^{r_o} r dr d\psi = \frac{r_o^2 - r_i^2}{2} \theta_1. \quad (\text{B.12})$$

As θ_1 approaches θ_3 there will be complete overlap if the dimensions of the pole piece and magnet are the same. As the magnet continues to move past θ_3 the area swept will be,

$$A_2 = \int_{\theta_2}^{\theta_3} \int_{r_i}^{r_o} r dr d\psi = \frac{r_o^2 - r_i^2}{2} (\theta_3 - \theta_2) \quad (\text{B.13})$$

the derivative of B.12 as a function of angle is,

$$\frac{dA_1}{d\theta_1} = \frac{r_o^2 - r_i^2}{2}. \quad (\text{B.14})$$

Since θ_3 is a fixed constant dependent on motor geometry, the derivative of B.13 as a function of angle is,

$$\frac{dA_2}{d\theta_2} = -\frac{r_o^2 - r_i^2}{2}. \quad (\text{B.15})$$

Equations B.14 and B.15 show that the area swept is constant and positive for angles $\leq \theta_3$ and constant and negative as the magnets rotate past θ_3 . Combining equation B.3 with B.14, the peak value for the generated voltage becomes,

$$e_{max} = -NB \frac{r_o^2 - r_i^2}{2} \omega. \quad (\text{B.16})$$

The generated voltage is shown in figure B.3, with the actual voltage superimposed over the theoretical voltage to illustrate that due to B_z not being continuous over the pole face of

APPENDIX B. DERIVATION OF BACK-EMF EQUATION

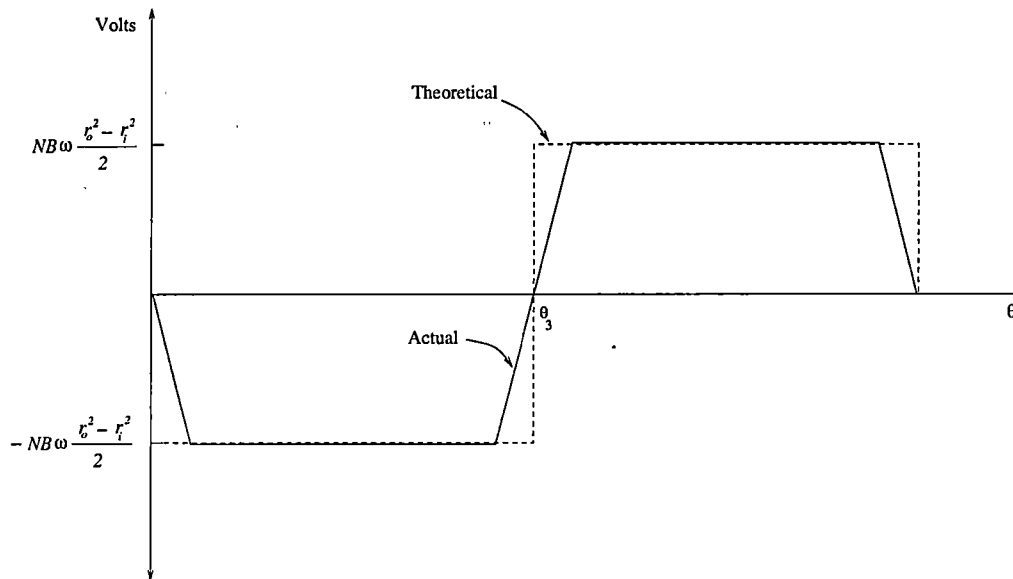


Figure B.3: Graph of actual versus theoretical back-emf.

the magnet, the generated voltage is not exactly square but more trapezoidal. The shape of B_z in an axial machine was first determined numerically by Campbell [7] and later analytically by Wijenayake [24].

Appendix C

Electronic Drive Design

The nature by which the machine produces torque requires that the supply voltage be switched alternatively positive and negative depending on the position of the rotor, this may be accomplished in many ways both mechanically and electrically. The most efficient means by which create a bipolar voltage across a load is by utilizing 4 transistors in an H-bridge arrangement and alternatively switching the upper and lower legs to create the desired waveform across the load. The actual timing and level of the voltage delivered to the load by the H-bridge inverter can either be controlled by discrete logic or by utilizing a microprocessor based system. In this particular application, there are no sophisticated control algorithms or peculiar timing requirements that would require a digital signal processor.

There exists many trade-offs when deciding on whether to utilize discrete logic, programmable logic, a microprocessor, or a custom integrated circuit. The use of discrete logic is generally the least expensive but also the least robust. Additionally, the amount of real estate necessary to accomplish the goal is much greater than the other methods. Utilizing programmable logic can address the real estate issue but does little to circumvent the problem associated with flexibility. The use of programmable logic reduces the size of the controller but once the device is programmed and the support hardware designed, it is difficult to make even minor changes. For

maximum flexibility, a microcontroller with integrated counters, A/Ds and programmable I/O is generally used. Once the software and hardware have been debugged, and if sufficient volume exists, a custom integrated circuit may be a cost and space effective means to provide the control functions. To provide a robust platform in which to study the characteristics of the integrated motor, a microprocessor based motor control is briefly discussed in the next section, many of the finer design details have been omitted for clarity.

C.1 Controller Requirements

The controller must perform several different functions, these can be delineated into four categories:

1. Data acquisition.
2. Switch pattern generation.
3. Error protection

Data Acquisition

The controller is responsible for gathering and interpreting data from the bus voltage, current sensor and position encoder. The bus voltage sensing is implemented utilizing a simple isolated voltage divider fed into the A/D multiplexer of the microcontroller. The sample time is not a critical parameter for this drive but can be programmed in software.

The position encoder is required to provide feedback to the controller as to the relative position of the rotor. The absolute rotor position is not necessary once the machine is rotating; thus, position relative to the last switch point provides sufficient information to the controller to decide on the next switch point. The encoder chosen was a US Digital H1-1024 optical shaft encoder

that produces a 1024 quadrature pulses per revolution. Since the prototype machine consists of 10 poles, there is 36° between each pole face. The encoder will provide a resolution of:

$$E_{res} = \frac{36^\circ}{1024} = .0352^\circ$$

The encoder provides two pulse trains separated by 90° , these pulse trains must be decoded to provide position and direction information, an integrated circuit designed by LSI was utilized. This circuit provides direction information and a clock suitable to the up/down counter available on the microcontroller. In addition, the circuit can implement a 1 or 4 times mode programmable via the microcontroller. The 4 times mode effectively quadruples the resolution of the encoder.

Switch Pattern Generation

The drive has the capability to operate in two distinct modes: square wave and modulated. The square wave mode is one in which the output switches are turned on for a certain rotation angle and then turned off producing a bipolar square wave voltage with a peak-peak value equal to the DC link voltage. In this mode, the amplitude of the voltage across the motor terminals is not software adjustable and can only be changed by adjusting the input voltage to the main rectifiers. The impressed voltage and back-emf are shown in figure C.1 .

Error Protection

To ensure proper drive operation, it is necessary to monitor the drive fault outputs, motor speed, bus voltage and current. These quantities are constantly monitored by the microcontroller in all modes. The Powerex Intellimod produces 4 fault signals: WFO, VFO, UFO and FO which provide feedback to the controller regarding the status of a switching cycle. For instance, if the blank time is not sufficient on a particular phase, the module will not allow a shoot-through fault and will indicate the fault back to the controller. The controller is responsible for clearing the

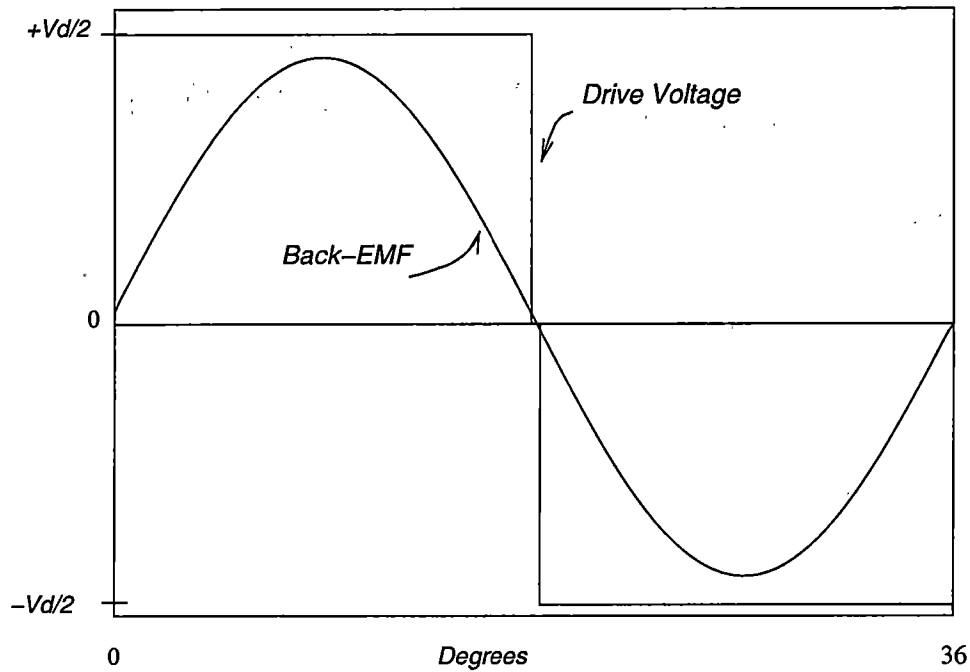


Figure C.1: Inverter Square Wave Mode.

fault and continuing with the proper switching sequence.

C.2 Power Circuitry

The power circuitry is designed using an intelligent power module (IPM) from the Powerex Corporation. These particular devices are extremely easy to interface to micro controllers and digital signal processors; they also generate error signals for several common conditions encountered in electric drives such as short circuit, over current, over temperature and under voltage.

C.2.1 Circuit Description

Control Section

The schematic of power circuit is shown in figure C.2. The PM10CSJ060 is a six transistor IGBT bridge with a maximum voltage rating of 600 V and a maximum current rating of 10 Amps. The interface is simple, with 3 power outputs, 4 fault outputs, 2 power inputs, 6 control inputs and 8 power supply inputs. The pins are denoted as follows: the power outputs W,V,U; the fault outputs WFO, VFO, UFO and FO; the power inputs P and N; control inputs WP,VP,UP, UN,VN and WN: and the power supply pins VWP1, VWPC, VVP1, VVPC, VUP1, VUPC,VN1 and VNC.

The inputs to the Powerex module are supplied by 6 high speed digital opto-couplers, OK2, OK8, OK10, OK12, OK13 and OK14. These opto-couplers isolate the high power, high voltage electronics from the low power, low voltage control circuitry; thereby, protecting the microcontroller from damage in the event of a catastrophic failure. The circuit design for the drive signal isolation is straightforward and will not be discussed. As a result of the optical isolation, the Powerex module requires 4 15 V isolated power supplies. The top three power switches require one isolated supply each and the remaining supply powers all three of the lower legs. The isolated power supply was implemented by purchasing a M57994 isolated DC-DC converter from Powerex, its main feature is its low profile and wide input supply range making it ideal for small motor drives.

The fault outputs of the IPM are also isolated from the control, this was implemented utilizing standard speed 4N35 opto-isolators which produce an active low signal to indicate a fault. The fault signal causes an interrupt to be executed by the microcontroller which services the interrupt in the following priority: WFO, VFO, UFO and FO.

Power Section

The power section in figure C.2 are the entities to the right of the IPM. These include the bridge rectifier, filter capacitors, output terminals, current sensor and the snubber capacitor.

The DC bus is formed by diodes Dx-Dy and paralleled filter capacitors C1 and C14. Resistors R20 and R21 serve two functions, one to bleed off the charge on the capacitors on power-down and secondly to limit the current in OK3. Components R22, OK3 and R23 form the DC link feedback circuit. The DC link voltage is monitored by the microcontroller through one of the eight analog multiplexor inputs.

The current is monitored by an Amploc CS50-P closed loop current sensor with a 3db bandwidth of 100kHz. The sensor produces an output current proportional to one thousandth of the sensed current; the output is directly connected to a shunt resistor which converts the current to a voltage. To provide a low impedance source to the A/D, the sense resistor is followed by an inverting op- amp circuit with the offset and gain set to 2.5VDC and 3.4 , respectively. The gain was chosen to produce a peak output of approximately 5 volts at a sensed current of 30 amps. The single-pole 3db bandwidth was set to 6 kHz to eliminate the switching frequency from the A/D sampling; thereby, reducing the required sampling rate.

C.3 Microcontroller Section

The microcontroller selected to implement the proper switching sequence and handle the overhead functions is an ATmega 103 manufactured by the Atmel Corporation. The microcontroller is based on a 4MHz RISC processor and has 128K of in-circuit programmable flash ROM for programming space, the details of the peripherals available on the ATmega103 can be found in [8]. The development tools available for the processor range from an assembler and simulator provided by Atmel to a port of GNU's gcc, binutils, libc and gdb. The GNU ports allow programmers familiar with the GNU toolset to rapidly develop applications. The schematic for the control

section of the drive is shown in C.3 and can be separated into 3 sections for discussion: Encoder signal conditioning, LCD drive and support functions and are discussed below.

Encoder Signal Conditioning

The circuitry required to condition the encoder signal for the microcontroller is provided by SW1, R12, C3, R6, R8-10 and the LS-7083. The relative optical encoder produces a set of TTL level pulses in quadrature where the phase of the signals are decoded to indicate direction. The LS-7083 is an integrated circuit produced by the LSI Corporation to condition and detect the pulses produced by the encoder. The LS-7083 requires 4 inputs for control and 2 for power; the control inputs consists of a X1/X4 input from SW2 which provides a resolution multiplier, the Ain and Bin inputs are the two inputs from the encoder and the bias current is provided by R6. The outputs from the LS-7083 are the CLK and UP/DN; in this particular design, the UP/DN is left unconnected since the rotation is unidirectional. The CLK signal is routed to the T1 input on the ATmega103 which is the external timer/counter 1 input. The encoder also produces an index pulse every revolution and is counted by timer/counter 2 via the PD7-T2 multiplexed pin. This signal is used to determine the speed of rotation.

LCD Interface

Although not necessary for operation, a liquid crystal display is interfaced to the microcontroller to provide current and voltage information in human readable form. In addition, the LCD provides a means to extract debugging information from the motor drive. The LCD is interfaced via the memory mapped I/O mode of the ATmega103, in this mode each device must reside at a particular address, the address of the LCD is decoded by IC2, a PALCE22V10 programmable logic device (PLD). The PLD contains the logic to decode multiple addresses, in the event that another peripheral is added to the controller, the hardware required to address the device is in place. The LCD has its own microcontroller and character generator; therefore, the ATmega103

needs only to send command strings and display data to the device. The data is presented to the LCD via the data bus while the ATmega103 is in the memory mapped I/O mode. Potentiometer R10 provides a bias voltage to the LCD to adjust the contrast of the display.

Support Functions

For proper operation the microcontroller requires a stable clock source, this is provided by an external 4Mhz clock QG1. In addition, for a real time clock source a separate 32.766kHz clock Q1 is also included. The power-on-reset circuitry is formed by the combination of T1, D1, R4, C2 and R5. Its function is to hold the processor in reset until all of the internal registers can be initialized and the RAM cleared. D1 provides a low impedance path to allow C2 to discharge rapidly upon power-down.

In order to input set points, components C1, R1, R2 and R3 form a stable voltage divider that provides the ATmega 103 with a analog voltage proportional to the set point, it is then sampled by the A/D converter and saved into RAM. To provide visual feedback to the user during setup and alignment of the encoder, LEDs D2-D5 are connected to the general I/O port B through current limiting resistors R7, R13, R14 and R15.

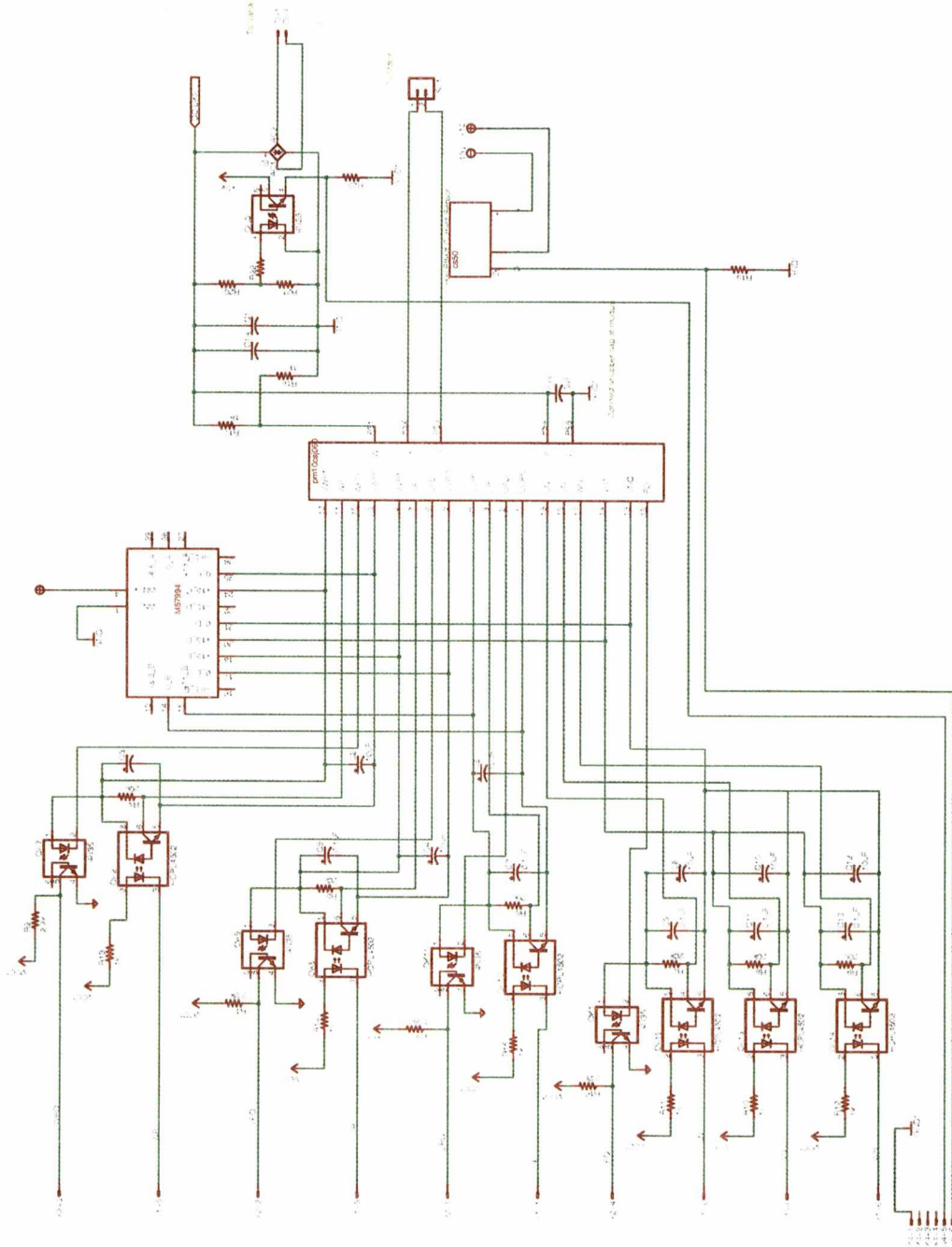


Figure C.2: Power Section.

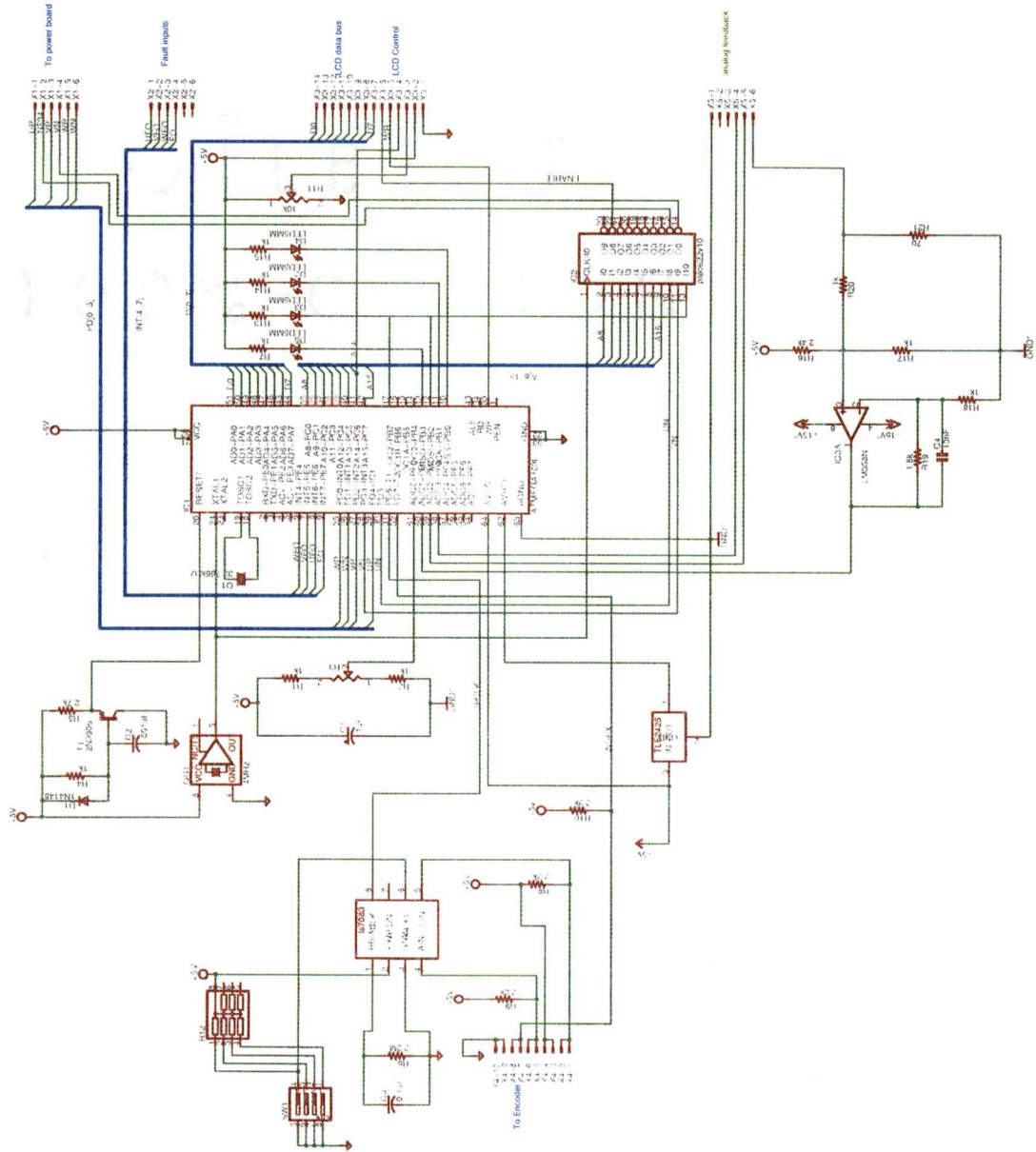


Figure C.3: Microcontroller Section.

Appendix D

Microcontroller Source Code

```
#include "atmega103.h"

int start_flag;

int state;

int gerror;

int enable; // Set enable variable

void delay2(unsigned char);

void initialize(void)
{
    DDRB=0xFF;    // Sets the Data direction register to all outputs
    TCCR0=0x05;   // Set the timer control register to divide by 128
    TCCR2=0x07;   // Set timer 2 to clock on external PD7 (remove jumper)
    TCNT2=0x00;   // Initializes counter zero
    PORTD=0x00;   // Enable port D inputs
}
```

APPENDIX D. MICROCONTROLLER SOURCE CODE

```
void error(int errnum)
{

while (gerror==1) {
switch(errnum){
case(1): PORTB=0xAF; break;

}

}
}
```

```
void state2(void)
{

TCNT2=0;
while(TCNT2<=10){
PORTB=0xF6;
}
TCNT2=0;
while(TCNT2<=10){
PORTB=0xF9;
}

}
```

```
void state1(void)
```


APPENDIX D. MICROCONTROLLER SOURCE CODE

```
{

    TCNT2=0;
    while(TCNT2<=10){
        PORTB=0xF9;
    }
    TCNT2=0;
    while(TCNT2<=10){
        PORTB=0xF6;
    }

}

void start(void)
{
    unsigned char delay_mult=128; // Steps of 32uS delay_time=delay_mult*32uS

    TCNT2=0x00;
    PORTB=0x09; // Set output to attempt to start motor
    delay2(delay_mult);

    if(TCNT2<=3){
        TCNT2=0;
        PORTB=0x06;
        state=0;
    }
}
```

APPENDIX D. MICROCONTROLLER SOURCE CODE

```
TCNT2=0;
delay2(delay_mult);
if(TCNT2<=3){
    gerror=1;
    error(1);
}
}
else {
    PORTB=0x09;
    state=1;
}

    start_flag=1;
}
void enable_op(void)
{

while(!enable){
    PORTB=0xFF;
    enable!=(PIND & 0x01);
}

}

void check_operations(void)
{
```

APPENDIX D. MICROCONTROLLER SOURCE CODE

```
if((PIND & 0x02)==0){  
    enable=0; // turn output off if second switch is hit  
    start_flag=0; // reset start flag so unit starts from standstill  
}  
}
```

```
void run(void)
```

```
{  
    if(state==1)  
    {  
        state1();  
    }  
    else  
    {  
        if(state==0)  
        {  
            state2();  
        }  
    }  
}
```

```
int main(void)
```

```
{
```

APPENDIX D. MICROCONTROLLER SOURCE CODE

```
initialize(); // Call function to initialize port and counter
start_flag=0;
enable=0; // Disable operation on startup
while(1)
{
    enable_op();
    if(start_flag==0)
    {
        start();
    }

    run();

    check_operations();
}
}
```

Appendix E

Mechanical Drawings

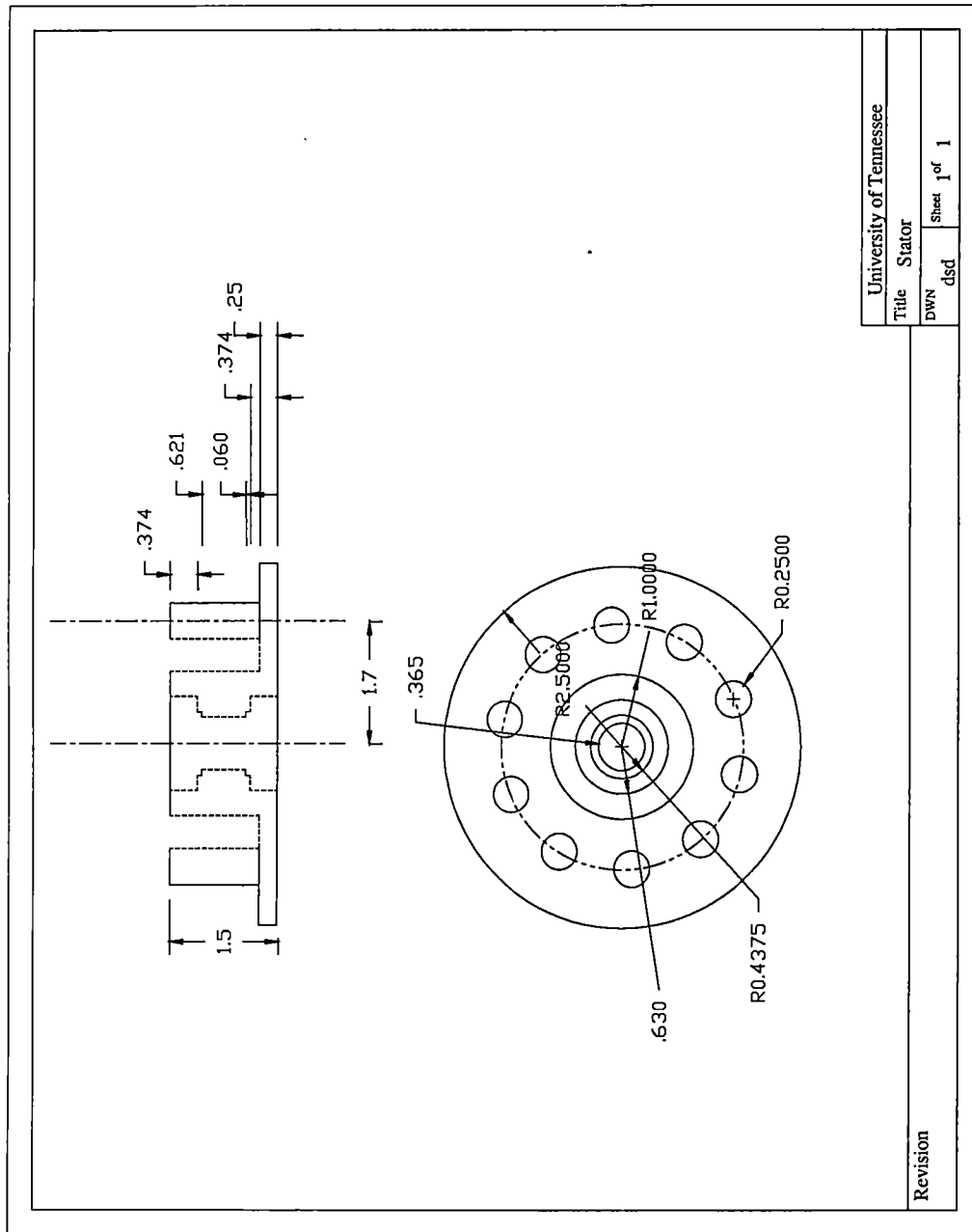


Figure E.1: Prototype stator drawing.

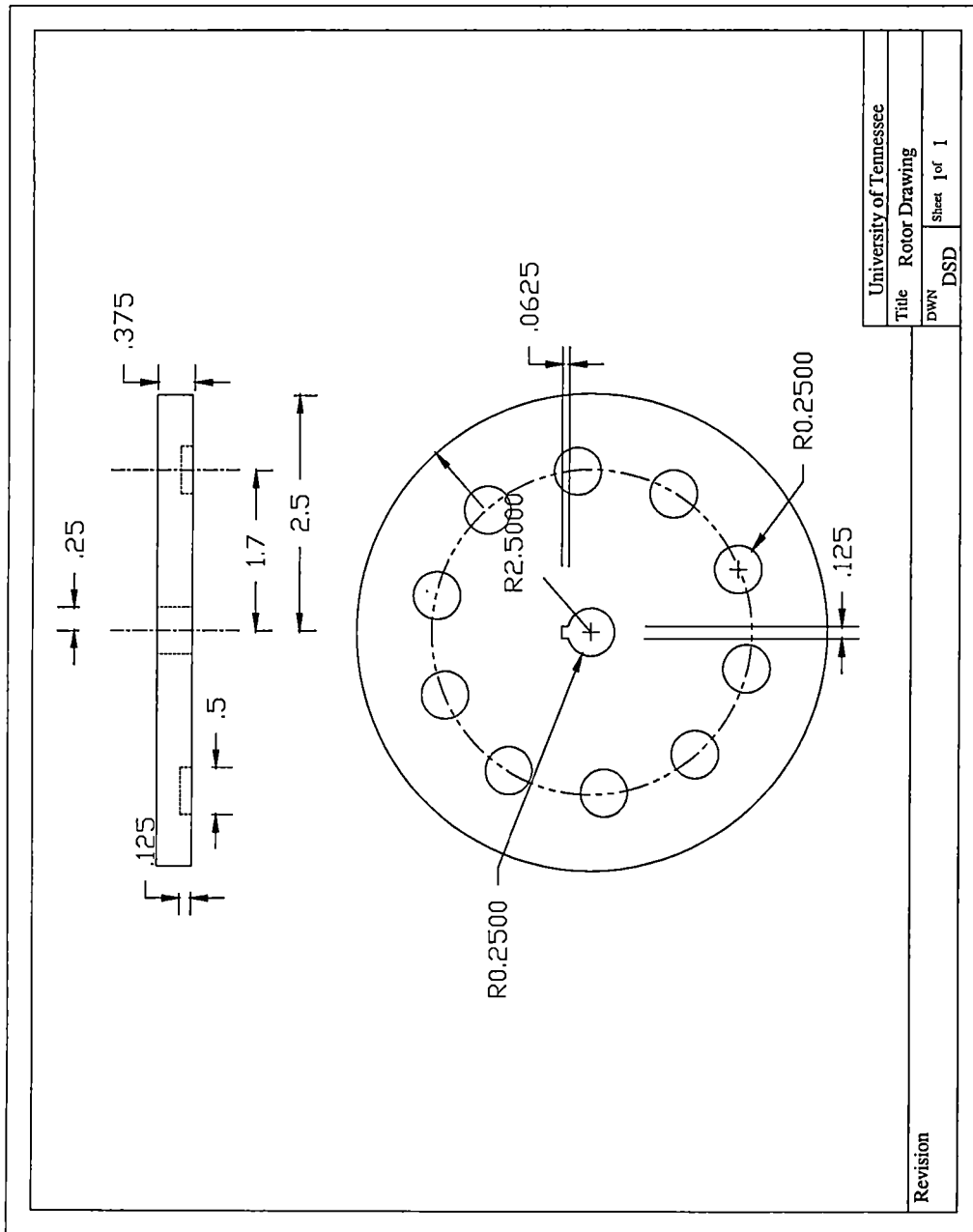


Figure E.2: Prototype rotor drawing.

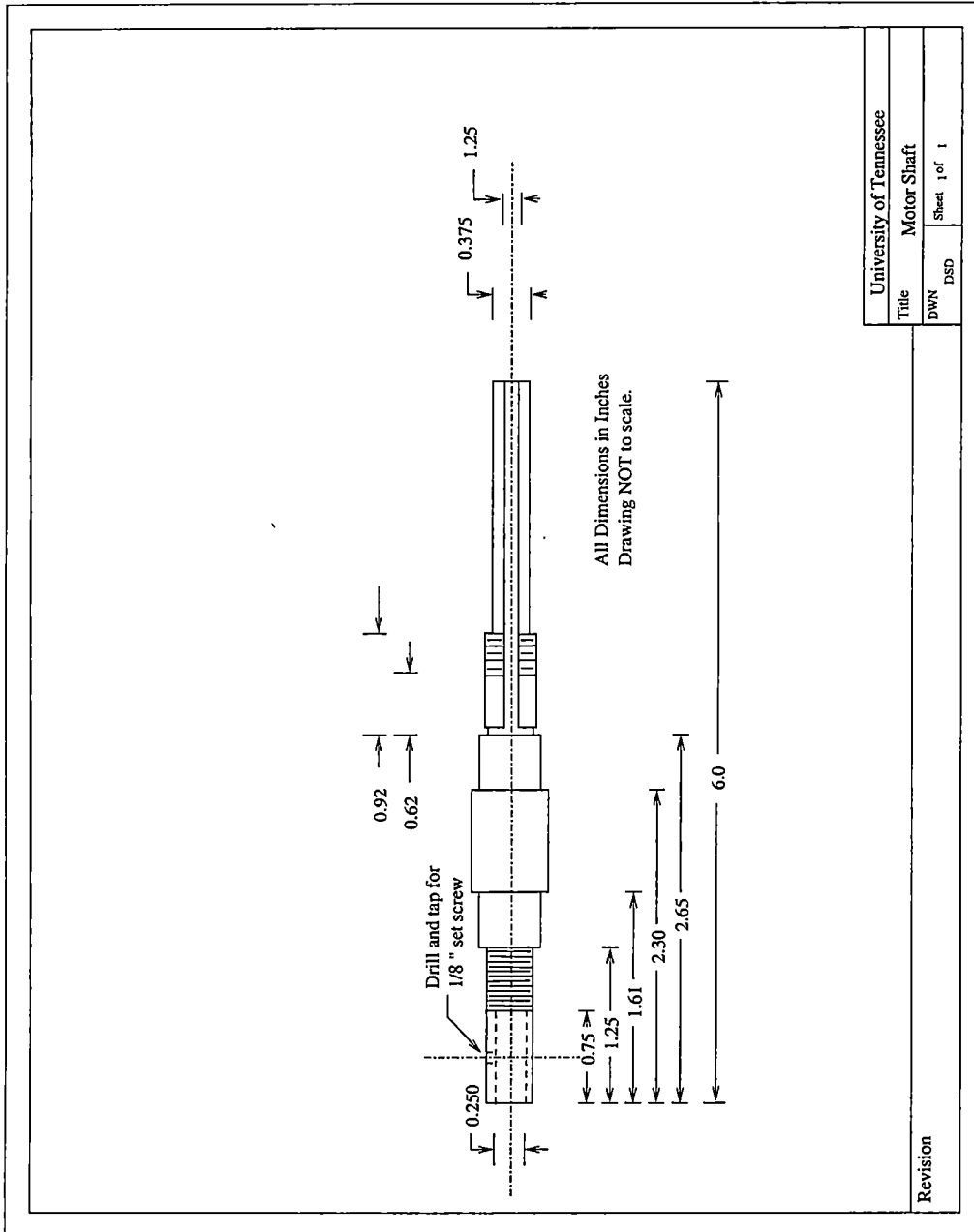


Figure E.3: Prototype shaft drawing.

Appendix F

Simulation Files

Scilab Code

```
R=.0432; // converted 1.7in to m
r=.00635; // converted .25 in to m
Np=10; // # of poles
Bg=.60; // Estimated flux Density
N=120; // # of turns per pole
Nm=2450; // Shaft Speed in rpm
w=Nm*(6.28/60); // Convert rpm -> rad/s
s=2*asin(r/R); // Provides range of valid expression
step=s/255; // Step size to create vector of length 256
theta=0:step:s;
//theta=.1
// ***** Equations to generate emf for 1/4 cycle *****

A1=2*r^2*acos(R*sin(theta/2)/r);
sqw=sin(theta/2) .* sin(theta/2);
Aa=2*R*sin(theta/2);
Ab=sqrt(r^2-R^2*sqw);
A2= Aa .* Ab;
A=A1-A2;
B=(sqrt(r^2-R^2*sin(theta/2).*sin(theta/2)));
F=(R^3/2)*(sin(theta/2).*sin(theta)./B);
H=(R*cos(theta/2).*B);
G=(r^2*R)*(cos(theta/2)./B);

// ***** end *****
```

APPENDIX F. SIMULATION FILES

```

e=-Np*N*Bg*w*(F-G-H); // added negative for aesthetics
//tst=(F-G-H);
// ***** generates 1/2 cycle from 1/4 cycle data *****

for t=1:2*length(e),
  if t<= length(e) then
    wav(t)=e(t);
  elseif t>length(e) then
    wav(t)=-e(2*length(e)-t+1);

  end
end

// ***** end *****
// ***** generates full cycle from 1/2 cycle data *****
for t2=1:2*length(wav),
  if t2<= length(wav) then
    wav2(t2)=wav(t2);

  elseif t2> length(wav) then

    wav2(t2)=-wav(t2-length(wav));

  end
end
// ***** end *****
xbase(0);xset("window",0);xselect(); // call up graphics window
//plot(theta,A);
//xbase(1);xset("window",1);xselect(); // call up graphics window
//plot2d([theta;theta],[e;390*cos(6*theta)]);
plot(0:2*%pi/(length(wav2)-1):2*%pi, wav2);

efft=abs(fft(wav2,-1)); // Takes fft of full cycle (magnitude)
np=length(efft);
// ***** Creates vector of lower order harmonics *****
Nharm=30;
Cnorm=length(efft)/2; // Normalize magnitude of fft by N/2
for i=1:Nharm
  wfft(i)=efft(i)/Cnorm;

```

APPENDIX F. SIMULATION FILES

```
end,  
// ***** end *****  
  
xbasc(2);xset("window",2);xselect(); // call up graphics window  
plot(0:Nharm-1,wfft); // Plot harmonics (skewed back to zero)  
  
// ***** Creates Fourier equivalent of waveform *****  
  
a=0:(2*%pi/1023):2*%pi;  
  
kmax=26; // # of harmonics to include  
vold=0;  
for k=0:2:kmax  
v=vold+wfft(k+2)*sin((k+1)*(a+(%pi/2)));  
vold=v;  
end,  
xbasc(3);xset("window",3);xselect(); // call up graphics window  
plot(a,v);  
  
// ***** end *****  
  
// ***** Create error vector for approximation *****  
  
err=wav2-v'; // Error of actual versus fourier approx. (v is transposed)  
xbasc(4);xset("window",4);xselect(); // call up graphics window  
plot(err);  
  
//***** end *****  
  
// Create vector of normalized fourier coefficients  
Kn=Bg*w*Np*N;  
nfft=wfft./Kn;  
save('fcoef',nfft)
```

Fortran Code

```

c Program to solve 1D magnetic diffusion equation
c by conservation methods
program mag_diff2
implicit real*4 (a-h, o-z)
parameter (Mp=1300)

dimension z(0:Mp), zf(0:Mp), bx(0:Mp),f(1:Mp),bxez(0:Mp)

data a,b/0.0,1.0/,bxa,bxb/1.0,1.0/
pi=4*atan(1.0)

print*, 'Enter mesh points, time max,stability factor,print step'
read*, m,tmax,stab,dtout
print*, 'Enter conductivity, permeability'
read(*,10) rho
print*, 'Enter permeability'
read(*,10) perm
10 format(E10.4)
d=1/(rho*perm)
print*, 'The value of d is', d

dz=(b-a)/m
dtexpl=(dz**2)/(2*d) ! Min time step for stability
dt=stab*dtexpl ! Stab<1 increases stability

call mesh(a,b,m,dz,z,zf)! call to mesh to create nodes and faces
time=0
tout=0

100 if (time.ge.tout) then

tout=tout+dtout
call output(m,z,bx,bxez)
write(3,*)
write(4,*)
call error(m,z,bx,bxez)
print*, 'data output at time', time
endif
time=time+dt

```

APPENDIX F. SIMULATION FILES

```

c ***** Flux and PDE routines*****
call flux(time,d,dz,m,bxa,b,bx,f)
c print*, 'flux 1', f(1)
do i=1,m
bx(i)=bx(i)+(dt/dz)*f(i)
enddo

c *****
call exact(d,m,bxa,tout,z,bxez,pi)

if (time.lt.tmax) then
goto 100
else
c print*, 'Execution stopped at',time
endif
do j=0,m+1
enddo
stop
end

c *****
c * SUBROUTINES *
c *****

subroutine mesh(a,b,m,dz,z,zf)
implicit real*4 (a-h, o-z)
dimension z(0:m), zf(0:m+1)

do i=1,m+1
zf(i)=a+(i-1)*dz ! faces
enddo

do i=1,m
z(i)=(zf(i)+zf(i+1))/2 ! nodes
enddo
return
end

c *****

subroutine flux(t,d,dz,m,bxa,b,bx,f)

```

APPENDIX F. SIMULATION FILES

```

implicit real*4 (a-h, o-z)
dimension f(1:m),bx(0:m+1)
bx(0)=1
f(1)=-d*((bx(1)-bx(0))/(dz/2)-(bx(2)-bx(1))/dz)
c  print*, 'flux1s',f(1)
do i=2,m-1
  f(i)=-d*((bx(i)-bx(i-1))/dz-(bx(i+1)-bx(i))/dz)
enddo

bx(m+1)=1
f(m)=-d*((bx(m)-bx(m-1))/dz-(bx(m+1)-bx(m))/(dz))

return
end
c  *****
subroutine output(m,z,bx,bxez)
implicit real*4 (a-h, o-z)

dimension z(0:m+1),bx(0:m+1),bxez(0:m+1)
do j=0,m
  print*,z(j),bx(j),bxez(j)
  write(3,*) z(j), bx(j)
  write(4,*) z(j), bxez(j)
enddo
return
end
c  *****

c  *****
subroutine exact(d,m,bxo,t,z,bxez,pi)
implicit real*4 (a-h, o-z)

dimension z(0:m+1),bxez(0:m+1)
do i=1,m
  olds=0

  do n=1,19,2

    sum=olds+(1.27/n)*sin(n*pi*z(i))*exp(-(pi*n)**2*t*d)
    olds=sum

```

APPENDIX F. SIMULATION FILES

```
        enddo
        bxez(i)=1-sum
        enddo
    return
end
c *****
subroutine error(m,z,bx,bxez)
implicit real*4 (a-h, o-z)
dimension z(0:m+1),bx(0:m+1),bxez(0:m+1)
dimension et(0:100)
do k=1,m
    et(k)=abs(bx(k)-bxez(k))
    print*, et(k)
    write(2,*) z(k),et(k)
enddo
write(2,*) ''
return
end
```

Vita

Daniel Steven Daniel, was born in Baltimore, Maryland on December 14, 1959. He attended both private and public schools in Woodlawn and Pikesville, Maryland. He graduated from Pikesville Sr. High in June of 1978. After graduating, he began working as a technician in the electric motor service industry.

After four years of working in the service industry, Steven began attending the Catholic University of America in Washington, D. C. majoring in Electrical Engineering. After graduating in the fall of 1985, he worked as a development engineer at Murray Corporation in Hunt Valley, Maryland. In 1986, Steven joined the Black and Decker Manufacturing Company in Towson, Maryland where he was employed for two years before attending the University of Tennessee-Knoxville in the fall of 1988 to pursue a Master's degree in Electrical Engineering.

As a graduate student, Steven was employed as a Development Associate at the Oak Ridge National Laboratory in Oak Ridge, Tennessee. In August of 1990, Steven left Tennessee to work in various industries around the United States. In the summer of 1993, he returned to Tennessee to continue his education and was awarded a Master's Degree in Electrical Engineering in December of 1993. After graduating, Steven re-joined the Oak Ridge National Laboratory.

Steven is formerly an Assistant Professor of Electrical Engineering at the University of Alaska-Fairbanks where he taught courses in electric machine theory, power systems, power electronics and digital design. In addition to teaching, he performed research in the area of novel electric machines and power electronics, in particular, their application to manned and unmanned vehicles.

Presently, Steven is Vice president of International Development Corporation a consulting firm providing design services in electronic engineering. In addition, he is an Adjunct Assistant Professor at the University of Tennessee Knoxville. He has co-authored several papers in the electric machines area and is co-inventor of a *Thermally responsive battery charger* U.S. Patent 5,013,993.